RESEARCH TECHNICAL REPORT

Development of Sprinkler Protection Guidance for Lithium Ion Based Energy Storage Systems

Development of Sprinkler Protection Guidance for Lithium Ion Based Energy Storage Systems

Prepared by

Benjamin Ditch
Dong Zeng

June 2019
(Revised October 2020)

FM Global
1151 Boston-Providence Turnpike
Norwood, MA 02062

PROJECT ID RW000029

Disclaimer

The research presented in this report, including any findings and conclusions, is for informational purposes only. Any references to specific products, manufacturers, or contractors do not constitute a recommendation, evaluation or endorsement by Factory Mutual Insurance Company (FM Global) of such products, manufacturers, or contractors. FM Global does not address life, safety, or health issues. Users of the information in this report must make the decision whether to take any action. FM Global undertakes no duty to any party by providing this report or performing the activities on which it is based. FM Global makes no warranty, express or implied, with respect to any product or process referenced in this report. FM Global assumes no liability by or through the use of any information in this report.

Executive Summary

Fire protection recommendations for Lithium-ion (Li-ion) battery-based energy storage systems (ESS) located in commercial occupancies have been developed through fire testing. A series of small- to large-scale free burn fire tests were conducted on ESS comprised of either iron phosphate (LFP) or lithium nickel oxide / lithium manganese oxide (LNO/LMO) batteries. Coupled with large-scale sprinklered fire tests, the performance of sprinkler protection common to commercial facilities where ESS are being installed was evaluated. The impact of installation practice, specifically space separation from combustible and non-combustible objects, was also assessed to ensure that the hazard of an ESS fire event can be managed to an acceptable level. The goal of this approach was to provide a framework to define the protection guidance for installations beyond the scope of the systems evaluated here. All test evaluations were conducted by FM Global at the FM Global Research Campus in Rhode Island, USA.

This report describes Phase 2 of a multi-phase project conducted in conjunction with the Property Insurance Research Group (PIRG) and in partnership with the Fire Protection Research Foundation (FPRF). The first phase of the project provided a fire hazard assessment of ESS systems to develop safe installation practices, fire protection guidance, and appropriate emergency response tactics for Li-ion battery ESS[i]. To support the fire hazard assessment, two free burn fire tests were conducted on Tesla 100 kWh Power Pack systems. These are the only known publicly available full-scale fire tests conducted with complete ESS units. Thus, there is limited real-scale data available to support a fire hazard assessment of Li-ion based ESS and there is no experimental data available to support sprinkler protection guidance.

The ESS available for this project phase were donated by a single integrator and were based on either LFP or LNO/LMO battery chemistry. Both systems were similar in construction with solid metal side and back wall, an open front, and contained 16 modules arranged in eight levels of two modules. The LFP modules were comprised on 78 prismatic batteries, each rated for 20 Ah at 3.3 V, for a total module rating of 120 Ah at 43 V. The LNO/LMO modules were comprised of 64 prismatic batteries, each rated for 32.5 Ah at 3.75 V, for a total module rating of 130 Ah at 60 V. The overall dimensions of a rack were 660 × 770 × 1,760 mm (26 × 30.25 × 69.25 in.) for the LFP system and 760 × 768 × 2,400 mm (30 × 30.25 × 94.5 in.) for the LNO/LMO system. All batteries were balanced to within ± 200 mV and the modules were charged to at least 95% state-of-charge (SOC) before each test. To limit the potential for electrical shock hazards to lab personnel and data acquisition equipment, individual modules were not electrically connected within the ESS rack. This adjustment is not expected to have affected the fire behavior of the ESS system under the conditions of the test.

At all test scales, which ranged from a single battery module to full ESS racks containing 16 modules each, the ESS system comprised of LFP batteries exhibited a lower overall hazard. This was most notably

[i] A. Blum and R. T. Long, "Hazard Assessment of Lithium Ion Battery Storage Systems," Final Report prepared for Fire Protection Research Foundation, February 2016.

observed in the sprinklered tests where a single sprinkler operation was sufficient to control the fire to the rack of origin, with no significant involvement of the modules in an adjacent rack. Under the same conditions the fire did spread to an adjacent rack in the test involving a system comprised of LNO/LMO batteries, and the number of sprinkler operations represented a demand area greater than 230 m^2 (2,500 ft^2).

While the design of the racks effectively shields the fire from sprinkler water, under the conditions of the tests, the sprinklers delayed or outright prevented fire spread to adjacent racks. Coupled with adequate space separation from nearby combustibles and the addition of thermal barriers between racks, the hazard can be further decreased. However, lacking a protection system that can suppress the fire in the early stages, prolonged fire duration, high water demand, and damage to the surroundings is likely. Protection guidance coupling sprinkler system design and ESS installation guidance, e.g., separation distance, is thus recommended to manage the hazard within acceptable levels.

The best protection recommendations based on current knowledge, are summarized below. The sprinkler system provides a minimum discharge density of 12 mm/min (0.3 gpm/ft^2) using sprinklers having a K-factor of 81 L/min/$bar^{1/2}$ (5.6 gpm/$psi^{1/2}$) or greater, with a nominal 74°C (165°F) temperature rating and RTI of 27.6 $m^{½}s^{½}$ (50 $ft^{½}s^{½}$). For ceiling heights in the range of 3.0 m (10 ft) to 7.6 m (25 ft) the ceiling construction should have a minimum 1-hour fire rating. All ceiling-level sprinkler protection should be installed in accordance with FM Global Property Loss Prevention Data Sheet 2-0 (DS 2-0), *Installation Guidelines for Automatic Sprinklers*, January 2014. The protection recommendations are:

- For the tested LFP system:
    - Without fire protection, the minimum space separation from any part of the ESS is 1.2 m (4 ft) from non-combustible objects and 1.8 m (6 ft) from combustible objects, including adjacent ESS racks.
    - With sprinkler protection, the minimum space separation from any part of the ESS is 0.9 m (3 ft) from non-combustible objects and 1.5 m (5 ft) from combustible objects. The sprinkler system water supply should be designed for a minimum 230 m^2 (2,500 ft^2) demand area and a duration of at least 90 minutes.
    - These separation distances are based on the LFP system with an 83.6-kWh electrical capacity, refer to Table 7-1 for guidance on lower electrical capacity systems.
- For the tested LNO/LMO system:
    - Without fire protection, the minimum space separation from any part of the ESS is 2.4 m (8 ft) from non-combustible objects and 4.0 m (13 ft) from combustible objects, including adjacent ESS racks.
    - With sprinkler protection, the minimum space separation from any part of the ESS is 1.8 m (6 ft) from non-combustible objects and 2.7 m (9 ft) from combustible objects. The sprinkler system water supply should be designed for the total room area where the ESS is located, and the water supply should be calculated as 45 minutes times the

number of adjacent racks (i.e., the number of racks installed such that the horizontal spacing is less than the recommended space separation for combustible objects).

- These distances are based on the LNO/LMO system with a 125-kWh electrical capacity, refer to Table 7-1 for guidance on lower electrical capacity systems.

- For ESS comprised of multiple racks, each individual LFP or LNO/LMO rack should be separated as combustibles per Table 7-2 when sprinkler protection is not provided. Refer to Section 7.1.2 for guidance on separation distance when sprinkler protection is provided.

- Additional protection guidance can be found in the Recommendations Section of the main body of the report, including separation distances resulting from testing of LFP and LNO/LMO systems with a lower energy capacity.

ESS representing a hazard outside the above listed conditions, including design features and power rating, may require a more robust protection scheme to account for several unknowns that can negatively affect protection effectiveness. Large-scale free burn tests, as described in Section 6.1, are recommended to determine adequate space separation distances to prevent fire spread to nearby combustibles or damage to non-combustibles, when sprinkler protection is not provided. Large-scale sprinklered tests, as described in Section 6.2, are recommended to determine adequate space separation distances to prevent fire spread to nearby combustibles, excluding adjacent ESS racks, or damage to non-combustibles, as well as sprinkler protection design, including discharge density/area and water supply duration.

In practice, a fire watch should be present until all potentially damaged ESS equipment containing Li-ion batteries is removed from the area following a fire event. Fires involving Li-ion batteries are known to reignite any time from minutes to days after the initial event. Adequate cooling of the batteries is necessary in order to prevent reignition. Finally, this project has not addressed explosions hazards or any mitigating that may occur during an ESS fire or an independent event, or firefighting tactics.

Errata Notice: An earlier version of this report issued in June 2019 referred to one of the tested batteries as “Nickel manganese cobalt oxide (NMC) and lithium manganese oxide (LMO)”. It should have been “Lithium nickel oxide (LNO) and lithium manganese oxide (LMO)”. This change has been reflected in Table 3-1. In addition, references throughout the text to the battery type “NMC” have been replaced with “LNO/LMO”. Finally, the units for the secondary vertical axis in Figure 5-9 (left) have been changed from BTU/min to BTU/s.

Abstract

Protection recommendations for Lithium-ion (Li-ion) battery-based energy storage systems (ESS) located in commercial occupancies have been developed through fire testing. A series of small- to large-scale free burn fire tests was conducted on ESS comprised of either iron phosphate or lithium nickel oxide / lithium manganese oxide batteries. Coupled with large-scale sprinklered fire tests, the performance of sprinkler protection common to commercial facilities where ESS are being installed was evaluated. The impact of installation practice, specifically space separation from combustible and non-combustible objects, was assessed to ensure that the hazard of an ESS fire event can be managed to an acceptable level. Where applicable, best protection recommendations based on current knowledge have been provided.

Acknowledgements

The authors thank Mr. R. Chmura, Mr. J. Chaffee, and the entire FM Global Research Campus crew for their efforts in conducting the fire tests. This was a monumental effort that required the coordination and support from staff across the Research Campus. Special gratitude is extended to Mr. Mike Racicot, Mr. Kevin Mullins, Mr. Mike Skidmore, and Mr. Jason Tucker for their extreme patience and flexibility working through the unique aspects of these tests. Mr. Kris Olsen, as well as the entire Instrumentation Group, were also critical to the project success. Finally, the diligent oversight of project safety and hazardous material disposal by Mrs. Janine Pitocco ensured personnel safety throughout this project.

The authors greatly acknowledge the discussion and input from the many Research group members that provided valuable technical discussions from Drs. Sergey Dorofeev, Franco Tamanini, and Yibing Xin. The FM Global Engineering Standards group is also thanked for their expertise in loss prevention which allowed for definitive protection recommendations, improving the practical application of this work.

The authors further thank Mrs. Amanda Kimball, of the Fire Protection Research Foundation, as well as Mr. Dan Gorham and the members of the Property Insurance Research Group for their insightful discussions. In addition, the funding provided by PIRG members and other sponsors for the procurement of ESS and disposal services was essential to the economic feasibility of this project.

Finally, the authors would like to thank Ms. Denise Staplins for processing this report.

Table of Contents

List of Figures

List of Tables

PAGE LEFT INTENTIONALLY BLANK

1. Introduction

The use of Lithium-ion (Li-ion) battery-based energy storage systems (ESS) has grown significantly over the past few years. In the United States alone the use has gone from 1 MW to almost 700 MW in the last decade [1]. Many of these systems are smaller installations located in commercial occupancies, such as office buildings or manufacturing facilities. Yet, there has been relatively little research conducted that can be used to ensure that effective fire protection strategies are in place.

The main difference between Li-ion and other battery chemistries, such as lead-acid, is the potential for thermal runaway reactions leading to venting of ignitable gases. Many studies have addressed how failure of a single cell battery is affected by characteristics such as chemistry, electrolyte composition, state-of-charge (SOC), or format [2-8]. The subsequent propagation of thermal runaway to adjacent cells in a multiple cell battery module has also be studied to a lesser extent [9, 10].

This report describes part of a multi-phase project conducted in conjunction with the Property Insurance Research Group (PIRG) and in partnership with the Fire Protection Research Foundation (FPRF). The first phase of the project provided a fire hazard assessment of ESS systems to develop safe installation practices, fire protection guidance, and appropriate emergency response tactics for Li-ion battery ESS [11]. To support the fire hazard assessment, two free burn fire tests were conducted on Tesla 100 kWh Power Pack systems. These are the only known publicly available full-scale fire tests conducted with complete ESS units. Separate intermediate-scale fire testing by DNV-GL [12] has also been recently conducted at the module level to evaluate the performance of different fire suppressants. Suppressants included water, wet chemical, and dry chemical agents. In this case, the fire suppressants where applied directly onto the module, representing protection provided within the ESS rack. While this testing does not allow for estimation of the performance of a typical commercial occupancy protection system where sprinklers are located outside of the rack, water was identified as the most effective suppressant tested, presumably due to its high thermal capacity. The effectiveness of water at protecting Li-ion battery fires is further supported by large-scale testing by Ditch [13] where sprinkler protection was successful for a warehouse storage scenario. These recent efforts provide confidence that sprinkler protection can be sufficient for ESS in commercial occupancies. However, there are limited real-scale data available to support a fire hazard assessment of Li-ion based ESS and there are no experimental data to support sprinkler protection guidance.

From a fire protection standpoint, the overall fire hazard of any ESS is a combination of all the combustible system components, including battery chemistry, battery format (e.g., cylindrical, prismatic, polymer pouch), battery capacity and energy density, materials of construction, and component design (e.g., battery, module). To ensure confidence in the resulting protection guidance, the ESS were assumed to be operating under an abuse condition, such that proprietary electronic protection systems, e.g., battery management system (BMS), were not active. Any benefit from these proprietary systems would further reduce the overall hazard, e.g., the likelihood of ignition, but is not necessary to ensure the adequacy of the protection.

The following is a breakdown of the experimental tasks completed to determine sprinkler protection guidance for ESS installations within commercial occupancies:

- Small-scale tests were conducted on an individual ESS module to determine an appropriate ignition scenario to induce thermal runaway of the Lithium-ion batteries.
- Large-scale free burn fires were conducted on full ESS racks to establish the overall hazard of the donated ESS. Similar intermediate-scale tests were conducted on partial ESS racks to evaluate the effect of system capacity (e.g., kWh) on the hazard.
- Large-scale sprinklered fire tests were then conducted to determine the performance of sprinkler protection typical to commercial facilities where an ESS may be found.

FM Global contributed the resources associated with conducting the research program, including storage and post-test cleanup of the Li-ion batteries. The batteries used in the tests were donated by a private supplier. Disposal and recycling services were donated by a waste management company specializing in disposal of Li-ion batteries. The balance of the costs, which included program management services, was supplied by PIRG.

2. Existing ESS Protection Guidance Documents

In the United States, installation requirements for ESS within nonstorage buildings are currently affected by guidance documents, such as NFPA 13, *Standard for the Installation of Sprinkler Systems* [14], and FM Global Property Loss Prevention Data Sheets 2-0 (DS 2-0), *Installation Guidelines for Automatic Sprinklers* [15] and 3-26 (DS 3-26), *Fire Protection Water Demand for Nonstorage Sprinklered Properties* [16]. These guidance documents include fire protection requirements adequate for the contents of the occupancy, where the hazard category (HC) of the occupancy determines the sprinkler demand. In order of increasing fire hazard within the Data Sheets, the hazard category increases from lowest (HC-1) to highest (HC-3) hazard. For example, in DS 3-26 a sprinkler density of 4 mm/min (0.1 gpm/ft^2) generally relates to an HC-1 occupancy for ceiling heights up to 9.1 m (30 ft), 8 mm/min (0.2 gpm/ft^2) relates to an HC-2 category, and 12 mm/min (0.3 gpm/ft^2) relates to an HC-3 occupancy. Comparable occupancy hazard classifications in NFPA 13 (per Figure 11.2.3.1.1) are light hazard, ordinary hazard 2, and extra hazard group 2 (EH2), respectively. The applicable sprinkler system demand area for water supply calculations is typically 230 m^2 (2,500 ft^2) for both DS 3-26 and NFPA 13.

Sprinkler protection requirements for ESS will soon be addressed in NFPA 855, *Standard for the Installation of Stationary Energy Storage Systems* [17]. The proposed sprinkler protection guidance aligns with an EH2 occupancy per NFPA 13 or HC-3 occupancy per DS 3-26, as listed above. Similar guidance is also anticipated within FM Global Property Loss Prevention Data Sheets 5-33, Electrical Energy Storage [18]. Both documents provide installation and protection guidance for Li-ion battery-based ESS.

With regard to the current project, the highest sprinkler density available was targeted after review of the large-scale free burn test results. Sprinkler protection was provided by a K81 L/min/bar$^{1/2}$ (K5.6 gpm/psi$^{1/2}$), quick-response, nominal 74°C (165°F) temperature rated sprinklers. The sprinklers were installed such that the thermal link was located 0.3 m (1 ft) below the ceiling, which corresponds to the maximum allowed in both NFPA 13 and DS 2-0. The specific protection option selected allows for addressing a representative fire scenario within the constraint of the limited number of fire tests that can be conducted in this work.

Refer to reference [11] for an overview of the Li-ion battery technology, commercial ESS types, ESS safety standards, and relevant codes and regulations.

3. Experimental Method

The methodology for this project consisted of four experimental tasks to establish the range of hazard posed by Li-ion battery-based ESS and the subsequent level of protection provided by ceiling-level sprinkler systems. The goal of this approach was to maximize the application of large-scale fire tests and provide general sprinkler protection guidance for ESS located within commercial occupancies.

3.1 Donated ESS Equipment

An extensive solicitation for donations was coordinated in 2017 with FPRF and included multiple ESS manufacturers, integrators and users, as well as energy utilities and industry organizations. Two types of ESS were procured from a single manufacturer and detailed specifications are provided in Table 3-1. Since this project was not intended to provide a specific evaluation of an individual manufacturer's product all identifiable branding has been removed, and the equipment is generically referenced by battery chemistry.

Table 3-1: ESS equipment specifications.

Specification	LFP	LNO/LMO
Battery Description		
Chemistry	Lithium iron phosphate (LFP)	Lithium nickel oxide (LNO) and lithium manganese oxide (LMO)
Capacity (Ah)	20	32.5
Voltage (VDC)	3.3	3.75
Format	Prismatic	Prismatic
Nominal Dimensions, L×W×H (mm [in.])	227 × 161 × 7.25 (8.9 × 6.3 × 0.3)	290 × 216 × 7 (11.5 × 8.5 × 0.3)
Module Description		
Capacity (Ah)	120	130
Voltage (VDC)	42.9	60
Power (kWh)	5.2	7.8
Battery Layout (S= series, P = parallel)	13S6P	16S4P
Battery Quantity (#)	78	64
Nominal Dimensions*, L×W×H [mm (in.)]	700 × 270 × 180 (27.5 × 10.75 × 7)	650 × 320 × 240 (25.5 × 12.75 × 9.5)
Mass, kg (lb)	49 (108)	75 (166)
Rack Description		
Capacity (Ah)	120	130
Voltage (VDC)	686 (16 modules)	960 (16 modules)
Rack Layout (i.e., module configuration)	2 wide × 8 tall	2 wide × 8 tall
Enclosure	Open front, solid sides	Open front, solid sides
Nominal Dimensions, W×D×H [mm (in.)]	660 × 770 × 1,760 (26 × 30.25 × 69.25)	760 × 768 × 2,400 (30 × 30.25 × 94.5)

The manufacturer balanced the individual batteries to within ± 200 mV and charged all the modules to at least 95% SOC, based on voltage, during December 2017 and January 2018. The self-discharge rate for both battery types was expected to be less than 0.5%/month which resulted in a condition that meets or exceeds the 90% SOC desired for testing. The SOC of each module was confirmed to be at least 95% before each test. To limit the potential for electrical shock hazards to lab personnel and data acquisition equipment, individual modules were not electrically connected within the ESS rack.

Each ESS was similar in construction as shown in Figures 3-1 and 3-2 for the LFP equipment and Figures 3-3 and 3-4 for the LNO/LMO equipment. In both cases, the racks consist of 16 modules installed such that there are eight levels of two modules located side-by-side. The side and back walls of the racks were predominately solid. The front was open, leaving the plastic face of the module exposed, with the exception of a removable narrow panel between those modules that extended the height of rack. This panel was ABS plastic for the LFP equipment and aluminum for the LNO/LMO equipment. The BMS (not active) for each rack was located within a rectangular box above the top level of modules.

Figure 3-1: Photos of LFP rack; front (right), side (middle), and back (right).

Figure 3-2: Photos of LFP module with front face of module shown on left side of picture.

Figure 3-3: Photos of LNO/LMO rack; front (right), side (middle), and back (right).

Figure 3-4: Photos of LNO/LMO module; front face (left) and top with front face of module shown on left side of picture (right)

3.2 Combustible Load

As shown in Table 3-2, the total combustible load per LFP module is estimated to be 279 ± 28 MJ (265 ± 26 BTU×10^3) or 4,464 ± 446 MJ (4,233 ± 423 BTU×10^3) for a rack comprised of 16 modules. Corresponding values for the LNO/LMO module are 509 ± 51 MJ (482 ± 48 BTU×10^3) or 8,142 ± 814 MJ (7,719 ± 772 BTU×10^3) per rack. Each LFP module has an approximate weight of 50 kg (110 lb), of which ~15% by weight is represented by combustible load; similarly the LNO/LMO module has an approximate weight of 75 kg (165 lb), with ~18% combustible load. The remaining components of the ESS rack are predominantly metal and contribute negligible amounts of available chemical energy.

The above combustible load calculations are based on the listed masses and the heats of combustion for each material listed in Table 3-2. These values should be considered gross estimates and are only provided here as a relative comparison of the total energy between the two ESS types. While a detailed list of module components and associated weights was provided as part of the donation, only generic descriptions of the material composition were available. Therefore, the materials of construction are separated into two categories: unexpanded plastics and electrolyte. It was further assumed that

electrolyte represented 7% of the individual battery mass, which is consistent with batteries of a similar capacity [13]. The heat of combustion value for diethyl carbonate (DEC) was used as a representative estimate for electrolyte as it has been shown to be similar to other organic carbonate solvents typically found in Li-ion battery electrolyte [19]. The exact composition of the electrolytes or unexpanded plastics are unknown, therefore a variance of ± 10% was assumed for all heats of combustion. The contribution from electrical energy stored within the batteries was calculated from the power rating listed in Table 3-1, assuming 100% SOC and ± 10% uncertainty.

Table 3-2: Combustible load for LFP and LNO/LMO equipment.

Material	LFP Module		LNO/LMO Module	
	Mass	Energy*	Mass	Energy*
	kg (lb)	MJ (BTU×10^3)	kg (lb)	MJ (BTU×10^3)
Electrolyte	2.6 (5.7)	73 ± 7 (69 ± 7)	3.6 (7.9)	100 ± 10 (95 ± 9)
Plastic	4.9 (10.9)	188 ± 19 (178 ± 18)	10 (22.1)	381 ± 38 (361 ± 36)
Electrical Energy†	n/a	18.5 ± 2 (17.5 ± 2)	n/a	28 ± 3 (27 ± 3)
Total [1 Module]	7.5 (16.5)	279 ± 28 (265 ± 26)	13.6 (30.0)	509 ± 51 (482 ± 48)
Rack Total [16 modules]	120 (265)	4,464 ± 446 (4,233 ± 423)	218 (480)	8,142 ± 814 (7,719 ± 772)

*Energy is calculated using a ΔH_C for electrolyte = 28 MJ/kg (12.0 BTU/lb) [20] and unexpanded plastic = 38 MJ/kg (16.3 BTU/lb) [21].
†Electrical energy in MJ calculated from the module power rating as P (kWh) × 3.6 s.

3.3 Test Facilities

Testing was conducted at three laboratory spaces within the Fire Technology Building at the FM Global Research Campus in West Glocester, Rhode Island, USA. Free burn fire tests were conducted under a fire products collector (FPC) to allow for real-time heat release rate (HRR) measurement. Small- and intermediate-scale testing, described in Sections 4 and 5, utilized the 5-MW FPC located in the Calorimetry Lab. The 5-MW FPC consists of a 6.1 m (20 ft) diameter inlet that tapers down to a 1.5 m (5 ft) diameter duct. The inlet to the FPC is at an elevation of 7.9 m (26 ft) from the floor and the air exhaust rate was set to 24 m^3/s (50,000 ft^3/min). Large-scale testing, described in Section 6.1, utilized the 20-MW FPC, which consists of an 11 m (36 ft) diameter inlet that tapers down to a 3.0 m (10 ft) diameter duct. The inlet to the FPC is at an elevation of 11.3 m (37 ft) and the air exhaust rate was set to 71 m^3/s (150,000 ft^3/min). For both FPCs, combustion gas concentration, velocity, temperature and moisture content of the exhaust air from the lab are measured within the FPC duct. Beyond the measurement location, the exhaust duct connects to a wet electrostatic precipitator (WESP) prior to the gases venting to the atmosphere.

Large-scale sprinklered fire tests were conducted under the north movable ceiling, which is flat and unobstructed. The ceiling measures 24.4 m x 24.4 m (80 ft x 80 ft) and is adjustable for heights above the floor ranging from 3.0 m to 18.3 m (10 ft to 60 ft). The air emission control system (AECS) exhaust ducting consists of four extraction points, located at the lab ceiling that are 24 m (80 ft) above the test floor. The extraction points merge into a single duct with a cross-sectional area of 6.1 m^2 (66 ft^2) where

measurement of the exhaust flow is made similar to that of the 20 MW-FPC. The air exhaust rate was set to 94 m^3/s (200,000 ft^3/min) and the movable ceiling was set to an elevation of 4.6 m (15 ft) from the floor. For reference, Figure 3-5 is a plan view of the LBL showing the north movable ceiling, the south movable ceiling, and the 20-MW Fire Products Collector (FPC).

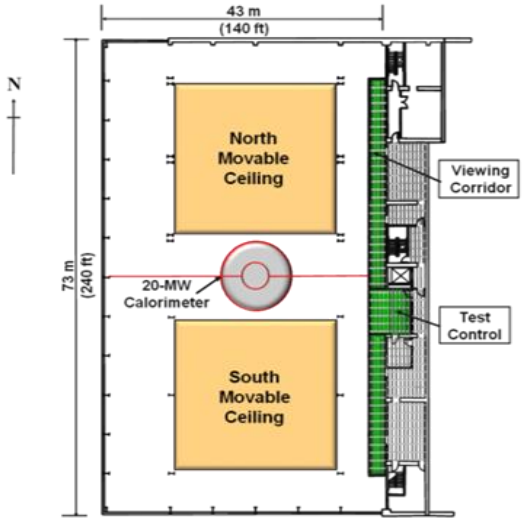

Figure 3-5: Illustration of FM Global Large Burn Laboratory test locations.

3.4 Instrumentation and Analysis Methods

Various instruments were used to evaluate the heat exposure and spread of fire within the ESS unit, as well as the heat exposure to nearby equipment and structures. The instrumentation layout was intended to provide continuity in the measurements acquired as testing progressed from small to large scale. To simplify the report, this section provides a general description of the use and specification for each type of instrument. Schematics showing specific measurement locations used for each test can be found in Sections 4 through 6. All instrumentation was calibrated in accordance with ISO/IEC 17025 [22].

3.4.1 Environmental Conditions

Environmental conditions, including relative humidity, dry-bulb temperature, and wet-bulb temperature of the air inside and outside of the lab, were measured just prior to each test as well as continually during each test with Vaisala HMT337 humidity and temperature transmitters. The transmitters are located within the laboratory space at four points surrounding the test array and at one outdoor location near the air inlet to the laboratory.

3.4.2 Thermocouples

Thermocouples (TCs) were used to monitor the spread of fire within the ESS rack and the potential for fire spread to the adjacent racks. Measurements were acquired on each battery module and at multiple locations on the ESS rack with Type K, stainless-steel sheathed, ungrounded, 6.4 mm (0.25 in.), chromel-alumel TCs (Omega Engineering, Inc., model KMQXL-062U, or equivalent). Ungrounded TCs were selected to minimize leakage current from damaged batteries reaching the data acquisition hardware. TCs were either secured using aluminum tape or mechanically fastened with a tech bolt/washer combination located at least 25.4 mm (1 in.) from the measurement junction.

TC measurements from all tests were edited to remove erroneous data believed to be a result of leakage current from damaged batteries, e.g., sparks, reaching the TC bead. Sparking, and thus the need for data editing, was more predominant for the LNO/LMO batteries though was also observed for the LFP batteries. While ungrounded TCs were selected to mitigate this effect, the millivolt measurement response of TCs is still susceptible to damage or temporary erroneous readings when impacted by a much higher voltage spark.

Figure 3-6 shows an example of two types of data series acquired during Sprinklered Test #2 with LNO/LMO batteries. Module6 illustrates data temporarily reporting unrealistically erratic measurements before returning to reasonable values. Module5 and Module10 illustrate data where measurements were continually truncated at the data acquisition system threshold values of -200°C (-328°F) or 1,328°C (2,422°F) indicating physically unrealistic data. Interestingly these data exhibit opposite trends where Module5 reports the lower threshold while Module10 reports the upper threshold. Module14 illustrates data not impacted by leakage current.

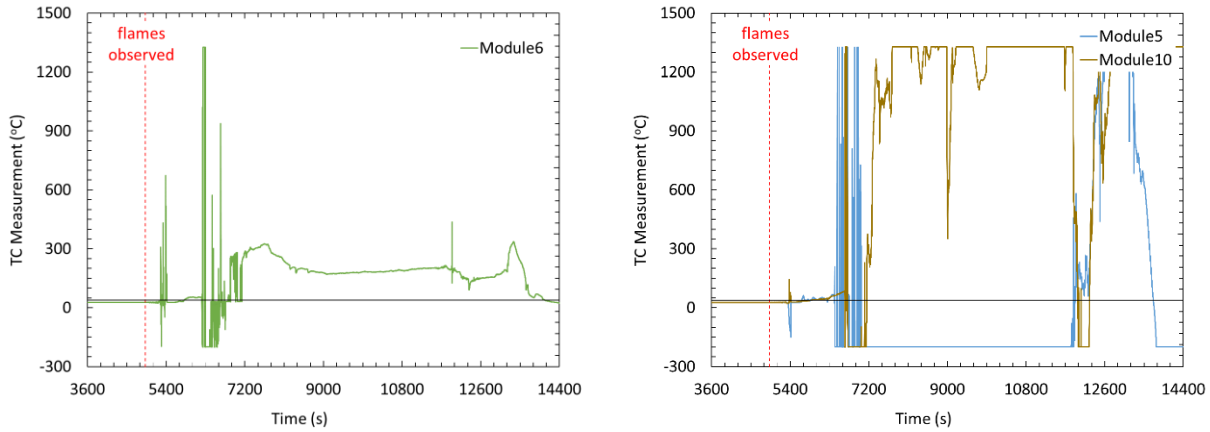

Figure 3-6: Example of original TC Measurements during the sprinklered LNO/LMO Test. Temporarily erroneous data shown on left and continuous erroneous data shown on right.

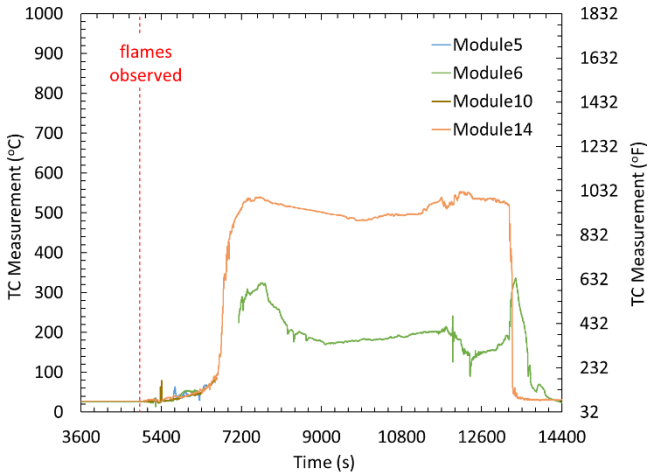

Figure 3-7: Example of edited TC measurements during the sprinklered LNO/LMO Test. Module14 included as an example of a data series that did not require editing.

Figure 3-7 shows data that have been edited to remove values below 25°C (75°F), i.e., ambient lab temperature, exceeding 1,000°C (1,832°F), or exhibiting a 1 s change greater than 100°C (212°F). For example, the temporary erratic measurements from 5,270 to 5,370 s and 6,200 to 6,700 s were removed from Module6. Module5 and Module10 were truncated at ~6,500 s due to continuous erratic measurements. Module14 is also shown as an example of data that did not need to be edited.

3.4.3 Heat Flux and Heat Flux Measurements

The primary focus of this project was to measure the thermal exposure to objects adjacent to and surrounding an ESS fire. The two most common methods to measure incident heat flux are Schmidt-Boelter (S-B) heat flux gages / radiometers and plate thermometers. Previous work conducted by the Sandia National Laboratory has shown that each of these methods exhibits similar measurement uncertainty, in the range of 24% to 40% depending on the fire environment [23]. This emphasizes the importance of selecting the proper measurement technique for the intended fire environment. For instance, S-B gages are best suited for measurements outside of the fire or for highly transient fires and are characterized by high sensitivity and a fast thermal response. Conversely, plate thermometers are robust and well suited for measurements inside of a fire but require corrections to account for convective and radiative losses as well as thermal inertia under transient fire conditions.

3.4.3.1 Heat Flux Gages and Radiometers

Heat flux gages and radiometers were used in all tests to measure the thermal exposure to nearby equipment and structures. In addition, heat flux gages were also used during the large-scale free burn tests to monitor the thermal exposure to ESS racks adjacent to the fire. The heat flux gages were of Schmidt-Boelter type with ranges of either 0-50 or 0-100 kW/m^2 (0-260 or 0-530 BTU/ft^2/min) and were generally located near the fire source where convective and radiative heat transfer was anticipated. Radiometers were also Schmidt-Boelter type with an integrated sapphire crystal window and had a range of either 0-2, 0-5, or 0-10 kW/m^2 (0-11, 0-26, or 0-53 BTU/ft^2/min) and were located away from the fire where radiation was the predominant mode of heat transfer. All gages were water cooled to ~ 45°C (113°F).

3.4.3.2 Plate Thermometers

Custom plate thermometers (PTs) were used in the large-scale free burn fire tests (Section 6.1) to measure the thermal exposure to equipment located adjacent to an ESS fire. Refer to Figure 6-2 for the specific locations of the PTs, which were arranged in vertical arrays on mock ESS racks positioned on either side of a test rack. As shown in Figure 3-8, the PTs were constructed by mounting sheathed TCs to the backside (inside) of the mock racks with a metal bolt and washer. The TC bead was offset from the bolt by 25 mm (1 in.) and thermally isolated from the washer with Cotronics insulation to minimize conductive losses. The entire assembly is then further insulated with 200 mm (8 in.) diameter by 25 mm (1-in.) thick KAO wool.

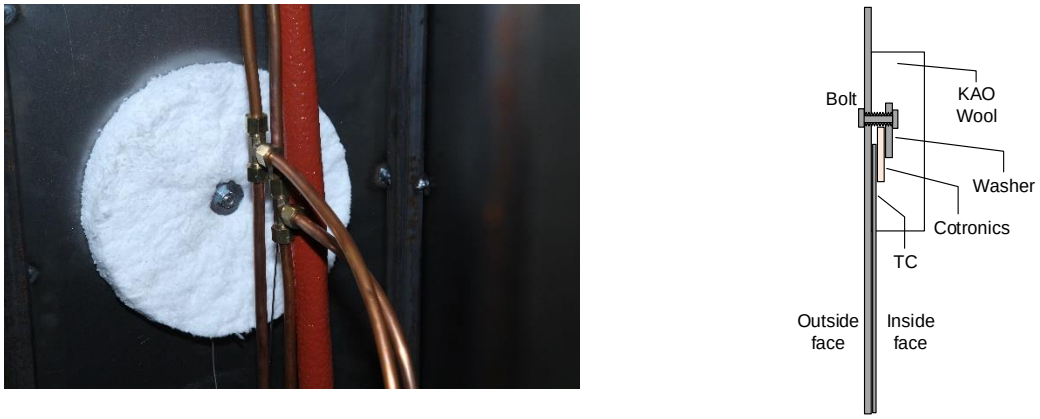

Figure 3-8: Photo of backside of TCs installed on mock ESS rack (TC28 – 37) on left and schematic of TC attachment on right.

The total net heat flux to a surface comprises both radiative and convection heat transfer, as well as losses due to reflection and conduction through the surface

$$\dot{q}''_{tot} = \varepsilon(\dot{q}''_{rad} - \sigma T_s^4) + \dot{q}''_{conv} - \dot{q}''_{loss} \quad 3\text{-}1$$

where $\dot{q}''_{rad}$ is the radiative heat flux, $\dot{q}''_{conv}$ is the convective heat flux, and $\dot{q}''_{loss}$ is the heat flux loss term due to conduction (all in kW/m^2). Here, the radiation term is the difference between the absorbed incident radiation and the emitted radiation from the surface.

The design of these tests allows for two simplifications to the total net heat flux calculation. First, under the radiation dominated conditions that were present during the high fire intensity stage, the convective term becomes small and can be neglected. Second, the backsides of the PT were well insulated to provide a near adiabatic surface, as shown in Figure 3-8, which minimizes the effects of back-surface heat loss and means that the loss term can be neglected. Heat conduction between the insulated and uninsulated portions of the PT was not considered but should be minimal given the small thickness of the metal.

The radiative heat flux received by the surface can be written as:

$$\dot{q}''_{rad} = \frac{1}{\varepsilon}[\varepsilon\sigma(T_s^4 - T_\infty^4) + \rho d c_p \frac{dT_s}{dt}] \quad 3\text{-}2$$

where σ is the Stefan-Boltzmann constant with the value of 5.67 x 10^{-8} W/m^2 K, and T_s is the surface temperature in K. T_∞ is the ambient surface temperature in K, and the emissivity (ε) should be set to 1.0 for a black body. The plate thermometers were constructed with 18 gage steel and had material properties of: density (ρ) with a value of 7,700 kg/m^3 (480 lb/ft^3), specific heat of the surface (c_p) with a value of 0.49 kJ/kg·K (0.117 BTU/lb·°F), and thickness of the surface (d) with a value of 1.2 mm (0.047 in.). The resulting value represents the imposed heat flux as the emissivity of the PT is conservatively assumed as unity.

3.4.4 Heat Release Rate

Heat release rate was measured from the collection of combustion gases to compare the fire development, overall magnitude, and total energy released for each test. Three different measurement techniques were used based on convective, chemical, and radiative energy depending on the conditions of the test and available instrumentation.

3.4.4.1 Convective and Chemical Energy (real-time)

Free burn tests were conducted under an FPC to allow for real-time convective and chemical heat release measurements. Convective flow within the FPC duct was measured with a Type K, exposed junction, 6.4 mm (0.25 in.) sheathed, chromel-alumel thermocouple and an impact tube averaging ring. The convective heat release rate, $\dot{Q}_{c,}$ is calculated from the gas temperature and mass flow through an FPC as

$$\dot{Q}_c = \dot{m}_{gas} c_p \Delta T \qquad 3\text{-}3$$

where, $\dot{m}_{gas}$ is the mass flow entering the duct in kg/s and ΔT is change in air temperature from the ambient value through the FPC. Corrections are made for the change in c_p as a function of temperature. All temperatures are entered in K and $\dot{Q}_c$ is given in kW. For error analysis, it was assumed that convective measurements have an uncertainty of ±10% based on the combined uncertainty of the instrumentation.

Due to the unique nature of an ESS fire, energy calculations based on the hot gas flow above the fire represent the apparent, or bulk, convective energy released. The measured gas flow includes contributions from three main sources: 1) heat generated from combustion, 2) heat generated from the thermal runaway of batteries, and 3) sensible heat stored in the battery modules and the ESS rack. The impact of these different heating mechanisms is most notably observed in Sections 4.3.4, 5.2.4, and6.1.2.5, where the release of sensible heat stored in the modules and rack structure are measured as convective energy even after the fire extinguished.

Combustion gases within the FPC duct were measured with non-dispersive infrared carbon monoxide (CO) and carbon dioxide (CO_2) gas analyzers to calculate the generation of carbon monoxide and carbon dioxide, and a flame ionization detector total hydrocarbon (THC) analyzer to measure the release of volatile organic compounds (VOC) as equivalent methane. Chemical heat release rate based on carbon dioxide and carbon monoxide generation (CDG) is calculated as

$$\dot{Q}_{chem} = \Delta H_{CO_2} \dot{G}_{CO_2} + \Delta H_{CO} \dot{G}_{CO} \qquad 3\text{-}4$$

Here, ΔH_{CO_2} and ΔH_{CO} are the net heat of complete combustion per unit generated of carbon dioxide and carbon monoxide in kJ/kg, respectively. Values of ΔH_{CO_2}= 13,300 kJ/kg (5,720 BTU/lb) and ΔH_{CO} = 11,100 kJ/kg (4,780 BTU/lb) are used to approximate the mix of combustible materials (see Section 3.2) found in the ESS equipment. $\dot{G}_{CO_2}$ and $\dot{G}_{CO}$ are the gas generation rates measured in the FPC duct in kg/s.

Chemical measurements are assumed to have an uncertainty of ±20%, which is a combination of the typical sources of uncertainty for ordinary combustible products [24, 25, 26] and the carbonate species developed during thermal runaway of a Lithium-ion battery [27]. INERIS noted that the uncertainty was at least 10% for a small format polymer battery [28] during bench-scale testing with a Fire Propagation Apparatus (FPA) [29]. Zhang suggested that oxygen consumption measurements can be corrected by accounting for the presence of carbonate species resulting from degradation of the battery electrolyte [30]. However, this correction is more appropriate for bench-scale testing and requires a detailed knowledge of the electrolyte composition and resulting combustion process. The magnitude of the measurement error related to the battery chemistry is difficult to generalize in a large-scale environment as it depends on the quantity of batteries involved in a fire and can change significantly as the fire develops. The bulk net heat of combustion, as detailed in Section 3.2, also changes depending on the quantity of combustibles (batteries, plastic module components, wire insulation, etc.) contributing to the fire at any specific time.

It should be noted that the chemical heat release rate based on oxygen consumption calorimetry was also calculated but is not reported. The paramagnetic O_2 analyzer used to measure the depletion of oxygen within the FPC duct was susceptible to linear analyzer drift and baseline shifting during these tests. This may be due to the long test duration (often exceeding 3 hours) and high air dilution rates required for the 5-MW and 20-MW FPCs. Similar measurements errors were not observed for the CDG calculations due to significantly better resolved signals for CO and CO_2 concentrations.

3.4.4.2 Total Energy

Unlike testing under an FPC, time-resolved heat release rates cannot be determined for sprinklered testing conducted under a ceiling. There are significant transport delays and mixing with ambient lab air that occur between the fire source and the calorimetry measurement station. However, the total energy released during the test is calculated by integrating the chemical HRR curve up to test termination. After the test is terminated, an exponential best fit curve of the decay portion of the test data is used to estimate the tail portion of the HRR and again integrated to yield the total energy released. These two values are added to provide a value for the total energy released during the test. For error analysis, it is assumed that the total energy up to test termination has ± 20% error (see Section 3.4.4.1) and the post-test curve fit data have ±50% error. Convective energy is not reported for sprinklered tests due to the unknown cooling effect of the water spray before the combustion gases reach the calorimetry location.

3.4.4.3 Chemical Heat Release Rate Calculated from Radiation Measurements

Far-field radiation measurements were used for all intermediate- and large-scale tests to estimate the total chemical HRR to allow for comparison between free burn and sprinklered tests. The HRR of a fire test conducted under a fire products collector can be reasonably determined in real-time since there is minimal lag or smearing in the collection of the fire plume gases. The sprinklered Li-ion battery ESS fire tests were conducted under the movable ceiling. Though the total chemical heat released during the fire can be determined from the calorimetry data based on the fire plume gas collected from the exhaust duct above the ceiling, a significant time delay and entrainment of ambient lab air exists due to the long travel time of the fire plume from the fire location to the gas analysis station. The time delay and smearing effect of fire plume prevents using the calorimetry-based heat release rate data in the heat

flux evaluation. Instead, for the sprinklered fire test, the HRR is derived from the far-field radiative heat flux measurement by assuming the fire behaves as a point-source for thermal radiation:

$$\dot{Q} = \frac{4\pi r^2 \dot{q}_p''}{\chi_r} \quad 3\text{-}5$$

where χ_r is the radiant fraction of the fire, which can be calculated in real-time from the convective and chemical heat release rate under free burn conditions as shown in Eqn. 3-6. Here $\dot{Q}_c$ is the convective HRR, t_0 and t_e provide the time bounds of heat release rate considered in the calculation.

$$\chi_r = 1 - \int_{t_o}^{t_e} \dot{Q}_c \Big/ \int_{t_o}^{t_e} \dot{Q} \quad 3\text{-}6$$

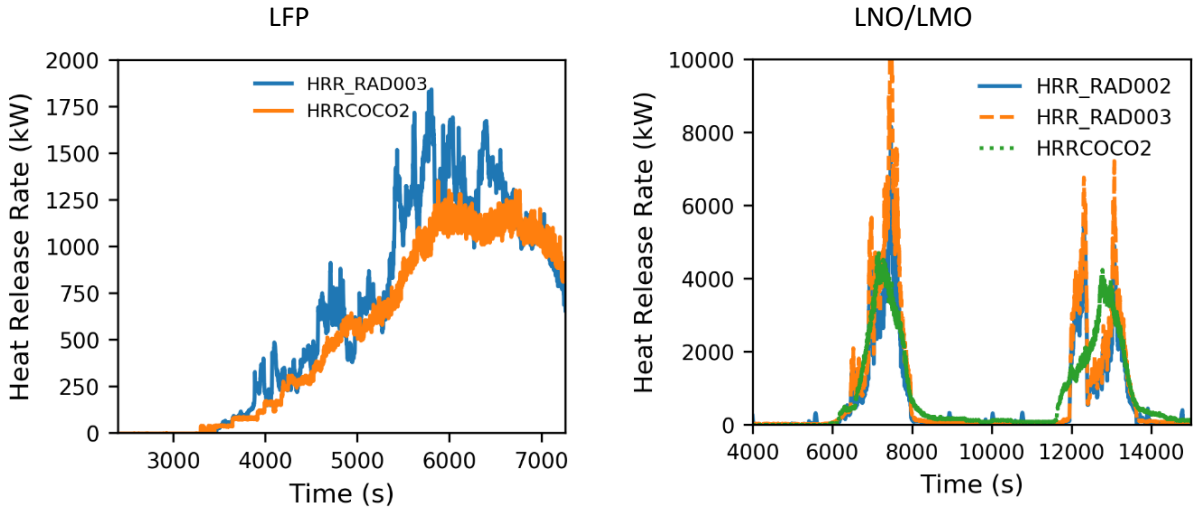

Figure 3-9: Chemical heat release rates calculated based on CO/CO_2 calorimetry and radiation measurement, sprinklered LFP test (left) and sprinklered LNO/LMO test (right).

Figure 3-9 shows the chemical heat release rate determined based on the CDG calorimetry, and the far-field radiative heat flux. Additional measurement details including radiant fraction and heat flux measurement locations can be found in Section 6.2.3.3. Comparing the heat release rate based on the CDG calorimetry and radiation measurement, the HRR based on the calorimetry shows a significant delay and less fluctuation due to the smearing effect, and a relatively slower increase rate, such as around from 4000 to 5500 s in the sprinklered LFP test. Therefore, the HRR for the sprinklered tests is determined based on the radiative heat flux measurement using Eqn. 3-5.

3.4.4.4 Estimation of Near-field Heat Flux using a Multi-point Source Model

A primary consideration in this project was the near-field heat flux imposed on objects surrounding an ESS fire, specifically objects within 0.9 m (3 ft). The large fire size and a close distance of the target location required consideration of the view angle of fire. For this purpose, this study utilizes a Multipoint Source (MPS) Model similar to the approach used by Zhou et al. [31]. The MPS was originally developed

by Hankinson and Lowesmith [32] for jet fires and is extended to optically-thin, buoyant turbulent fires by Zhou et al. [31]. In this study, a similar model is applied to calculate the radiative heat flux of significantly larger fires compared to those examined previously. Theoretically, for larger fires, the approach of Modak [33] considers radiation absorption and may better simulate such fires. However, the test configuration of these fires is complex; a simple radiative profile with a single adjustable parameter and optically-thin radiative characteristic is assumed in the current approach for the large-scale fire tests. This approach under-predicted the measured near-field heat flux for the intermediate-scale testing, and the discrepancy was addressed by including surface reradiation in the model. Such an approach is expected to capture the main feature related to the near-field radiative heat flux. A complete description of the MPS model as applied to this study can be found in Appendix A.

3.4.4.5 Prediction of Sprinkler Response

A theoretical method to calculate the response time of sprinkler links to rack storage fires was developed by Kung et al. [34]. This method is used here to compare the predicted sprinkler operation time for a free burn fire test under an FPC to the actual sprinkler operation time observed in a sprinklered fire test. An outline of the method, which can be found in Reference [35], is also provided below.

The thermal response of sprinkler links can be found from a simple balance between convective heat transfer to the link and heat stored in the link for cases when thermal radiation can be neglected. The governing equation can be expressed as [36, 37]

$$\frac{dT_s}{dt} = \frac{v^{1/2}(T - T_s)}{RTI} \tag{3-7}$$

where T_s is the temperature of the simulated link, T is the ceiling gas temperature, v is the gas velocity, and RTI is the thermal response index of the simulated link. To determine the link temperature, both the gas temperature and velocity under the ceiling are required. For testing under the 5-MW FPC, where no ceiling is present, these values can be estimated using well-known plume laws for plume centerline excess gas temperature [38, 39], ΔT_c, and centerline velocity, v_c:

$$\frac{\Delta T_c}{T_a} = A g^{-1/3}\left(c_p \rho_a T_a\right)^{-2/3} Q_c^{2/3} (z - z_o)^{-5/3} \tag{3-8}$$

$$v_c = B g^{1/3}\left(c_p \rho_a T_a\right)^{-1/3} Q_c^{1/3} (z - z_o)^{-1/3} \tag{3-9}$$

Here, c_p is the specific heat of the plume gases, T_a and ρ_a are ambient temperature and density, z is the plume height above the top surface of the fuel array, and z_o is the virtual origin location relative to the top surface. The constants A and B have values of 11 and 4.25, respectively. The convective heat release rate, Q_c, is calculated as shown in Eq. 3-3.

While there are no known studies to determining the virtual origin of an ESS fire, it is reasonable to assume the virtual origin elevates above the floor level as a function of increasing fire size similar to a

warehouse fire. For a two-tier rack storage array [i.e., 3.0 m (10 ft)] the virtual origin correlates with the convective heat release as [34]

$$z_o = -1.6 + 0.094\dot{Q}_c^{2/5}, \qquad 3\text{-}10$$

where z_o is in m and Q_c must be entered in kW.

Using the above equations, the link temperature during the free burn fire tests was calculated for two generic sprinkler types: quick-response {RTI = 28 (m-s)$^{1/2}$ [50 (ft-s)$^{1/2}$]}, and standard response {RTI = 170 (m-s)$^{1/2}$ [300 (ft-s)$^{1/2}$]}. Link operation is then predicted as the time after ignition at which the link reaches a specified value, i.e., 74°C (165°F) for this project.

3.4.5 Module Data

The manufacturer that donated the ESS equipment also provided software and hardware which provided access to the module balancing board (MBB). This board is typically a primary component of the battery management system (BMS) that measures the voltage at every series connection and the temperature within the module. Table 3-3 lists the quantity and general location of the MBB measurement for both module types. The exact type and location of instrumentation is not known. However, in private communication, the manufacturer noted that these measurements are acquired to observe trends[ii] within the module to determine if corrective action should be taken by the BMS. For the purpose of this project, the MBB data were used to gain additional insight into the voltage and temperature response of the ignition module for each test.

A complete set of data is available in the Appendices for each test. Much of the data provide redundant information with regard to the heating of the module as a means of ignition and only select measurements locations are presented in the body of this report.

[ii] These instruments are not calibrated in accordance with ISO/IEC 17025.

Table 3-3: MBB measurement types and locations

	LFP Module	LNO/LMO Module
Temperature	Five locations*, representing: • Front of module, bulk • Center of module, bulk • Back of module/bulk • Positive terminal† (represents front module temp) • Negative terminal† (represents back module temp)	Four locations*, representing: • Front of module • Center of module • Back of module • MBB (printed circuit board)
Voltage	• Battery level voltage at 13 locations • Module level voltage	• Battery level voltage at 15 locations • Module level voltage

*The listed location reflects the actual orientation of the module installed within the ESS rack along the side of the module facing the horizontal center of the rack. The lone exception is the MBB location which is acquired on the printed circuit board on the face of the module.
†Measurement location used to represent front and back of module. Similar temperatures observed at other measurement locations.

3.5 Fire Fighter Intervention

At the end of each test, laboratory staff determined if fire suppression water was needed to cool the tested equipment to expedite disposal efforts. This project was not intended to evaluate firefighting tactics in the event of an ESS fire and the approach and quantity of water used was not documented. Numerous factors complicate comparison of firefighting tactics in a controlled laboratory environment to a real-world event, including access to the involved equipment, room conditions (e.g., smoke) and geometry, and access to fire protection equipment and water.

4. Small-scale Ignition Testing

Small-scale testing was conducted on single modules to assess the likelihood of thermal runaway leading to a self-propagating fire for both the LFP and LNO/LMO chemistries, Figure 4-1. To properly evaluate the hazard of an ESS fire and subsequent performance of sprinkler protection, an overheat ignition scenario was selected to induce thermal runaway of several batteries within a module. Examples include impact from a fork truck, a module dropped before being installed within an ESS, or a small fire occurring adjacent to the ESS. This approach eliminated the need to access the inside of the module and was more straightforward than an overcharge or mechanical damage (e.g., puncture) event. Ultimately, all these options result in similar thermal damage to the separator material within the batteries leading to thermal runaway.

There is an important distinction between an ignition scenario for the evaluation of fire protection systems and one to evaluate the abuse tolerance of a battery or module design. Abuse tolerance targets the potential for abuse conditions to cause thermal runaway or a subsequent fire in the first place. To develop protection guidance the goal of the selected ignition method is to develop a self-propagating fire. Focusing on a developed fire greatly increases the confidence in protection guidance by avoiding specific details on how the fire was initiated.

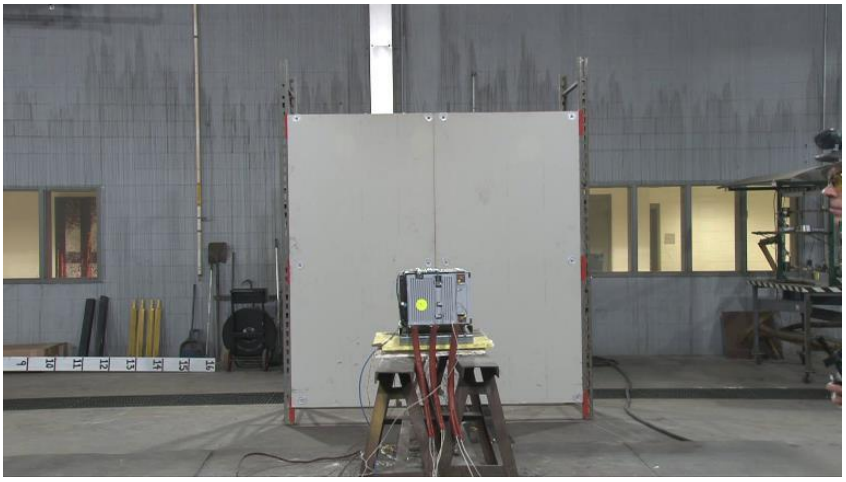

Figure 4-1: Example of single-module ignition test

4.1 Instrumentation Layout

The ignition test was conducted under a 5-MW FPC. Instrumentation consisted on two thermocouples located on each of four sides of the battery module as shown in Figure 4-2 for the LFP module and Figure 4-3 for the LNO/LMO module. In addition, convective and chemical heat release rates were measured in the FPC exhaust gas flow. Specification for the instrumentation and discussion on the analysis methods can be found in Section 3.4

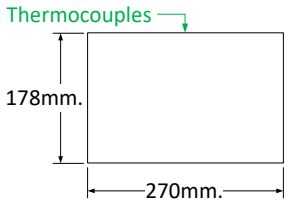

Front elevation view

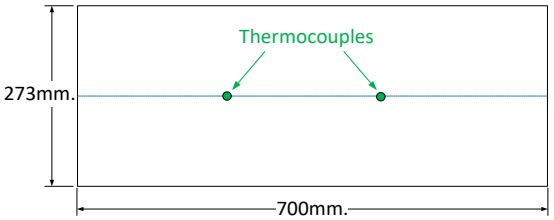

Plan view

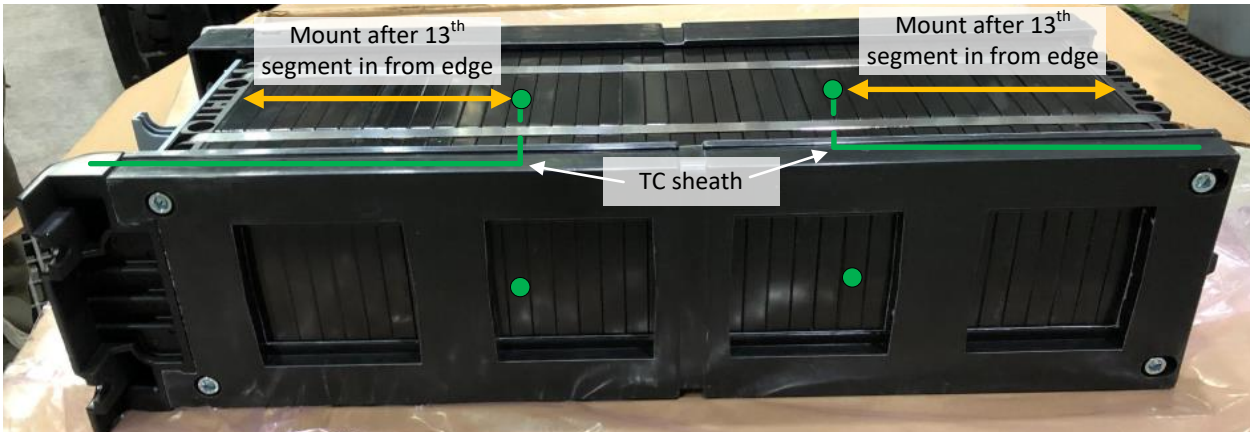

Figure 4-2: Thermocouple layout, LFP

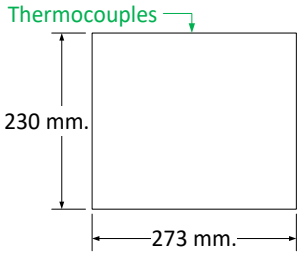

Front elevation view

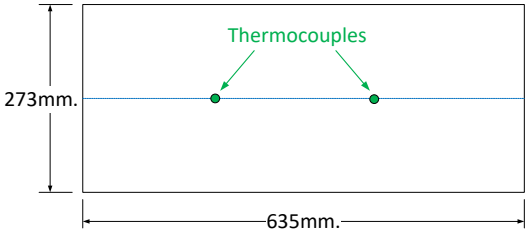

Plan view

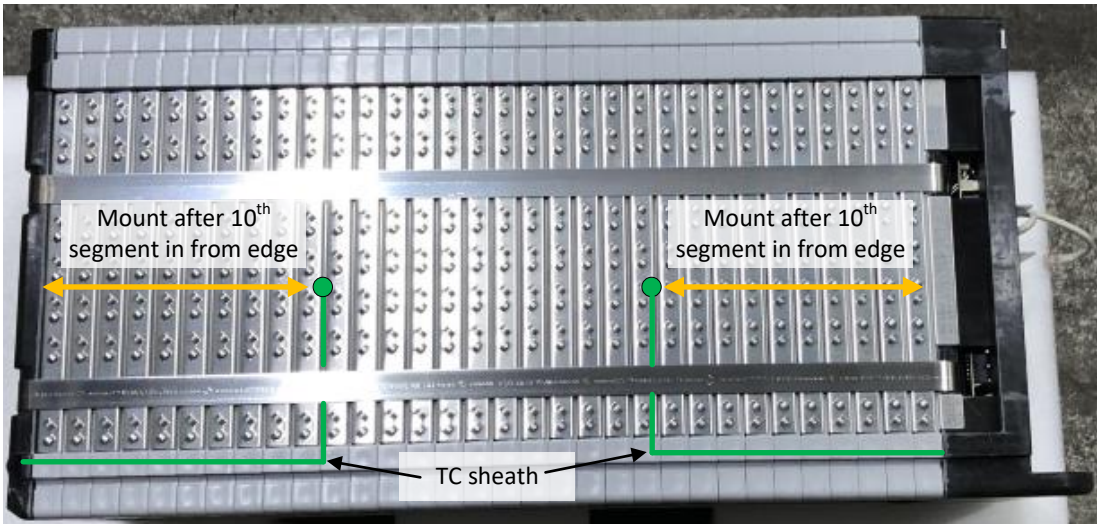

Figure 4-3: Thermocouple layout, LNO/LMO

4.2 Ignition

Ignition was accomplished with three flat bar heating elements 25 mm wide × 76 mm long (1 in. × 3 in.) mounted to the underside of the battery module, as shown in Figure 4-4. The heaters were rated up to 900 W each with a 240 V supply (Watlow Supply, Inc., Firebar, WH-FSP-1210WK-8). All three heaters were connected to a controller (Fuji Electric PXR4-TCY-GVSA1) set to provide a temperature ramping rate of 5°/min up to a maximum of 350°C (660°F). The thermocouple providing feedback to the controller was mechanically fastened to the bottom of the module between two of the heaters, 150 mm (6 in.) in from the face of the module. This location provided a better approximation of the module temperature as opposed to directly controlling the heater temperature due to the significant differences in the thermal mass. The ignition scenario provided a reliable heating condition without requiring internal access to the battery module. The heating source remained active until sustained burning of the module was observed. There is no expected impact on the test outcome due to localized heating of a single module. Subsequent involvement of nearby modules is driven by heat produced from burning of the ignition module, which mitigates the need for electrically connecting the modules. This approach is consistent with recent testing from DNV-GL [12] and simulates an overheat abuse condition resulting in ignition of combustible vent gases.

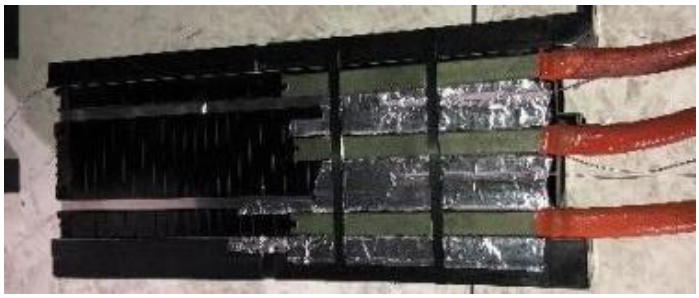

Figure 4-4: Ignition heater layout along bottom of module.

A supplemental premixed propane-air pilot flame was also included for the LFP modules to ensure ignition of the vent gases, Figure 4-5. The pilot flame was not present during the single module testing described in this section but was present in all subsequent tests detailed in Sections 4 through 6. Propane was supplied at a rate of 2.15 L/min (0.08 ft^3/min) with sufficient combustion air to provide a stable blue flame. The combustion nozzle was offset 76 mm (3 in.) from the face of the ignition module at the base of the ESS rack. At that distance the pilot flame exposed the plastic face plate of the module to a 0.8 kW/m^2 (4.2 BTU/ft^2/min) heat flux based on preliminary measurements.

Figure 4-5: Supplemental pilot flame used to ensure ignition of vent gases for the LFP modules.

The need for a supplemental pilot flame to ensure ignition of the LFP vent gases can be seen in Figure 4-6. During preliminary single module testing without a pilot flame, the LFP batteries exhibited significant variability in the time to ignition, ranging from 45 s to 7 min after venting was observed, if ignition occurred at all. The LNO/LMO batteries produced sparks that consistently ignited the vent gases.

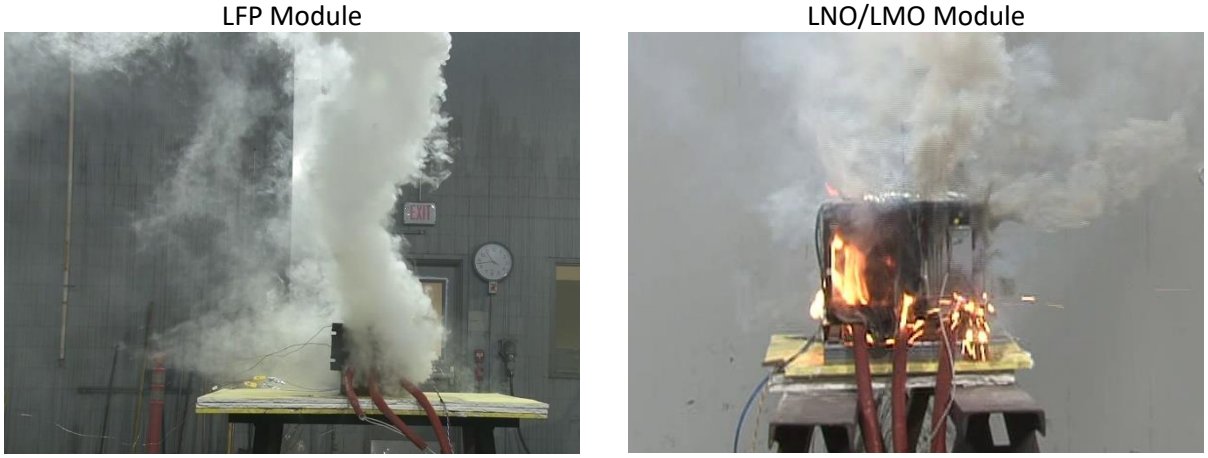

Figure 4-6: Example of LFP (left) and LNO/LMO (right) battery response to abuse conditions. LFP batteries vented a thick white smoke and sometime required an external pilot flame to ignite, whereas LNO/LMO batteries generate sparks that consistently ignited vent gases.

It should be noted that an internal ignition source (i.e., within the ESS rack) is more suitable than an external ignition source (i.e., outside of the rack) to achieve the project goal of determining sprinkler protection guidance. While fire testing conducted outdoors has shown an increased fire hazard using an external ignition source [11], for an indoor ESS installation, the heat generated from the external ignition source alone is likely sufficient to operate a ceiling sprinkler. Thus, external ignition is not a viable option for the present work. In addition, evaluating the potential for unburned vent gases leading to an explosion hazard within a confined environment, e.g., a storage closet, is outside the scope of this project. In this case, the overheat abuse condition would need to be accomplished with a non-flaming ignition source, such as heaters affixed to the module casing or individual batteries as was used in previous testing by Ditch [13].

4.3 Results

For both tests, the external heating source caused thermal runaway reactions in the batteries of both module chemistries. Sparks generated by the LNO/LMO batteries consistently ignited the vent gases, while the LFP batteries required a pilot flame to ensure ignition. Once ignited, the fire spread to involve the entire module with the LNO/LMO module producing a higher peak HRR and total energy released.

4.3.1 Single Module Test Overview

Flame propagation for both chemistries occurred from the front of the module exposed to the heaters to the back of the module, as the batteries were heated and underwent thermal runaway. Figure 4-7 shows an example of the fire development for the LNO/LMO module where it can also be seen that the

module orientation plays a role in the flame location. At 1:11:00 the fire was predominantly on the front half of the module and progressed toward the back as shown at 1:23:40 and 1:35:00.

Figure 4-7: Side view of lateral fire propagation for LNO/LMO module; in this view the ignition heaters are located on the right half (front) of the module and the fire progress from the right to left.

Figure 4-8 shows the fire at near peak HRR, which occurred roughly at 1:17:00 for the LFP module and 1:11:00 for the LNO/LMO module. The peak HRR occurs when multiple batteries vent simultaneously. The added momentum from the venting process is evident from the slanted angle of the flames, which return to the standard axisymmetric flame shape associated with buoyant flames as the venting process completes.

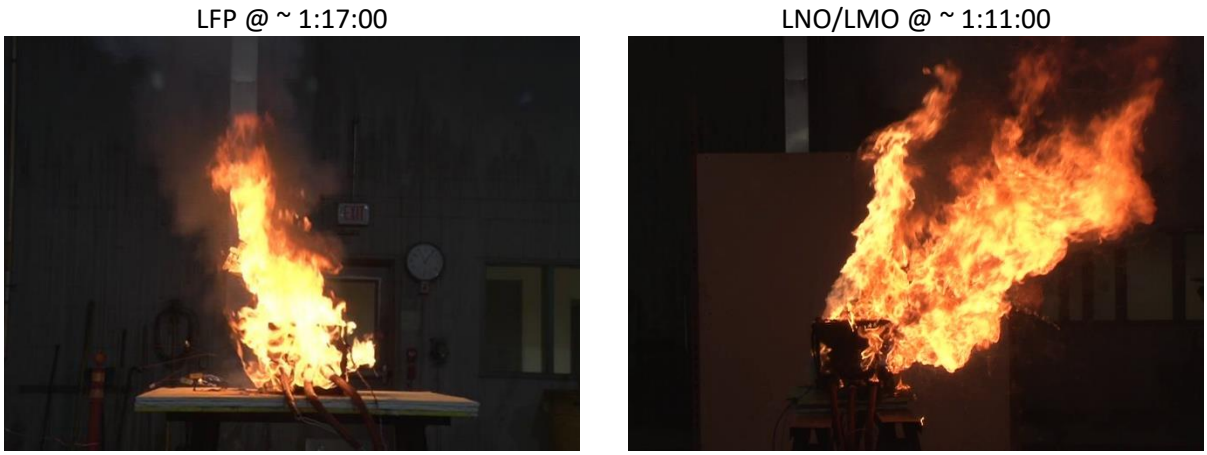

Figure 4-8: Photos of LFP (left) and LNO/LMO (right) at near peak heat release rate. The angle of the flames is due to the momentum of the vent gases exiting the batteries.

4.3.2 TC Measurements

Figure 4-9 presents data from the external TCs for the LFP and LNO/LMO modules. Internal temperatures for the back and front of the module acquired by the BMS are also shown for comparison. Both modules exhibited a similar trend where the temperatures at the front on the module steadily increased leading to battery venting (observed as flames for the LNO/LMO module due to sparks igniting the vent gases). Once vent gases are ignited, the peak measurements are consistent with combustion

temperatures and reflect the progression of fire from the front to the back of the module (see Figure 4-7).

The non-uniformity of the initial heating process leading to battery venting is evident in the data shown in Table 4-1. The highest temperatures were recorded at the bottom-front location which is consistent with the position of the heaters, with values of 295°C (560°F) for the LFP and 143°C (290°C) for the LNO/LMO. The remaining temperatures at the front of the modules were elevated with an average of 74 ± 7°C (165 ± 14°F) for the LFP and 56 ± 7°C (132 ± 13°F) for the LNO/LMO, assuming a variance of one standard deviation. The overall higher temperatures at the time of battery venting of the LFP module suggests those batteries are more abuse tolerant than the LNO/LMO batteries. Away from the heaters, ambient temperatures were recorded at the back of both modules.

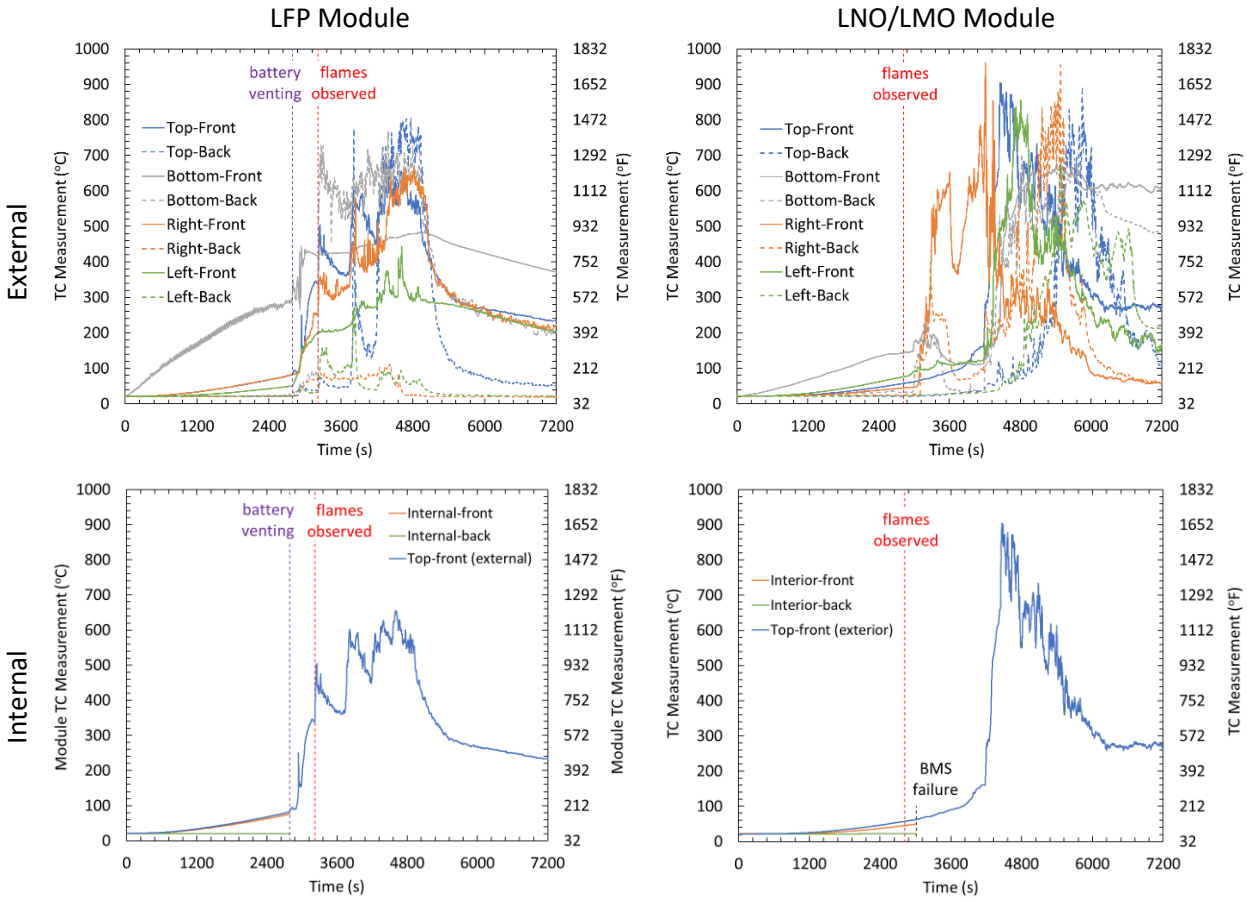

Figure 4-9: TC Measurements on the exterior and interior of the modules; LFP (left) and LNO/LMO (right)

It should be noted that temperatures presented here only indicate the heating trend of the modules, not the temperature of the batteries. Previous small-scale studies under uniform heating conditions report thermal runaway reaction generally occur when Li-ion batteries reach 150°C – 200°C (300°F – 400°F) [19, 40, 41]. The measured temperatures within both the LFP and LNO/LMO modules were less than half that value (Table 4-1) when venting was observed. This wide discrepancy highlights the

difficulty in using BMS data as a means of ignition source control, e.g., prevent thermal runaway reactions. Detailed information is needed for each battery in the module to ensure abuse conditions are positively identified so that preventive actions can be taken.

Table 4-1: TC measurements at time of observed battery venting; LFP module at 2,790 s (46:30) and LNO/LMO module at 2,820 s (47:00).

Location	LFP Module		LNO/LMO* Module	
	Front (°C)	Back (°C)	Front (°C)	Back (°C)
Top	83	22	57	22
Bottom	295	27	143	33
Right	82	21	45	25
Left	52	22	76	23
Internal	80	22	45	22

* Time of venting and observed flames are considered equivalent since the vent gas ignites as part of the thermal runaway process.

Similar internal module temperature data were acquired for all tests conducted in the project, including small through large scale. Tabulated data can be found in Appendix B. For the LFP tests, communication from the MBB circuit board that acquires the BMS data failed after ignition was observed at an average internal temperature of 66°C ± 12°C (150°F ± 23°F) at the front and 23°C ± 1°C (73°F ± 2°F) at the back. However, with the exception of the small-scale LFP test presented in this section, the BMS data failed before ignition was observed in the LNO/LMO tests at an average internal temperature of 50°C ± 4°C (122°F ± 7°F) at the front and 31°C ± 4°C (88°F ± 8°F) at the back. This implies that BMS data will be unreliable in a fire event and that loss of data communication could be one of the indicators of thermal runaway reactions or a developing fire.

Across all test scales (including intermediate and large scale) the time-to-ignition for the LFP modules was 43:30 ± 5:30 and for the LNO/LMO modules was 1:02:35 ± 14:45. The shorter heating time for the LFP modules was due to better contact between the heaters and the mounting surface compared to the LNO/LMO modules and is not necessarily indicative of the battery instability. As shown in Figures 4-2 to 4-4, the mounting surface for the LFP module was smooth and flat allowing for good heater contact, while the LNO/LMO module surface was notched providing an airgap beneath the heaters.

4.3.3 Module BMS Voltage Data

Voltage measurements from the MBB are shown in Figure 4-10. At the start of the test the battery voltages averaged 3.45 ± 0.04 V for the LFP module and 4.01 ± 0.002 V for the LNO/LMO module. These values represent the nominal voltage of all batteries in a series, not of a single battery (Section 3.4.5), and they are generally balanced to within ± 200 mV as provided by the manufacturer. The module voltage was independently measured as 44.9 V for the LFP and 64.3 V for the LNO/LMO representing greater than a 100% SOC based on the target voltages listed in Table 3-1 (LFP = 42.9 V and LNO/LMO = 60 V).

Once the heaters were turned on, some of the battery level voltages exhibited an observable change, though no consistent response was obvious. For example, five of the voltages in the LFP module showed a downward trend leading up to battery venting, while the remaining eight voltages were relatively unchanged. The opposite occurred in the LNO/LMO module, where seven voltages showed an upward trend and the remaining nine were relatively unchanged. Interestingly, the LNO/LMO module voltage exhibited an upward trend which is contradictory to the battery voltage. These results suggest that deviations in the voltages obtained by the MBB can indicate abuse conditions, but do not provide a sufficiently consistent response to positively identify thermal runaway events before venting takes place.

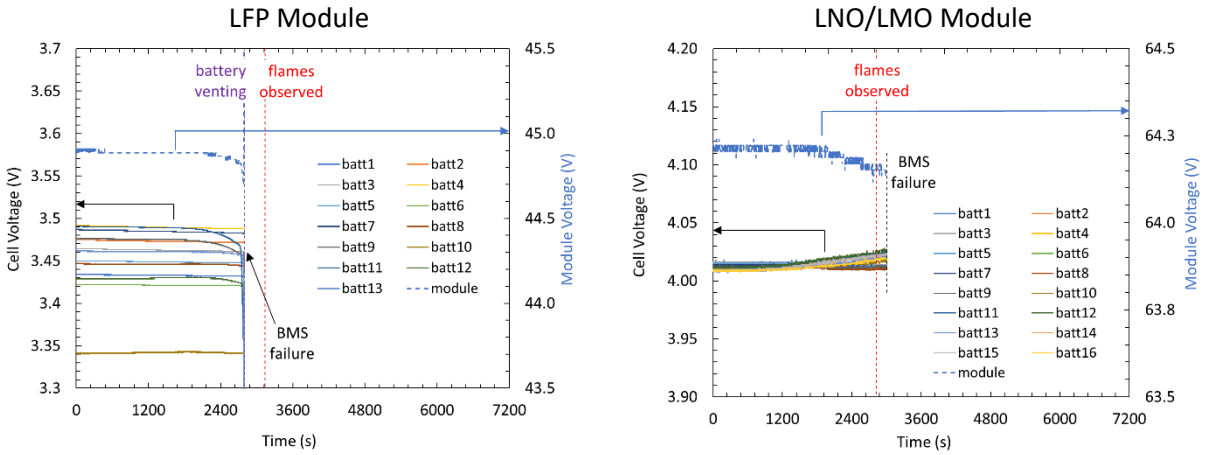

Figure 4-10: Voltage response from BMS for LFP (left) and LNO/LMO (right) tests.

4.3.4 Heat Release Rate

The LNO/LMO module represented a significantly higher hazard with respect to energy release rate during the fire. As shown in Figure 4-11, the peak chemical heat release rate for the LNO/LMO module of 1,023 kW (970 BTU/s) was over double the 413-kW (390-BTU/s) peak for the LFP module. Corresponding convective HRR values were 450 kW (427 BTU/s) for the LNO/LMO and 214 kW (203 BTU/s) for the LFP. A similar difference can be seen in the total energy released, which was calculated by integrating the area under the curves. The LNO/LMO module generated 315 MJ (299 BTU×10^3) of chemical energy, compared to 143 MJ (136 BTU×10^3) for the LFP module. Total convective energy values were 204 MJ (193 BTU×10^3) for the LNO/LMO and 101 MJ (96 BTU×10^3) for the LFP module.

Interestingly the convective HRR is greater than the chemical HRR during the decay phase of the fires, which starts at approximately 5,900 s (1:40:00) for the LNO/LMO module and 4,900 s (1:20:00) for the LFP module. Given the modules are approximately 80-85% by mass non-combustible material, i.e., predominantly metal, this trend can be partly attributed to sensible heat stored by the modules that continues to heat the ambient lab air after the fire has burned out.

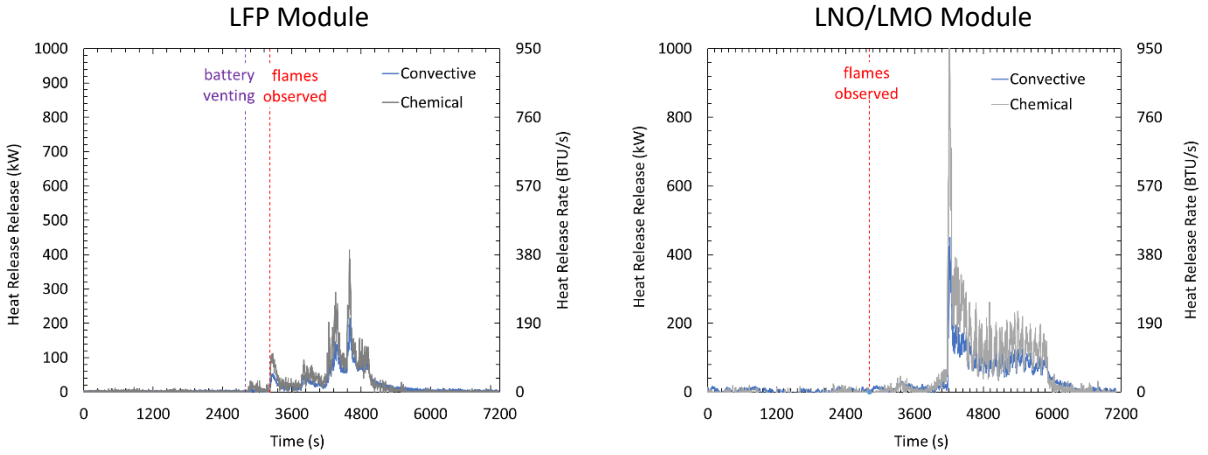

Figure 4-11: Heat Release Rate; LFP (left) and LNO/LMO (right).

A common means of comparing the combustion properties of different fuels is the radiant fraction, which represents the ratio of radiative and chemical energy released. The radiant fraction is calculated as χ_{rad} = 1- (convective HRR / chemical HRR). Figure 4-12 shows the time resolved radiant fraction for both modules. The data series are shown as a 10-s average to minimize noise and truncated to exclude the initial development and decay phase of the fire due to high measurement uncertainty. The average values for both modules over the measurement period shown are χ_{rad} = 0.37 and 0.32. These values are consistent with those of ordinary combustible materials, e.g., plastics.

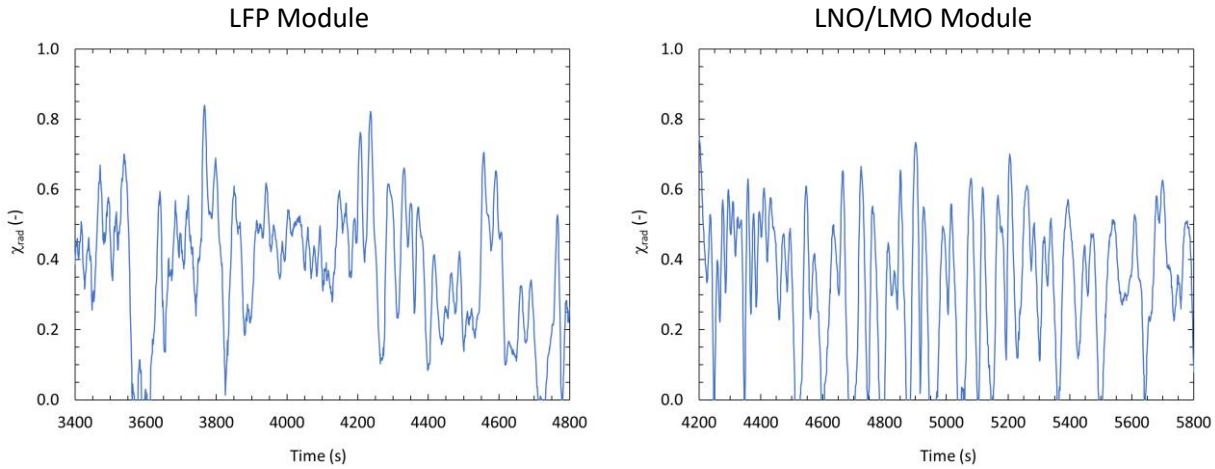

Figure 4-12: Radiative fraction based on convective and chemical heat release rate calculations; LFP (left) and LNO/LMO (right). Data shown as a 10-s average.

4.4 Sprinkler Response Prediction

The predicted response of a sprinkler located directly over the fire was calculated following the method described in Section 3.4.4.5. These predictions can be used to evaluate the impact of sprinkler RTI and ceiling height on the time of sprinkler operation and the corresponding fire hazard of a single module fire. Refer to Sections 5.2.5 and 6.1.2.6 for predictions of a sprinkler system response to a fire involving an ESS system comprised of multiple modules.

Figure 4-13 presents examples of the predicted response of a QR sprinkler link for the LFP and LNO/LMO tests. In these examples the dashed green lines show the sprinkler response for a 4.6 m (15 ft) ceiling height. Table 4-1 compiles calculations for QR and SR sprinklers for ceiling heights ranging from 4.6 m to 7.6 m (15 ft to 25 ft). For the LFP test, the limited fire size was sufficient to operate a QR or SR sprinkler under a 4.6 m (15 ft) ceiling when the fire size was in the range of 110 to 170 kW (104 to 161 BTU/s). However, sprinklers were not predicted to operate when the ceiling was raised to 6.1 m (20 ft) or higher. The larger fire size during the LNO/LMO test resulted in predicted sprinkler operations up to at least 7.6 m (25 ft) for a QR sprinkler and 6.1 m (20 ft) for a SR sprinkler. For both chemistries, the fires begin to burn out shortly after the time of predicted sprinkler operation, suggesting that only a single sprinkler operation would likely occur in a real fire event in a commercial occupancy.

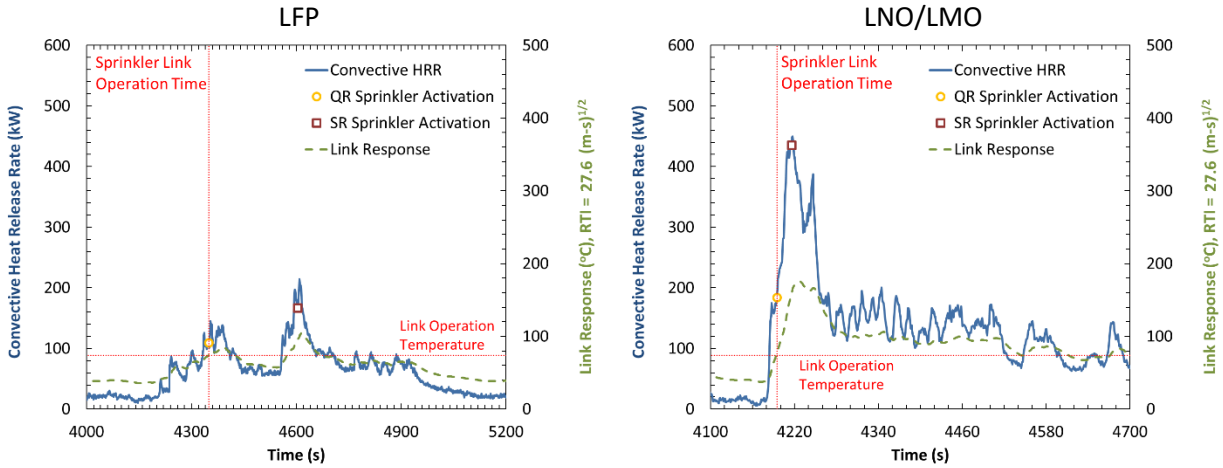

Figure 4-13: Predicted sprinkler response during LFP (left) and LNO/LMO (right) free burn test. Dashed green line shows the response of a QR link installed under a 4.6 m (15 ft) ceiling, directly over the fire.

Table 4-2: Predicted response time and fire heat release rate for ordinary temperature* sprinklers at different ceiling heights. Operation time listed for sprinklers located directly over the fire.

Ceiling Height	QR Sprinklers (RTI = 27.6 m½s½ [50 ft½s½]		SR Sprinklers (RTI = 170 m½s½ [300 ft½s½]	
	LFP	LNO/LMO	LFP	LNO/LMO
4.6 m (15 ft)	4,350 s @ 109 kW (103 BTU/s)	4,195 s @ 184 kW (174 BTU/s)	4,604 s @ 167 kW (158 BTU/s)	4,216 s @ 435 kW (412 BTU/s)
6. 1m (20 ft)	DNO†	4,205 s @ 282 kW (267 BTU/s)	DNO†	4,247 s @ 388 kW (368 BTU/s)
7.6 m (25 ft)	DNO†	4,215 kW @ 430 kW (408 BTU/s)	DNO†	DNO†

* Link activation temperature of 74°C (165°F)
† Predicted sprinkler did not operate

5. Intermediate-scale Fire Tests

Intermediate-scale free burn fire tests were conducted as a screening tool to evaluate the propensity for involvement of the module exposed to the ignition source and subsequent spread to adjacent modules. The results are also used in Section 7.2.1 to determine the relationships between electrical capacity, combustible load, and the overall fire hazard and provide a bound for extending protection guidance to arbitrary ESS equipment not included in this project.

Figure 5-1: Image of six-module fire test with LNO/LMO module

5.1 Instrumentation Layout

Free burn fire tests were conducted under the 5-MW FPC located in the Small Burn Laboratory at the FM Global Research Campus. Instrumentation consisted of 23 thermocouples and four heat flux gages located as shown in Figure 5-2. In addition, convective and chemical HRRs were measured in the FPC exhaust gas flow. Specification for the instrumentation and discussion on the analysis methods can be found in Section 3.4.

TCs were installed as follows:

- TC1 – 6 were fastened to the top of each module at half the width and depth. TC22 was similarly fastened to the bottom of the ignition module, except offset in between two of the heaters. TCHeater was located between the center and the bottom of the ignition module.
- TC7-14 were fasted to the sides of each ‘mock’ module at half the width and depth.
- TC15 – 21 were fastened to the ESS rack. Unless otherwise noted all locations were at half the rack depth.

Heat flux gages were located at the elevation of the third (top) row of modules. All gages had a range of 0-150 kW/m^2 (0-790 BTU/ft^2/min) for the LFP test, while for the LNO/LMO test HFG1 and HFG2 had a

range of 0-100kW/m^2 (0-530 BTU/ft^2/min) and RAD1 and RAD2 had a range of 0-5 kW/m^2 (0-26 BTU/ft^2/min).

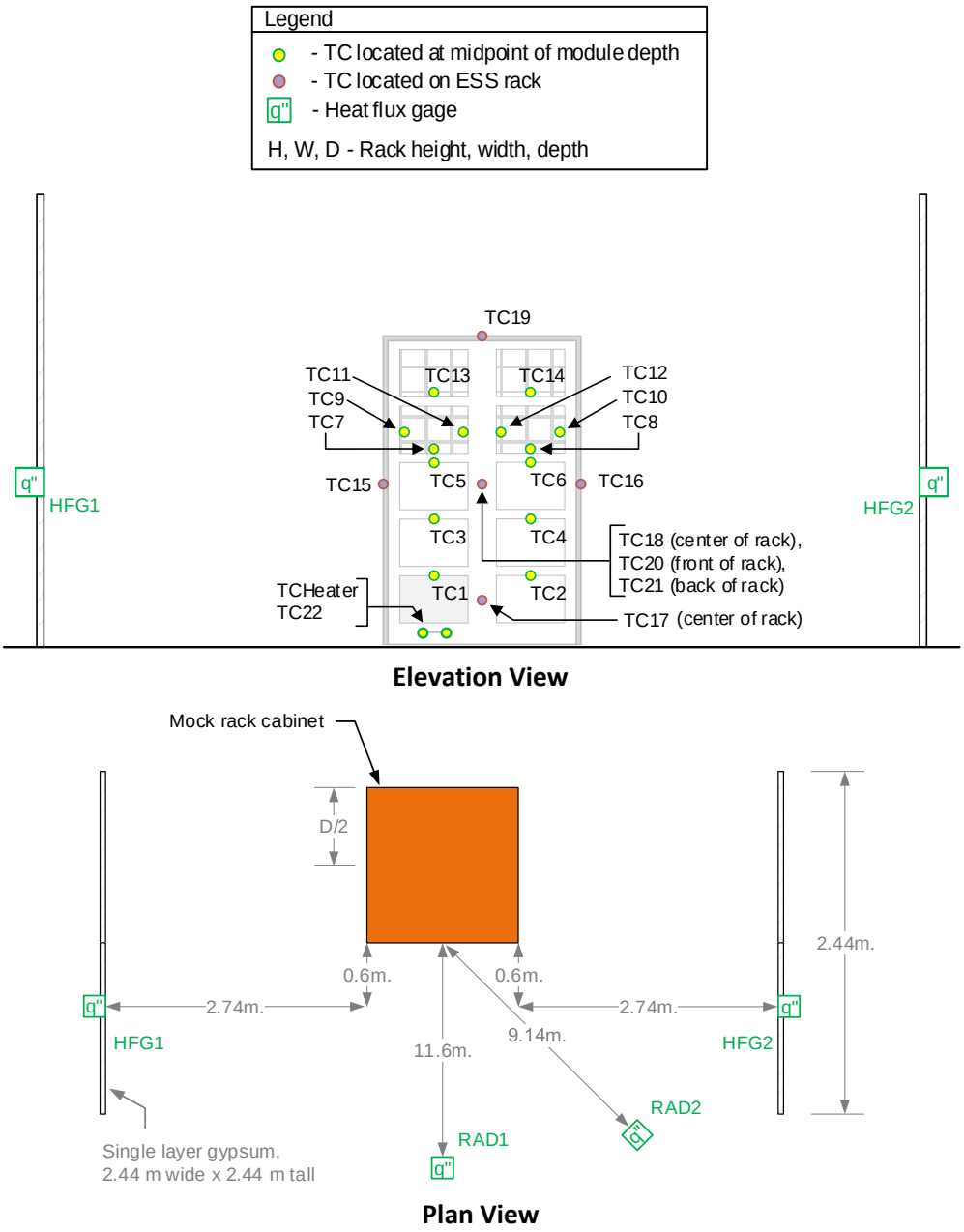

Figure 5-2: Schematics of intermediate-scale free burn fire test and instrumentation layout (not to scale) for LNO/LMO test. Front elevation view shown on top and plan view on bottom. Checkered boxes in elevation view represent the location of 'mock' modules.

Gages were installed as follows:

- On the structure walls, HFG1 and HFG2 were positioned 0.9 m (3 ft) from the ESS rack side for the LFP test and 2.7 m (9 ft) for the LNO/LMO test. For both tests, gages were positioned 0.6 m (2 ft) in front of the ESS rack to improve the view angle of the fire.

RAD1 was located 3.1 m (10 ft) from the rack face for the LFP test and 9.1 m (30 ft) for the LNO/LMO test. RAD2 was offset at an angle of 45 degrees and located 1.7 m (5 ft 7 in.) from the rack face for the LFP test and 9.1 m (30 ft) for the LNO/LMO test.

5.2 Results

Two intermediate-scale free burn tests were conducted following the approach established in the small-scale tests. In both tests, ignition of a single module was sufficient to spread the fire to all modules in the rack; however, there were some differences in the fire progression. During the LFP test, the fire spread vertically to involve all the modules in the stack above ignition before spreading horizontally to adjacent modules, whereas the fire spread horizontally to the adjacent stack before spread vertically in the LNO/LMO test. This contributed to a longer duration fire for the LFP equipment with a lower peak HRR. Ultimately the LNO/LMO equipment presented a higher hazard than the LFP equipment in terms of fire intensity and thermal exposure to the surroundings.

5.2.1 Intermediate-scale Free Burn Test Overview

Figure 5-3 shows photos of the LFP fire development leading to the peak HRR. At 49:30 sustained flames were observed at the face of the ignition module. The fire then spread up the left stack of modules, over ignition, and 1:32:51 marks the predicted time when a quick-response sprinkler would have operated if present (see Section 3.4.4.5). The upper module on the right stack then ignited before the fire progressed downward to involve all the modules in the rack. At 2:13:16 the fire was near its peak HRR and flames were extending approximately 0.6 m (2 ft) above the rack. Flames were predominantly emerging from the open face of the rack as the sheet steel walls of the cabinet (manufactured by lab staff) prevented all but minor flames from escaping through the sides or back walls. As the fire decayed, the modules on the left side (over ignition) burned out first followed by burnout of the modules on the right side. The fire lasted for over 2:30:00 and would have fully consumed the available fuel. Figure 5-4 shows the fire before lab staff extinguished the remaining flames with a fire hose at 3:32:16. A post-test image highlights the heavily damaged structure.

Figure 5-5 shows comparable pictures of the LNO/LMO test. At 0:57:00 flames were observed at the face of the ignition module, several minutes after the initial observation of minor flames underneath the module. The slightly longer time to ignition compared to the LFP module is due to better contact between the heaters and module for the LFP module and is not related to battery reactivity. The LNO/LMO module to the right of ignition then ignited and the fire spread up both stacks of modules simultaneously. 1:11:16 marks the predicted time when a quick-response sprinkler, 4.6 m (15 ft) overhead, would have operated if present (see Section 3.4.4.5). The fire reached its peak HRR around 2:13:16 and flames were extending approximately 1.5 m (5 ft) above the rack. The fire volume was significantly larger than that observed during the LFP test. Figure 5-6 shows that, unlike the LFP test, all modules in the LNO/LMO rack continued to burn throughout the decay phase. By 1:59:00 the lower modules had burned out and at 2:11:47 all modules had burned out. The heat contained within the modules is evident by the orange glow between the modules, which was still observed when the test was terminated at 3:23:30. No firefighter intervention was needed, and the fire lasted for approximately 1:10:00.

00:49:30 1:32:51 2:13:16

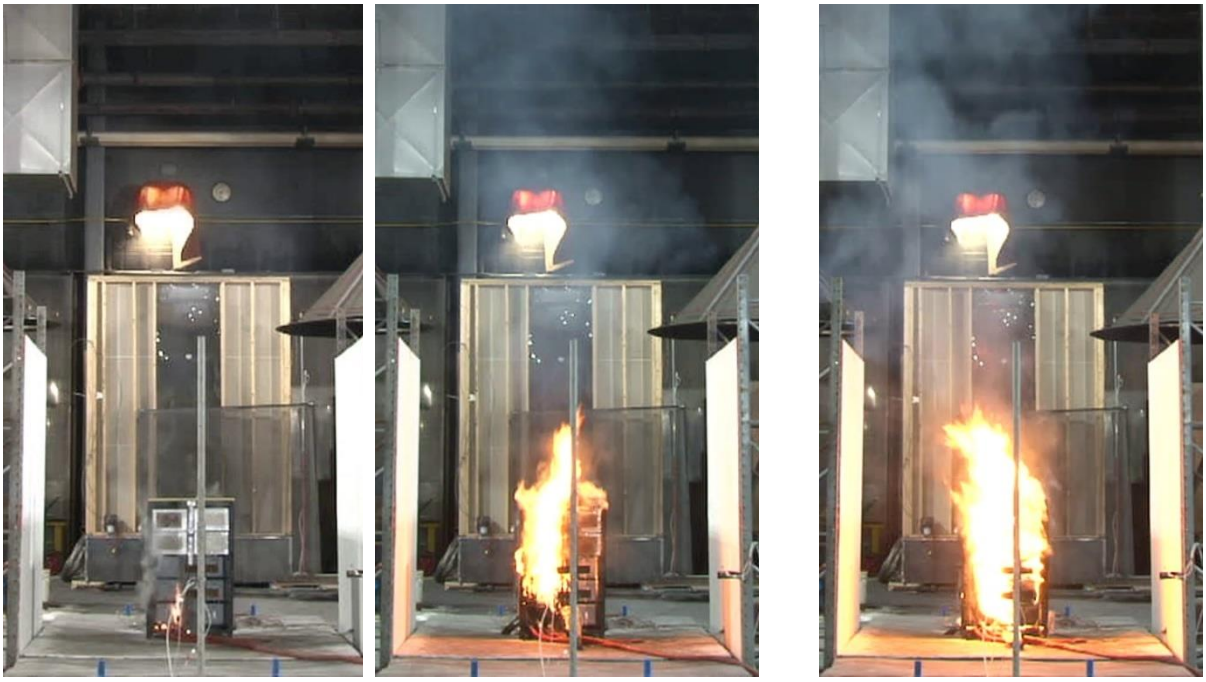

Figure 5-3: Photos of LFP fire development during intermediate-scale free burn test: near time of ignition (left), near time of predicted sprinkler operation (middle), peak heat release rate (right).

3:32:16 Post-test

Figure 5-4: Photos of LFP fire during decay phase immediately before manual extinguishment (left) and post-test (right).

00:57:00 1:11:16 1:29:00

Figure 5-5: Photos of LNO/LMO fire development during intermediate-scale free burn test: near time of ignition (left), near time of predicted sprinkler operation (middle), peak heat release rate (right).

01:59:00 2:11:47 3:23:30

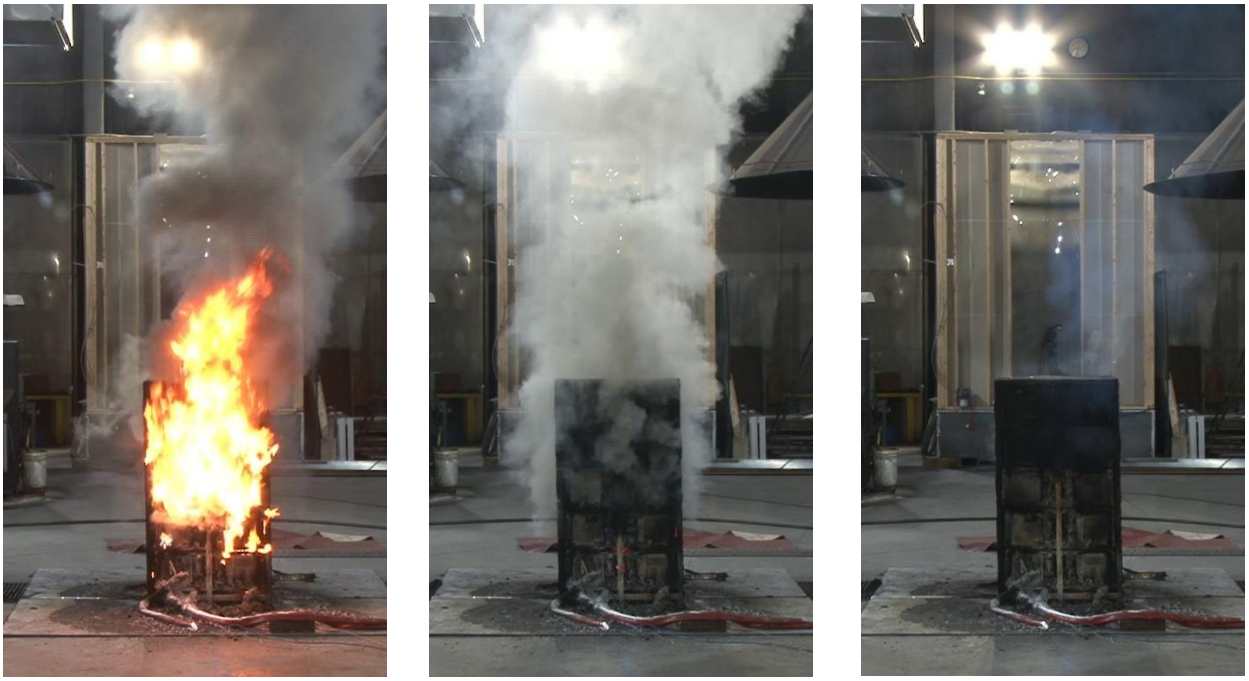

Figure 5-6: Photos of LNO/LMO fire decay phase (left), at burn-out of all modules (middle), and post-test (right).

5.2.2 TC Measurements

Figure 5-7 shows the TC measurements from the modules and racks in the LFP and LNO/LMO tests (measurement locations are shown in Figure 5-2). The temperature trends and magnitudes are very consistent with those that will be observed during the large-scale free burn tests, with the thermal mass of the modules causing a delay in the heating compared to the rack temperatures. Section 6.1.2.2 includes a complete discussion of heating trends in the large-scale tests and a comparison to the intermediate-scale results shown here. To summarize, the peak module temperatures in both tests were in the range of 400 – 600°C (750°F to 1,100°F) and peak rack temperatures exceeded 900°C (1,650°F). The heating trends seen in the mock module data (see Appendix C) are consistent with the observed fire progression within the ESS racks and are not further discussed here.

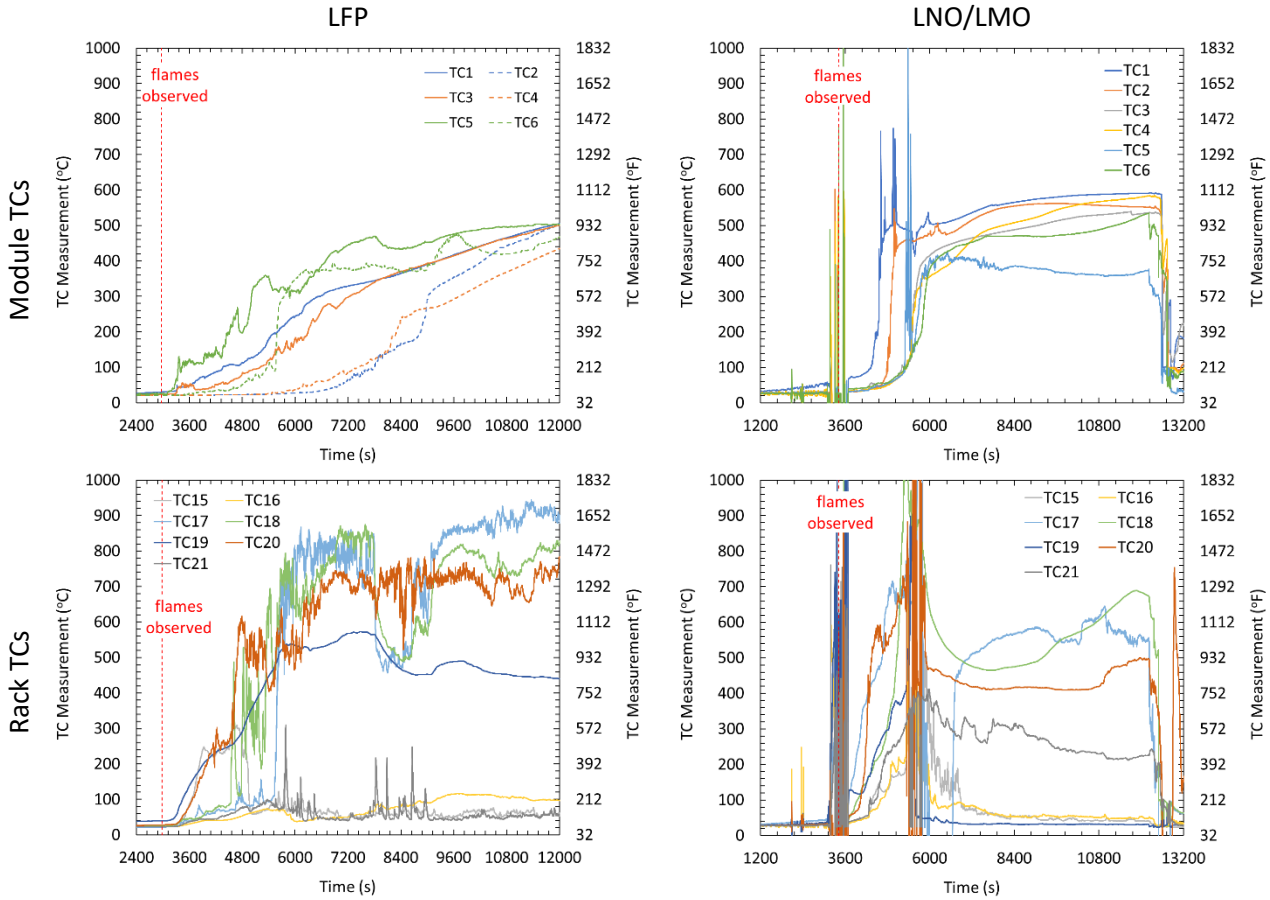

Figure 5-7: TC measurements during LFP (left) and LNO/LMO (right) tests for modules (top) and target (bottom).

5.2.3 Thermal Exposure to Surroundings

Figure 5-8 shows the heat flux to surrounding objects during both tests. As shown in the legends, the gages were positioned between 0.9 and 9.1 m (3.0 and 30 ft) from the closest edge of the ESS rack. Good symmetry with regards to the heat flux trends and maximum values was seen for both tests. For example, HFG3 and HFG4 are mounted on the opposing structure walls with a similar view of the fire and recorded reasonably similar max values with a range of 5.9 – 6.4 kW/m^2 (31.2 – 33.8 BTU/ft^2/min) for LFP and 5.6 – 6.4 kW/m^2 (29.6 – 33.8 BTU/ft^2/min) for LNO/LMO. However, the reader is reminded

that the gages in the LFP test were positioned 0.9 m (3 ft) away as opposed to 2.7 m (9 ft) away for the LNO/LMO test, and thus indicated a smaller source fire. The data shown here are more extensively used to validate the MPS model presented in Section 7.1, which estimates the near-field heat flux as a function of distance from the fire.

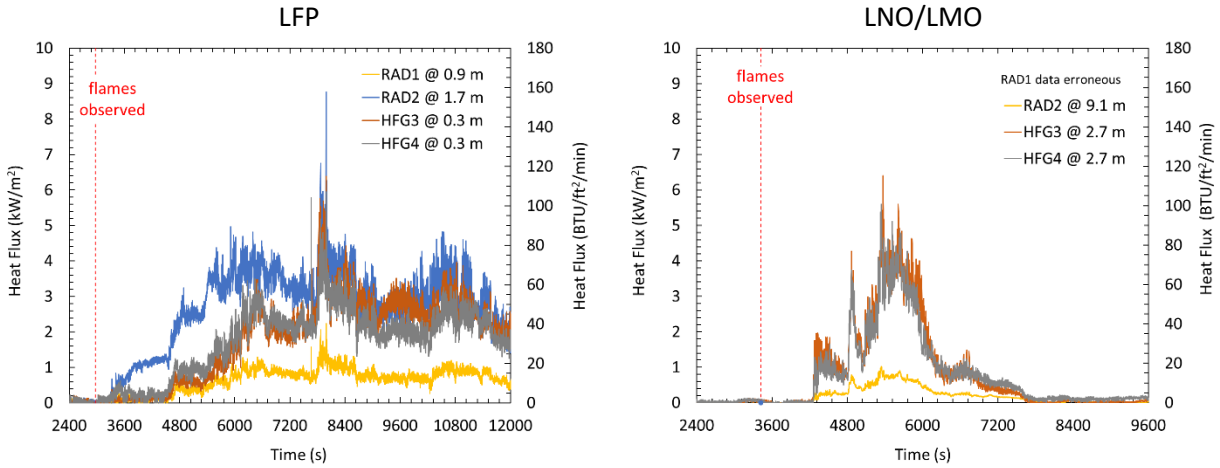

Figure 5-8: Thermal exposure to surroundings during LFP (left) and LNO/LMO (right) test.

5.2.4 Heat Release Rate

Consistent with the small-scale tests, the LNO/LMO modules presented a higher fire hazard with respect to energy released during the fire. Figure 5-9 shows the convective and chemical heat release rate measurements based on the collection of the combustion gases in the 20-MW FPC for both LFP and LNO/LMO tests. The peak chemical heat release rate for the LNO/LMO modules of 1,890 kW (1,790 BTU/s) was over a factor of four greater than the 500-kW (470-BTU/s) peak for the LFP modules. Corresponding convective HRR values were 1,020 kW (967 BTU/s) for the LNO/LMO and 312 kW (296 BTU/s) for the LFP. The LNO/LMO modules released approximately double the total energy during the test than the LFP modules. The LNO/LMO modules generated 2,034 MJ (1,930 BTUx10^3) of chemical energy, compared to 1,152 MJ (1,090 BTUx10^3) for the LFP modules. Total convective energy values were 1,435 MJ (1,360 BTUx10^3) for the LNO/LMO and 758 MJ (718 BTUx10^3) for the LFP modules. These ratios are similar to those of the small-scale results.

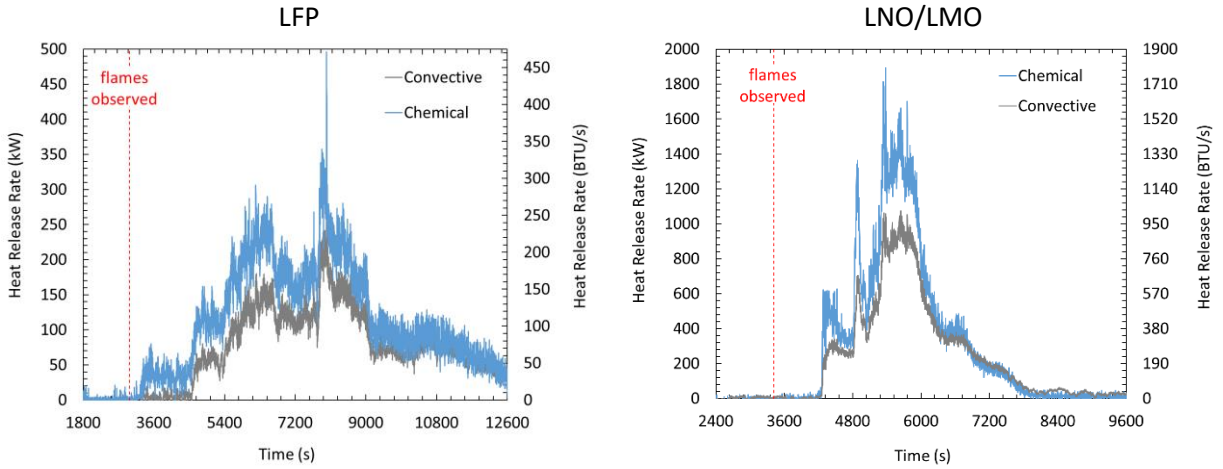

Figure 5-9: Heat Release Rate; LFP (left) and LNO/LMO (right).

5.2.5 Sprinkler Response Prediction

The predicted response of a sprinkler located directly over the fire was calculated following the method described in Section 3.4.4.5. These predictions can be used to evaluate the impact of sprinkler RTI and ceiling height on the time of sprinkler operation and the corresponding fire hazard.

Figure 5-10 presents examples of the predicted response of a QR sprinkler link for the LFP and LNO/LMO tests. In these examples the dashed green lines show the sprinkler response for a 4.6 m (15 ft) ceiling height. Table 5-1 compiles calculations for QR and SR sprinklers for ceiling heights of ranging from 4.6 m to 7.6 m (15 ft to 25 ft). For the LFP test, the initial fire development was sufficient to operate a QR or SR sprinkler under a 4.6 m (15 ft) ceiling when the fire size was approximately 100 kW (95 BTU/s). Raising the ceiling height to 6.1 m (20 ft) resulted in close to a 700 s (11:40) delay, though the corresponding fire size was still in the range of 150 to 200 kW (140 to 190 BTU/s). Sprinklers were not predicted to operate for ceiling heights of 7.6 m (25 ft) or greater. Similar results were seen for the LNO/LMO test, except the higher peak heat release rate allowed for sprinklers to operate under a 7.6 m (25 ft) ceiling.

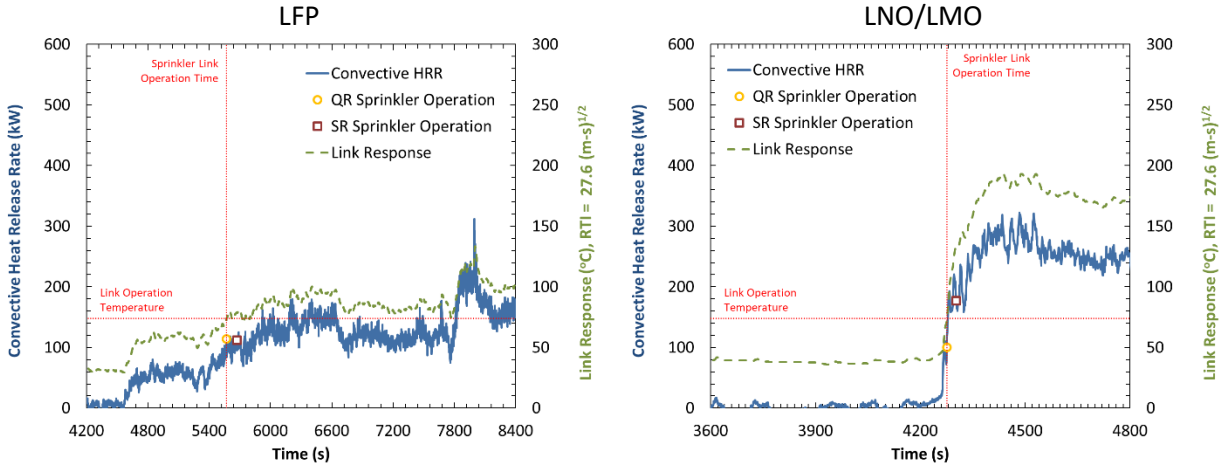

Figure 5-10: Predicted sprinkler response during LFP (left) and LNO/LMO (right) free burn test. Dashed green line shows the response of a QR link installed under a 4.6 m (15 ft) ceiling, directly over the fire.

Table 5-1: Predicted response time and fire heat release rate for ordinary temperature* sprinklers at different ceiling heights. Operation time listed for sprinklers located directly over the fire.

Ceiling Height	QR Sprinklers (RTI = 27 $m^{½}s^{½}$ [50 $ft^{½}s^{½}$])		SR Sprinklers (RTI = 170 $m^{½}s^{½}$ [300 $fts^{½}s^{½}$])	
	LFP	LNO/LMO	LFP	LNO/LMO
4.6 m (15 ft)	5,571 s @ 114 kW (108 BTU/s)	4,276 s @ 100 kW (95 BTU/s)	5,670 s @ 112 kW (106 BTU/s)	4,303 s @ 177 kW (168 BTU/s)
6.1 m (20 ft)	7,850 s @ 206 kW (195 BTU/s)	4,288 s @ 159 kW (151 BTU/s)	7,936 s @ 221 kW (209 BTU/s)	4,351 s @ 255 kW (242 BTU/s)
7.6 m (25 ft)	DNO†	4,330 s @ 228 kW (216 BTU/s)	DNO†	4,421 s @ 295 kW (280 BTU/s)

* Link activation temperature of 74°C (165°F)
† Predicted sprinkler did not operate

6. Large-scale Fire Tests

Large-scale fire tests were conducted with the LFP and LNO/LMO equipment to evaluate the overall fire hazard and performance of sprinkler protection. A free burn fire test was conducted on each chemistry to provide a hazard assessment that is representative of a range of commercial ESS designs. Measurements focused on the fire propagation through the ESS rack, as well as the thermal exposure to adjacent ESS racks and surrounding objects. Sprinklered fire tests were then conducted to evaluate the effectiveness of sprinkler protection at confining the fire to the ESS rack of origin and reducing the exposure hazard. While outside the scope of this project, these data are also available as input for numerical modeling to determine the effect of specific room configurations, such as room dimensions, ceiling height, and ventilation.

6.1 Free Burn Fire Tests

Two large-scale free burn fire tests were conducted with full ESS racks located in an open-air environment under a 20-MW FPC. This approach allowed for real-time measurement of the chemical and convective heat release rate from the fire and magnitude of radiant exposure to surrounding objects, which was used to compare the relative hazard of the LFP and LNO/LMO systems. Mock rack extensions were installed on either side of the ESS rack to further evaluate the thermal exposure to ESS equipment adjacent to a fire. The heat release rate data were also used to predict the response of various sprinkler system designs, e.g., response time index (RTI) and installation height, to expand the application of the sprinklered fire test results beyond the tested condition.

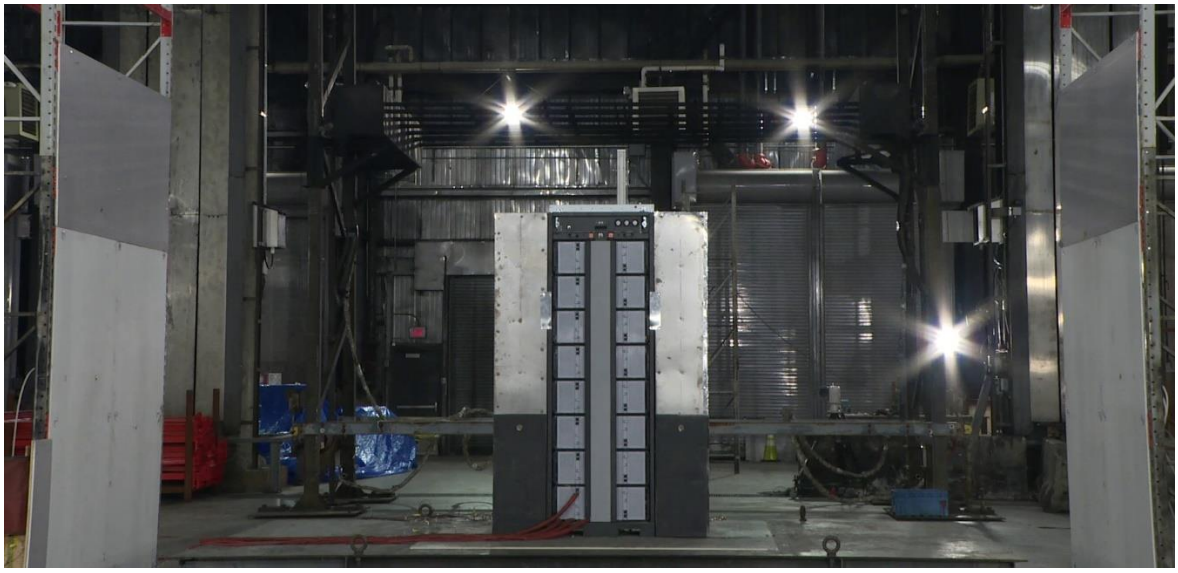

Figure 6-1: Example of full-scale free burn test setup for the LNO/LMO module. Mock racks are located on either side of the ESS rack to measure the exposure hazard to adjacent equipment and representative structure walls are located across a 2.7-m (9-ft) separation to measure the exposure to surrounding objects.

6.1.1 Instrumentation Layout

Free burn fire tests were conducted under the 20-MW FPC located in the Large Burn Laboratory at the FM Global Research Campus. Instrumentation consisted of 38 thermocouples and seven heat flux gages located as shown in Figure 6-2. In addition, convective and chemical heat release rates were measured in the FPC exhaust gas flow. Specification for the instrumentation and discussion on the analysis methods can be found in Section 3.4.

TCs were installed as follows:

- TC1 – 16 were fastened to the top of each module at half the width and depth. TC Heater was similarly fastened to the bottom of the ignition module, except offset in between two of the heaters.
- TC17 – 27 were fastened to the ESS rack. Unless otherwise noted all locations were at half the rack depth.

Plate thermometers were installed as follows:

- PT1 – 10 were mounted to the front face of the mock ESS racks at half of the width. PT3, 4, 7, and 8 were offset 76 mm (3 in.) due to the location of the heat flux gages. Refer to Section 3.4.3.2 for details on the construction and analysis methodology.

Heat flux gages had a range of 0-150 kW/m^2 (0-790 $BTU/ft^2/min$) and were installed as follows:

- On the mock ESS racks, HFG1 – 2 were located at 1/3 the rack height and HFG3 was located at 2/3 the rack height.
- On the structure walls, HFG4 and 7 were located at 1/3 the rack height, and HFG5 was located at the full rack height. The structure walls were positioned 2.7 m (9 ft) from the ESS rack as shown in Figure 3-8.
- HFG6 was located at 1/2 the rack height at 11.6 m (38 ft) from the face of the ESS to provide far-field measurements of the flame radiation.
- HFG8 was located behind 1/2 the rack height at 2.7 m (9 ft) from the back of the ESS rack.

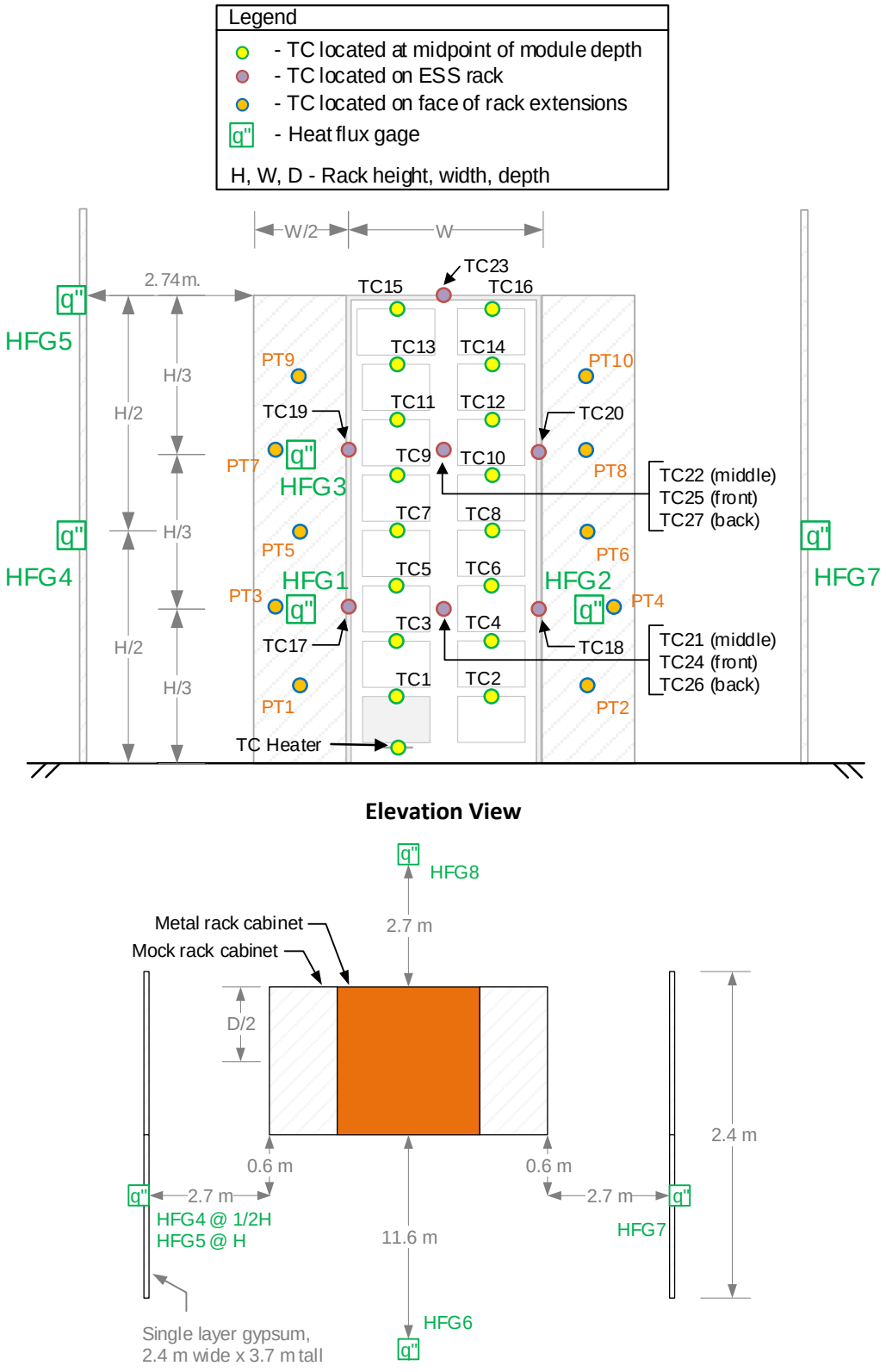

Figure 6-2: Schematics of free burn fire test and instrumentation layout (not to scale). Front elevation view shown on top and plan view shown on bottom.

6.1.2 Results

Similar to the small- and intermediate-scale tests, the LNO/LMO equipment presented a higher hazard than the LFP equipment in terms of fire intensity and thermal exposure to the surroundings. Aside from the larger magnitude of the LNO/LMO fire, the initial fire development leading to full involvement of all modules in the rack was similar between the two chemistries. However, the LNO/LMO modules exhibited an unusually extended decay phase where the fire transitioned into 'furnace like' combustion that was contained within the rack. Conversely, the LFP modules exhibited a more traditional decay phase leading to burnout.

6.1.2.1 Free Burn Test Overview

Figure 6-3 shows photos of the LFP fire development leading to the peak HRR. At 37:15 sustained flames are observed at the face of the ignition module. The fire then spreads up the lower half of the left stack of modules, over ignition, and 38:35 marks the predicted time when a quick-response sprinkler would have operated if present (see Section 3.4.4.5). By 1:11:05 the fire has spread to involve all the modules in the rack and the flames are extending approximately 10 ft (3.1 m) over the rack. To a lesser degree flames are also observed exiting the seams on the top and back of the rack highlighting the exposure potential on all sides of the rack. The fire then begins to burn out naturally and at 1:38:15 involves only the modules on the upper half of the rack, Figure 6-4. At 2:15:45 the fire self extinguishes. The rack structure appears to be heavily damaged with a significant amount of heat distortion.

Figure 6-5 shows comparable photos of the LNO/LMO fire development. At 1:00:20 flames have attached to the plastic face of the ignition module, an event which occurred approximately 1 min after the initial observation of flames. The slightly longer time to ignition compared to the LFP module is due to better contact between the heaters and module for the LFP module. The fire then appears to spread up the center of the rack involving the modules on both the left and right side. The time of 1:10:10 is when a quick-response sprinkler would have been predicted to operate if present (see Section 3.4.4.5). The fire continues to grow resulting in flames extending 3.1 – 4.6 m (10 – 15 ft) above the rack when the peak fire size is observed at approximately 1:28:50. The fire volume is significantly larger than that observed during the LFP test. Figure 6-6 shows that, unlike the LFP test, all modules in the LNO/LMO rack continue to burn throughout the decay phase as shown at 1:48:50. The flames exiting the rack transition to 'furnace' like flames within the rack and the fire is extinguished with fire hose stream just after 3:40:00.

Figure 6-3: Photos of LFP fire development during large-scale free burn test: near time of ignition (left), near time of predicted sprinkler operation (middle), peak heat release rate (right).

Figure 6-4: Photos of LFP fire during decay phase (left) and at self-extinguishment (right).

1:00:20 1:10:10 1:28:50

Figure 6-5: Photos of LNO/LMO fire development during large-scale free burn test: near time of ignition (left), near time of predicted sprinkler operation (middle), peak heat release rate (right).

1:48:50 3:40:00

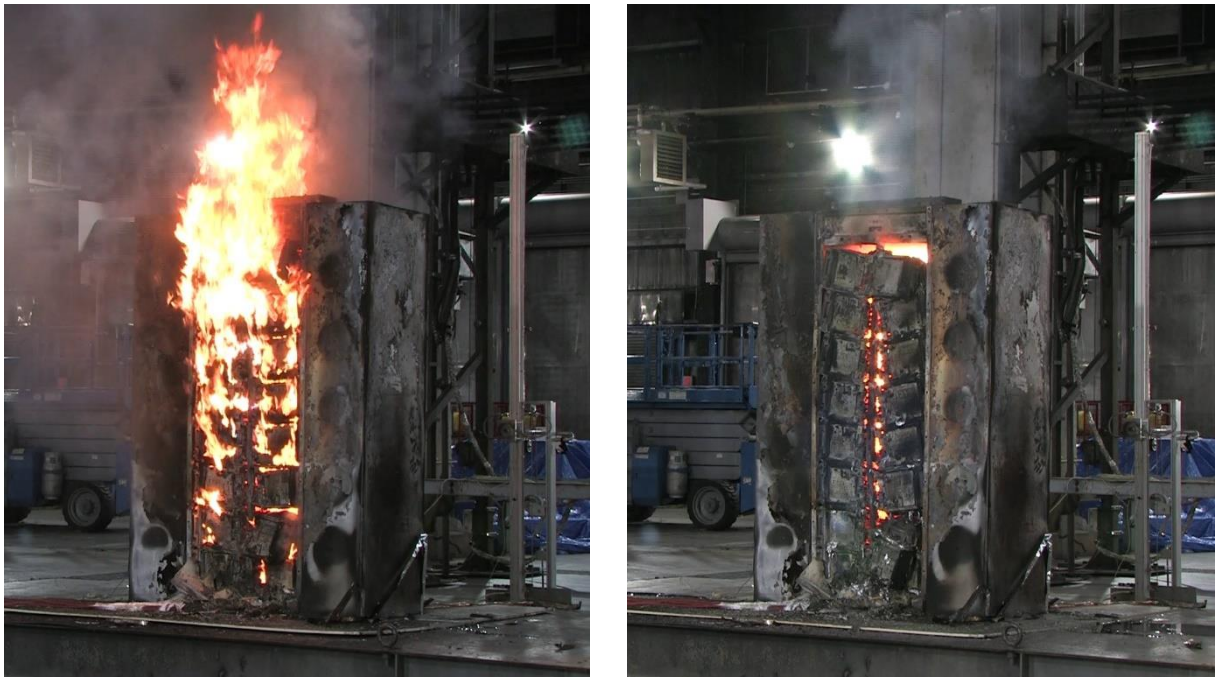

Figure 6-6: Photos of LNO/LMO fire decay phase before firefighter intervention (fire did not self-extinguish). Notice the furnace type combustion evident as the combustion transition to within the rack.

6.1.2.2 TC Measurements

Figures 6-7 and 6-8 show the TC measurements from the modules and racks in the LFP and LNO/LMO tests, respectively. Refer to Figure 6-2 for specific locations of each measurement. For both chemistries, there are two trends that can be attributed to the thermal mass of the modules, which are greater than 45 kg (100 lb) each. Heating of the individual modules is generally delayed until well after flames are initially observed and the modules continue to heat while the fire intensity decreases (as later shown in Figure 6-15). The minimal air gaps between the modules, generally 6.3 mm (0.25 in.), limit radiative heating. Conversely, the smaller mass of the rack walls and larger open spaces around the perimeter of the rack (generally 32 mm [1.25 in.] due to space surrounding the structural members) result in faster increase for many of the TC measurements. This trend is consistent with the modules storing sensible heat, i.e., absorbing heat from the fire, throughout the fire growth, which is then released during the decay phase.

While both chemistries exhibited similar initial heating trends, higher peak temperatures were recorded on both the modules and rack during the LNO/LMO test. The peak LFP module temperatures were nominally in the range of 400°C to 600°C (750°F to 1,100°F) until the fire self-extinguished. Comparable temperatures were recorded for the LNO/LMO modules until a secondary increase began at ~8,000 s as the fire transitioned to 'furnace' type combustion within the rack and the peak temperatures exceeded 1,000°C (1,800°F).

A convenient means of visualizing the fire progression through the modules is the time of exceedance of a threshold temperature. Figure 6-9 presents the time at which each module TC exceeded 66°C (150°F) with reference to module location within the rack. This threshold value was selected as the highest temperature before the noisy portions of the data observed on many channels (Section 3.4.2). Regardless, the resulting heating trends are consistent with test observations. The LFP fire generally progressed upwards to all the modules directly above the ignition module before involving the modules on the other side of the rack. However, collection of hot gases at the top of the rack caused the top two modules to heat up before the modules adjacent to ignition. Conversely, the LNO/LMO fire quickly involved the module to the right of ignition and then progressed upwards on both stacks of modules at the same time.

Similar module heating results were also seen during the intermediate-scale tests with six modules, Figure 6-10. It is interesting to note that the first module to exceed to the temperature threshold during the LFP test was not the ignition module, but rather the module in the middle of the stack above ignition. This was likely related to the mock modules located at the top of the stack for this test heating faster than the much heavier ESS modules, as the ignition module was involved in the fire first. In any case, the fire development was consistent with that in the large-scale LFP test where the modules in the ignition stack were involved in the fire before spreading to the adjacent modules. During the intermediate-scale LNO/LMO test, the fire again quickly jumped to the module to the right of ignition before progressing upwards.

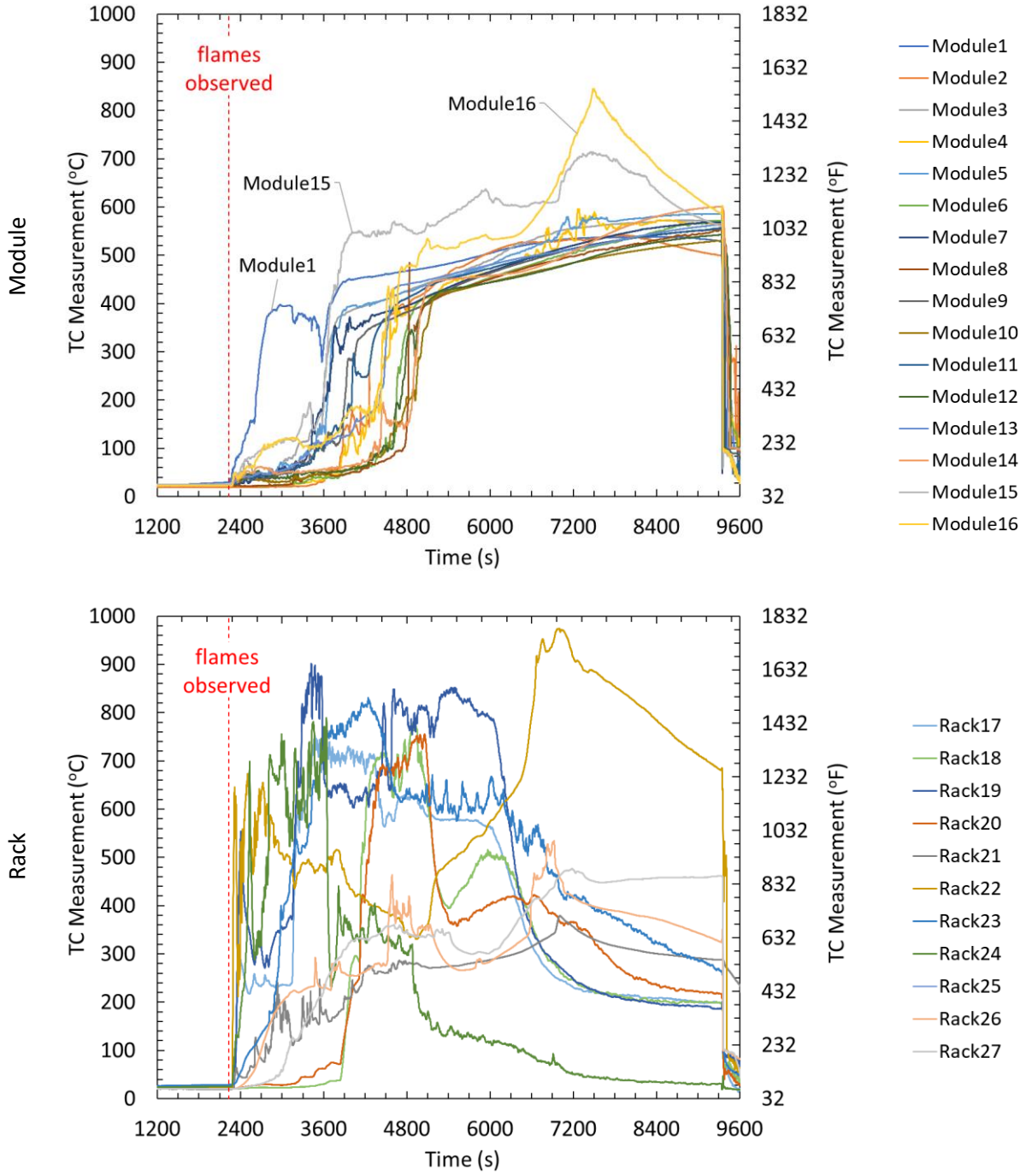

Figure 6-7: TC Measurements on the modules (top) and rack (bottom) during LFP test. Terminated with fire hose at ~9,600 s. Refer to Figure 6-2 for a schematic of each measurement location.

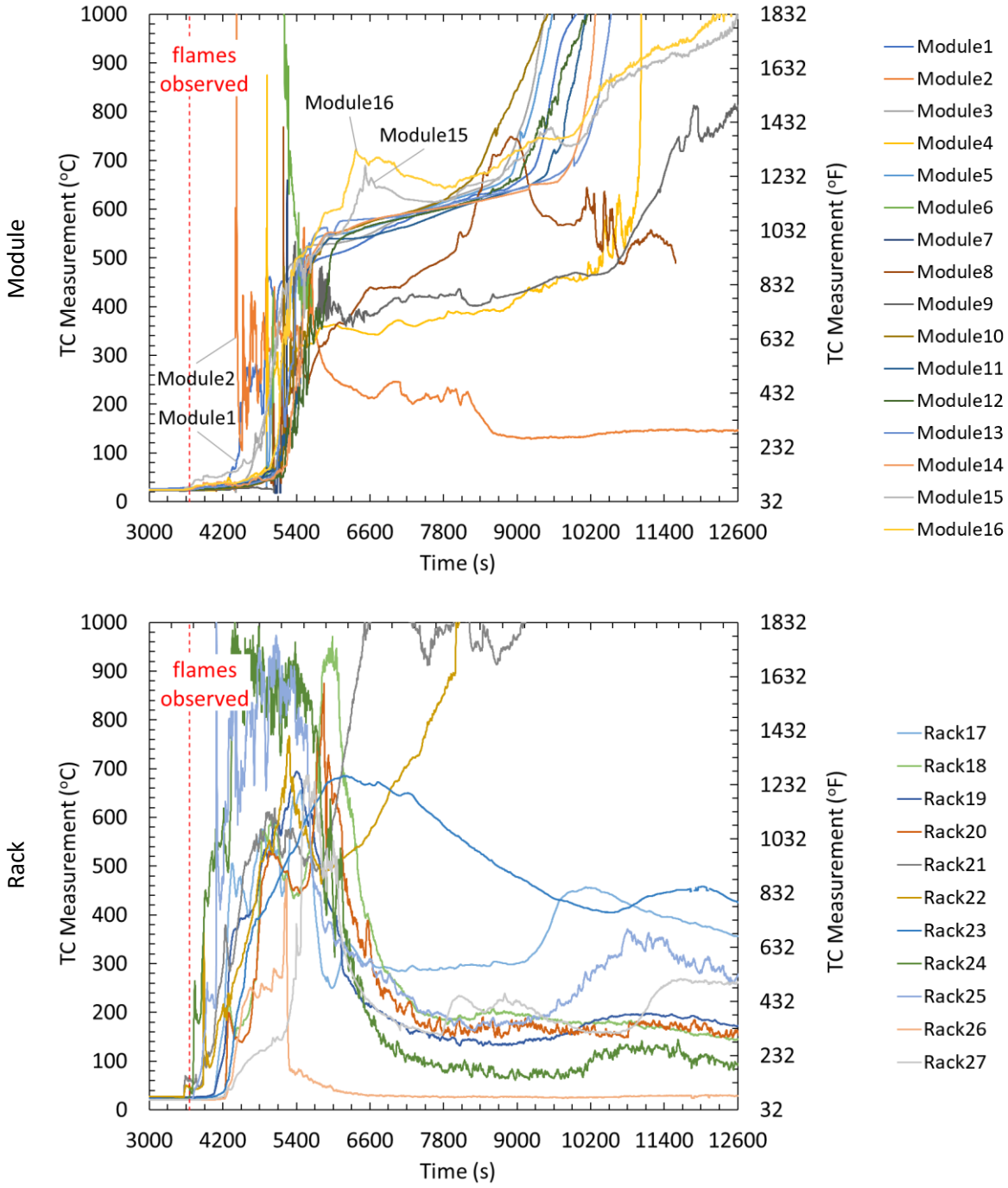

Figure 6-8: TC Measurements on the modules (top) and rack (bottom) during LNO/LMO test. Terminated with fire hose at ~13,500 s (not show). Refer to Figure 6-2 for a schematic of each measurement location.

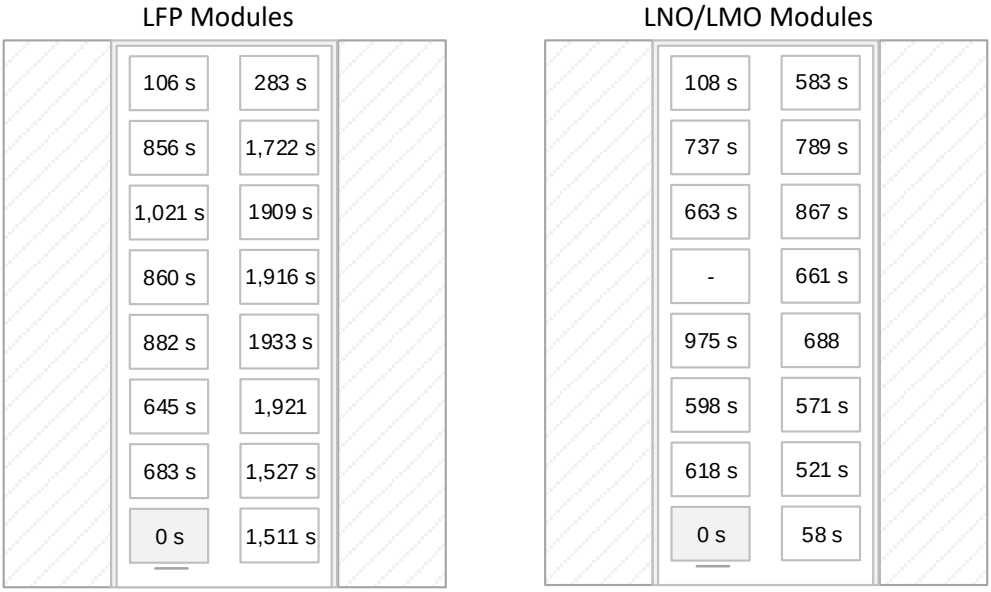

- TC failure before the 66°C (150°F) threshold was reached.

Figure 6-9: Module temperature exceedance time of 150°F (66°C) during large-scale tests. Time shown from first observation of flames on ignition module.

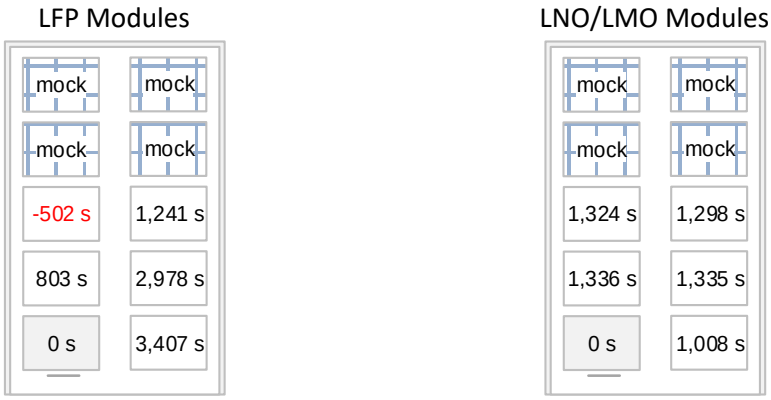

Negative values indicate that the temperature reached the 66°C (150°F) threshold before the ignition module. In all tests, the ignition module was involved in the fire first.

Figure 6-10: Module temperature exceedance time of 150°F (66°C) during intermediate-scale tests. Time shown from first observation of flames on ignition module.

6.1.2.3 Thermal Exposure to Surroundings

Figure 6-11 shows the time-resolved and maximum heat flux to surrounding objects during both tests. As illustrated in Section 6.1.1, all gages were positioned 3.0 m (9 ft) from the closest edge of the ESS rack to measure the near-field heat flux. The only exception was HFG6, which was 11.6 m (38 ft) from the face to measure the far-field heat flux. Good symmetry with regards to the heat flux trends and maximum values was seen for both tests. For example, HFG4, HFG5 and HFG7 are mounted on the opposing structure walls with a similar view of the fire and recorded reasonably similar maximum values with a range of 4 – 7 kW/m^2 (21 – 37 BTU/ft^2/min) for LFP and 15 – 20 kW/m^2 (79 – 110 BTU/ft^2/min) for

LNO/LMO. On the backside of the ESS rack, HFG8 recorded maximum values of 5 and 11 kW/m^2 (26 – 58 BTU/ft^2/min) for the LFP and LNO/LMO, respectively. Shielding from the ESS rack is evident as a reduced heat flux measurement until flames extend approximately 0.3 m (1 ft) above the rack at ~ 2,800 s (46:40) for LFP and 4,260 s (1:11:00) for LNO/LMO.

The data shown here are more extensively used to validate the MPS model presented in Section 7.1, which estimates the near-field heat flux as a function of distance from the fire.

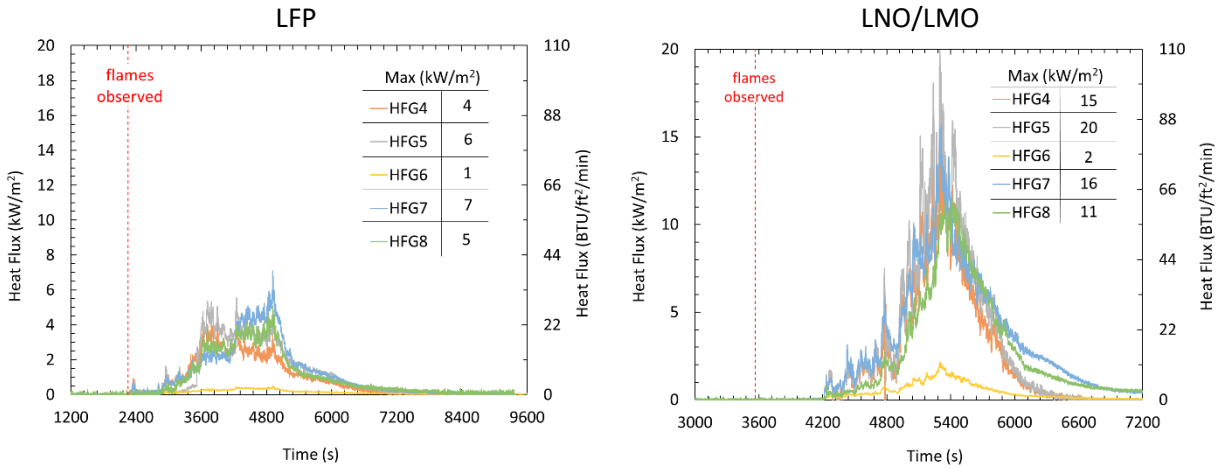

Figure 6-11: Thermal exposure to surroundings during LFP (left) and LNO/LMO (right) test. HFG4-5 & 7-8 were near-field measurements at 2.7 m (9 ft) horizontally from the closest edge of the ESS; HFG6 was a far-field measurement at 11.6 m (38 ft).

6.1.2.4 Thermal Exposure to Adjacent ESS Racks

Figures 6-12 and 6-13 show time-resolved heat flux measurements for the LFP and LNO/LMO tests, respectively. Separate plots are shown for the heat flux measurements collected by the plate thermometers and heat flux gages installed on the mock ESS racks. The faster response of the HFGs results in higher heat flux measurements during the initial growth phase of the fires. Unfortunately, the HFGs all fail early in the test before the peak fire intensity occurs. However, the more robust plate thermometers survive the entire test and report the highest values coinciding with the peak HRR, which is at 4,900 s (1:21:40) for the LFP test and 5,300 s (1:28:20) for the LNO/LMO test. For the purposes of assessing the likelihood of fire spread to adjacent ESS racks, the measurements can be separated into two categories. The faster response of the HFGs provides insight into the heat flux measurements at the expected time of sprinkler operation in the fire (as shown in Section 6.1.2.6). The peak heat flux measured by the PTs represents the most intense heating condition that could be imposed on adjacent battery modules, potentially leading to thermal runaway reactions.

To simplify review of these data, Figure 6-14 overlays the peak instantaneous heat flux values on a schematic of the test array. A similar trend is seen for both chemistries, with values in the range of 80 to 110 kW/m^2 (420 – 580 BTU/ft^2/min) towards the top of the rack and values in the range of 10 to 30 kW/m^2 (53 – 160 BTU/ft^2/min) towards the bottom. However, higher values were generally seen at the mid-rack locations during the LNO/LMO test. It is also noted that the higher values during the LFP test occurred on the side away from ignition, while the opposite was true for the LNO/LMO test.

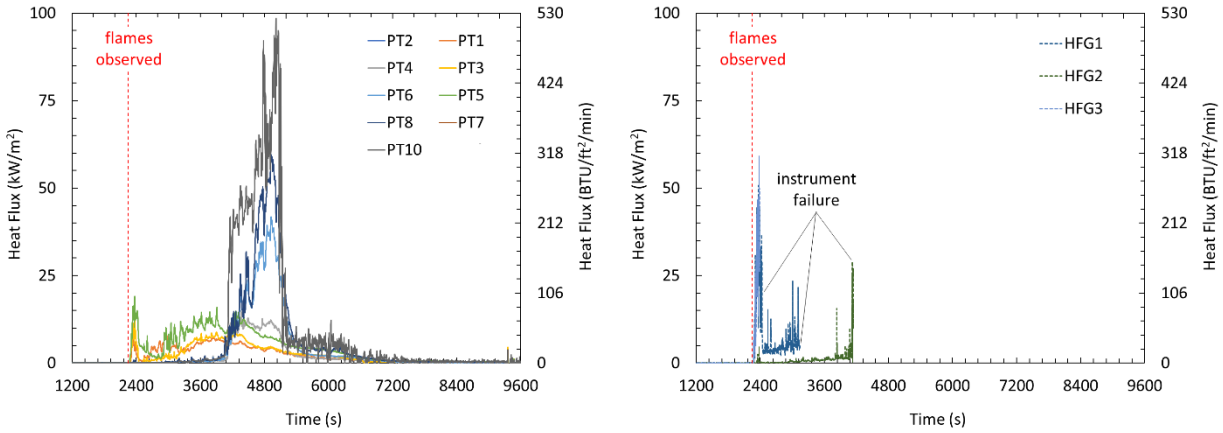

Figure 6-12: Thermal exposure to adjacent ESS racks from plate thermometers (left) and heat flux gages (right) during the LFP test. Note that PT9 failed and is not presented.

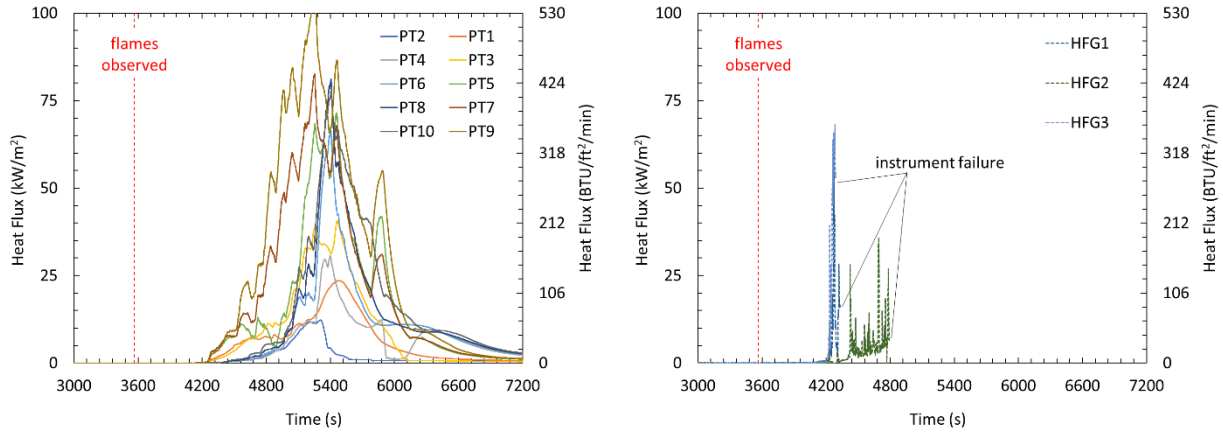

Figure 6-13: Thermal exposure to adjacent ESS racks from plate thermometers (left) and heat flux gages (right) during the LNO/LMO test.

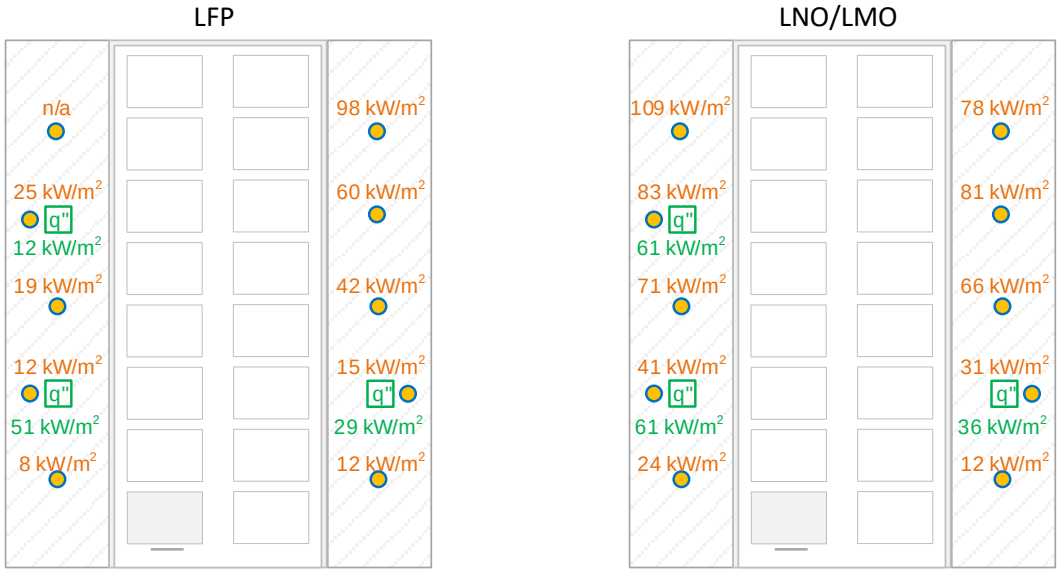

Figure 6-14: Peak instantaneous thermal exposure to adjacent ESS racks from LFP (left) and LNO/LMO (right) tests.

The maximum heat flux values shown Figure 6-14 suggest that the fire would have spread to adjacent ESS racks, i.e., racks installed side-by-side, if they had been present. Following Eq. 3-2, the maximum temperatures imposed on adjacent ESS racks were 860°C (1,575°F) during the LFP test and 900°C (1,650°F) during the LNO/LMO test. Both values are at least triple the 150°C – 200°C (300°F – 400°F) [19, 40, 41] range where thermal runaway reactions generally occur for Li-ion batteries.

6.1.2.5 Heat Release Rate

Consistent with the small- and intermediate-scale tests, the LNO/LMO modules presented a significantly higher fire hazard with respect to energy released during the fire. Figure 6-15 shows the convective and chemical heat release rate measurements based on the collection of the combustion gases in the 20-MW FPC for both LFP and LNO/LMO tests. Also included is the estimated chemical heat release rate based on far-field radiation measurements following the methodology detailed in Section 3.4.4.3.

As shown in Figure 6-15, the peak chemical heat release rate for the LNO/LMO modules of 10,660 kW (10,100 BTU/s) was over a factor of four greater than the 2,540-kW (2,410-BTU/s) peak for the LFP modules. Corresponding convective HRR values were 6,840 kW (6,480 BTU/s) for the LNO/LMO and 1,680 kW (1,590 BTU/s) for the LFP. The LNO/LMO modules released approximately double the total energy during the test. The LNO/LMO module generated 6,390 MJ (6,060 BTU×10^3) of chemical energy, compared to 3,810 MJ (3,610 BTU×10^3) for the LFP module. Total convective energy values were 4,660 MJ (4,420 BTU×10^3) for the LNO/LMO and 2,770 MJ (2,630 BTU×10^3) for the LFP module. These ratios are similar to those from intermediate- and small-scale results.

The chemical HRR estimated from the measured far-field heat flux, following the approach described in Section 3.4.4.3., shows good agreement with the calorimetric measurement. This is an important result allowing direct comparison to the sprinklered fire tests where time-resolved calorimetric measurements are not possible.

The radiative fraction, χ_{rad}, for both tests is shown in Figure 6-16. The convective and chemical HRR based on calorimetric measurement in the FPC exhaust flow are also shown for reference. During the growth phase of the fires the average χ_{rad} is 0.33 to 0.36. To avoid high measurement uncertainty when the convective HRR was less than 1% of the FPC capacity, data were averaged from 2,800 s to 4,900 s (46:40 to 1:21:40) for LFP and 4,200 s to 5,400 s (1:10:00 to 1:30:00) for LNO/LMO. These values are consistent with the small-scale results and further validate the χ_{rad} values used to estimate the chemical HRR from far-field radiation measurements. The subsequent reduction of χ_{rad} to or below zero during the decay phase of the fire, also observed as a merging of the convective and chemical HRR, is consistent with the release of sensible energy stored in the ESS equipment becoming the dominant factor in the heat balance.

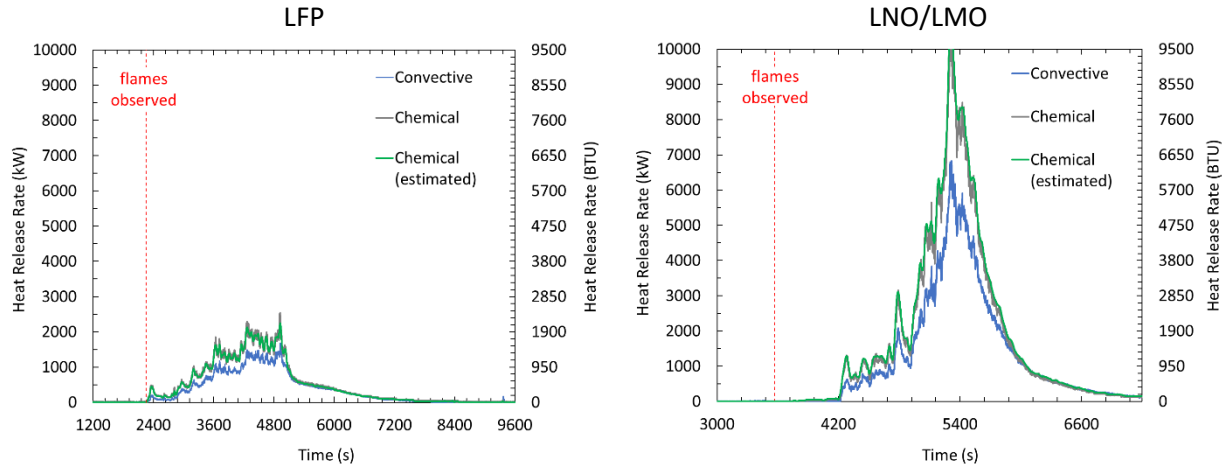

Figure 6-15: Heat release rate for LFP (left) and LNO/LMO (right).

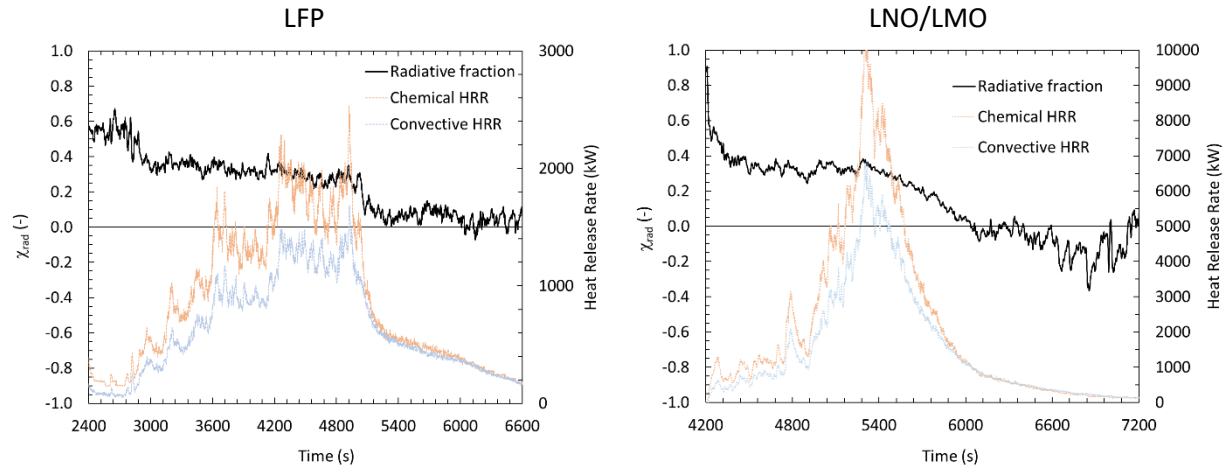

Figure 6-16: Radiant fraction based on convective and chemical heat release rate measurements for the LFP (left) and LNO/LMO (right) tests.

6.1.2.6 Sprinkler Response Prediction

The predicted response of a sprinkler located directly above the fire was calculated following the method described in Section 3.4.4.5. These predictions can be used to evaluate the impact of sprinkler RTI and ceiling height on the time of sprinkler operation and the corresponding fire hazard.

Figure 6-17 presents examples of the predicted response of a QR sprinkler link for the LFP and LNO/LMO tests. In these examples the dashed green lines show the sprinkler response for a 4.6 m (15 ft) ceiling height. Table 6-1 compiles calculations for QR and SR sprinklers for ceiling heights ranging from 4.6 m to 7.6 m (15 ft to 25 ft). For the LFP test, the initial peak HRR was sufficient to operate a QR or SR sprinkler under a 4.6 m (15 ft) ceiling. Raising the ceiling height to 6.1 m or 7.6 m (20 ft or 25 ft) resulted in close to a 600 s delay, while the corresponding HRR was still on the order of 400 kW (380 BTU/s). In comparison the peak convective HRR during this free burn test was 1,670 kW (1,580 BTU/s) showing that the sprinklers would still have operated early in the fire development. Similar results were seen for the LNO/LMO test, except that the operation times exhibited a shorter delay as a function of the ceiling height due to the faster fire growth rate.

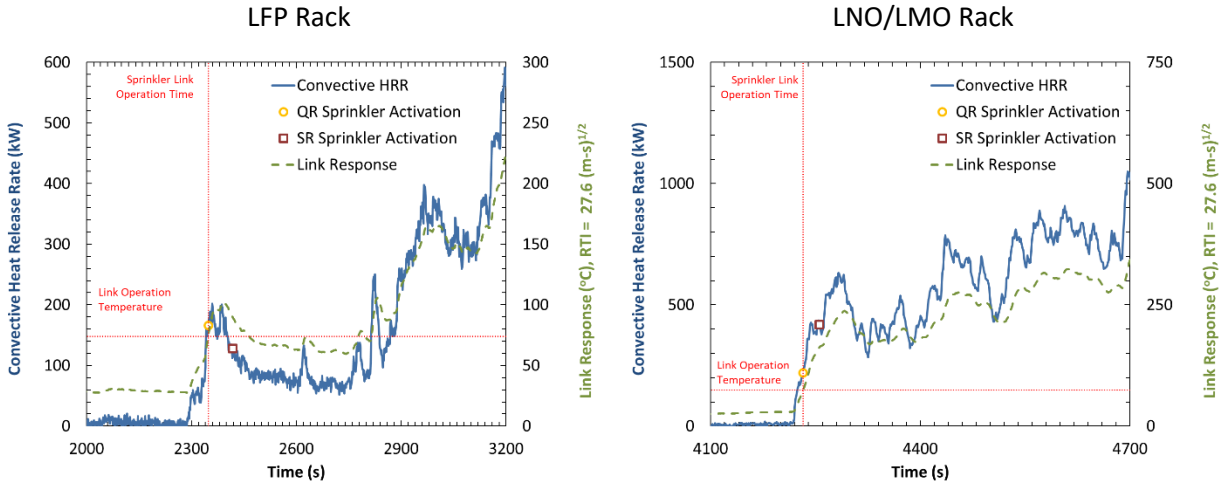

Figure 6-17: Predicted sprinkler response during LFP (left) and LNO/LMO (right) free burn test. Dashed green line shows the response of a QR link installed under a 4.6 m (15 ft) ceiling, directly over the fire.

Table 6-1: Predicted response time and fire heat release rate for ordinary temperature* sprinklers at different ceiling heights. Operation time listed for sprinklers located directly over the fire.

Ceiling Height	QR Sprinklers (RTI = 27.6 $m^{½}s^{½}$ [50 $ft^{½}s^{½}$])		SR Sprinklers (RTI = 170 $m^{½}s^{½}$ [300 $ft^{½}s^{½}$])	
	LFP	LNO/LMO	LFP	LNO/LMO
4.6 m (15 ft)	2,349 s @ 166 kW (157 BTU/s)	4,232 s @ 220 kW (209 BTU/s)	2,419 s @ 128 kW (121 BTU/s)	4,256 s @ 419 kW (397 BTU/s)
6.1 m (20 ft)	2,896 s @ 254 kW (241 BTU/s)	4,241 s @ 358 kW (339 BTU/s)	2,942 s @ 310 kW (294 BTU/s)	4,279 s @ 611 kW (579 BTU/s)
7.6 m (25 ft)	2,961 s @ 369 kW (350 BTU/s)	4,255 s @ 436 kW (413 BTU/s)	3,159 s @ 440 kW (417 BTU/s)	4,347 s @ 417 kW (395 BTU/s)
* Link activation temperature of 165°F (74°C)				

6.2 Sprinklered Fire Tests

Two large-scale sprinklered fire tests were conducted under an unconfined and unobstructed ceiling to represent an ESS installation in a large open area. This approach minimizes the collection of hot gases at the ceiling level needed to operate a sprinkler and allows the test results to be applied to any size room. As shown in Figure 6-18, corner walls were offset 0.9 m (3.0 ft) from the ignition rack to provide heat feedback to the fire and allow for measurement of the thermal exposure to surrounding objects. These walls were 3.7 m (12 ft) tall, resulting in a 0.9 m (3 ft) clearance between the top of the walls and the 4.6-m (15-ft) high ceiling.

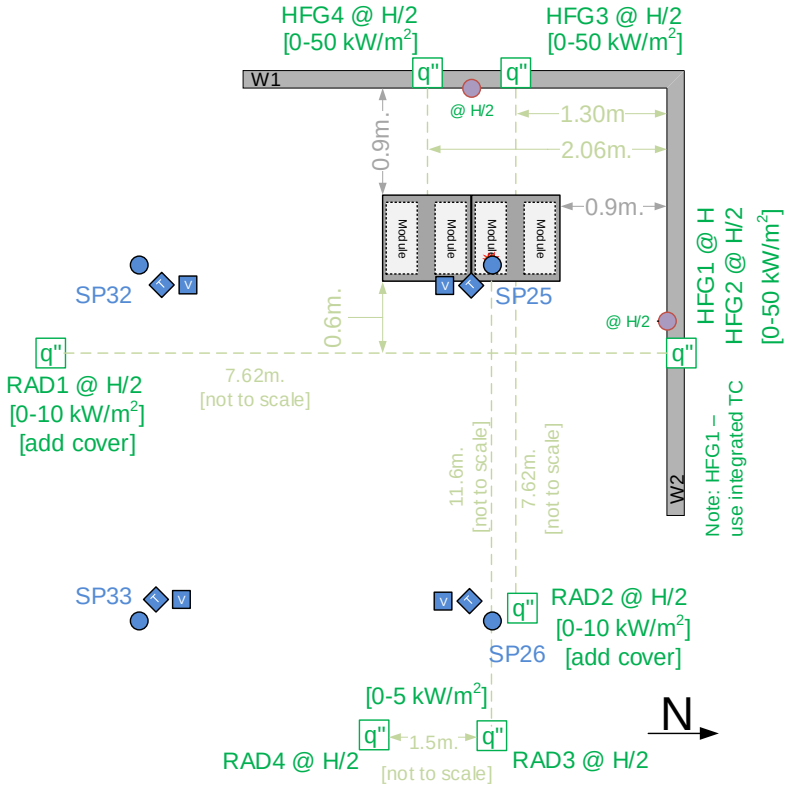

Figure 6-18: Plan view schematic of sprinklered fire test setup and instrumentation layout. The location of heat flux gages and radiometers is shown in green font and the location of active ceiling-level sprinklers and associated instrumentation is shown in blue font. Not shown are the standard 125 TCs and eight bidirectional probes mounted nominally 150-mm (6-in.) below the ceiling.

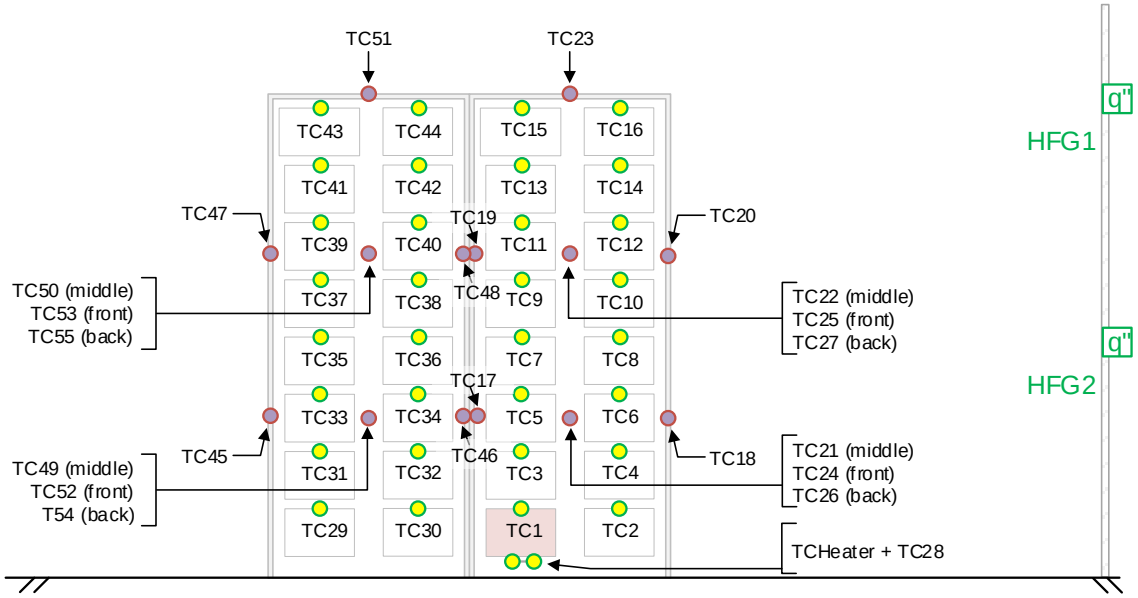

Figure 6-19: Front elevation view schematic of sprinklered fire test and instrumentation layout on the ESS racks. Yellow/green circles indicate TC attached to modules and purple/red circles indicate TCs attached to the ESS rack.

6.2.1 Instrumentation Layout

Sprinklered fire tests were conducted under the north movable ceiling in the Large Burn Laboratory at the FM Global Research Campus. Instrumentation consisted of 56 thermocouples and four heat flux gages and four radiometers located as shown in Figures 6-18 and 6-19. The standard ceiling-level instrumentation to monitor the ceiling gas flow and thermal exposure were also included. In addition, combustion product concentrations were measured in the exhaust gas flow to quantify the total energy released during the test. As discussed in Section 3.4, real-time measurement of the fire was calculated from far-field radiation measurements due to excessive lag and smear associated with gas analysis in this test space.

TCs were installed as follows:

- TC1 – 16 and 29 - 44 were fastened to the top of each module at half the width and depth. TC28 was similarly fastened to the bottom of the ignition module, except offset in between two of the heaters. TCHeater was located between the center and the bottom of the ignition module.
- TC17 – 27 and 45 – 55 were fastened to the ESS rack. Unless otherwise noted, all locations were at half the rack depth.

Heat flux gages and radiometers were installed as follows (see Figure 6-18 for gage range and wall location):

- On the W1 structure wall, HFG3 and HFG4 were located at 1/2 rack height at the horizontal midpoint of each ESS rack. These gages were positioned behind the backside of the ESS racks.
- On the W2 structure wall, HFG1 was located at 1/2 rack height and HFG2 was located at the full rack height. These gages were positioned 0.6 m (2 ft) in front of the ESS rack to improve the view angle of the fire.
- RAD1 was located at 1/2 rack height at 0.3 m (9 ft) from the outer edge of the target ESS rack for the LFP test and 8.5 m (28 ft) for the LNO/LMO test. For both tests, gages were positioned 0.6 m (2 ft) in front of the ESS rack to improve the view angle of the fire.
- RAD3 and RAD4 (LNO/LMO test only) were located 12 m (38 ft) from the face of the ESS, at 1/2 rack height, to provide far-field measurements of the flame radiation.

The following additional instrumentation was installed beneath the movable test ceiling. Schematics of the instrumentation layout can be found in Appendix D.

- Bare-bead, 0.8 mm (20-gage), chromel-alumel thermocouples, placed 165 mm (6 1/2 in.) below the ceiling at 125 locations. These thermocouples have been shown to have an RTI = 8 ± 1 $m^{1/2}s^{1/2}$ (14.5 ± 1.8 $ft^{1/2}s^{1/2}$). Measurements from these thermocouples are referred to as ceiling temperatures.
- Bidirectional velocity probes and associated thermocouples located ~ 180 mm (7 in.) below the ceiling at three radial distances from the ceiling center.
- Four wet pipe sprinklers as shown in Figure 6-18. A thermocouple and bidirectional velocity probe located adjacent to each sprinkler thermal element. In addition, each sprinkler has its operating mechanism included in an electric circuit to determine operation times.

  - Indicator sprinklers (i.e., sprinkler that do not discharge water) were included at the remaining 45 available locations to monitor the potential for additional sprinkler operations.
- Thermocouples imbedded in a cross-shaped steel angle, made from two 51 mm wide × 610 mm long × 6 mm thick (2 in. × 24 in. × 0.25 in.) angle iron segments, attached to the center of the ceiling. Measurements from these thermocouples are referred to as steel temperatures and have been shown to have an equivalent RTI of 1,100 ± 136 $m^{1/2}s^{1/2}$ (2,000 ± 248 $ft^{1/2}s^{1/2}$).
- Flow meters and pressure controllers to monitor and control the sprinkler discharge rate were included.

6.2.2 Sprinkler System Design

Sprinkler protection was provided by K81 L/min/$bar^{1/2}$ (K5.6 gpm/$psi^{1/2}$), QR, nominal 74°C (165°F) temperature rated sprinklers. The sprinklers were installed on 3.0 m × 3.0 m (10 ft × 10 ft) spacing with the sprinkler link located 0.3 m (1 ft) below the ceiling. The sprinkler layout, as later shown in Figure 6-29, is intended to provide the worst-case sprinkler placement with respect to the number of sprinklers that may discharge water onto the fire. Note that moving the ESS equipment such that ignition occurs between-two or among-four sprinklers may result in a slight delay in sprinkler operation, allowing additional fire development, but also increases the likelihood of more than one sprinkler operating during the early stage of the fire development and providing additional cooling.

6.2.3 Results

Both the LFP and LNO/LMO tests showed that ceiling-level sprinkler protection can reduce the overall fire intensity but does not adequately cool the modules within the rack to suppress the fire. This was an expected result because the solid walls of the ESS rack direct the sprinkler water away from the modules causing a deep-seated fire. In addition, sprinkler water discharged directly onto the face of the racks had minimal penetration into the racks due to the tight spacing of the modules. The result was continued thermal runaway reactions within the modules generating ignitable vent gases that burned once out the face of the racks.

Figure 6-20 shows photos of the LFP fire development leading to first sprinkler operation at 1:04:11. The fire continued to grow until it reached peak intensity at 1:44:30. Only one sprinkler operated, located directly over the fire, and the main ESS rack burned out at ~3:12:00. Flames from the fire did not reach the ceiling. As shown in Figure 6-21, the fire was contained to the main ESS rack, though there is some evidence of involvement of the upper two modules in the target ESS rack, adjacent to the main ESS rack. This is consistent with occasional flames being observed during the test in this region. However, no additional involvement of the ESS rack occurred. From a fire protection standpoint, since the fire did not spread beyond the rack of origin, the sprinkler system was able to control but not suppress the fire.

1:04:11

1:44:30

Figure 6-20: Photos of LFP sprinklered test during fire development: first sprinkler operation (left) and peak heat release rate (right).

3:30:00

Post-test

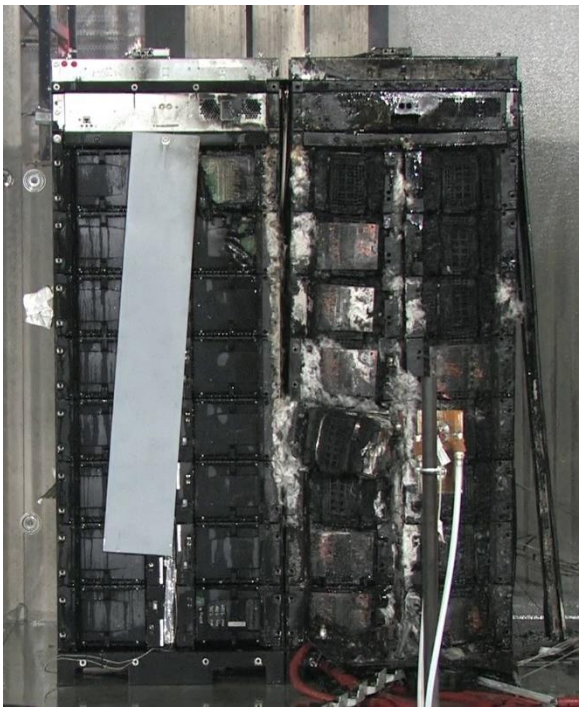

Figure 6-21: Photos of LFP sprinklered test during fire decay phase (left) and at burnout (right).

The increased hazard of the LNO/LMO modules observed in the earlier testing was again evident as a greater fire intensity, and further included fire spread to the target rack in the sprinklered test. Figure 6-22 shows the fire when the first sprinkler operated at 1:35:56, which was located directly over ignition. The subsequent three active sprinklers (i.e., sprinklers charged with water) operated from 1:49:50 to 1:52:45 but did not have any observable impact on the fire. When peak fire intensity occurred at 1:52:29 the flames were impinging on the ceiling and the thermal exposure was sufficient to char the paper on the gypsum board of the structure wall panel. There was also direct flame impingement on the ceiling for several minutes. Flames exiting the main ESS rack suddenly self-extinguished at ~2:01:00, indicating fire burn-out. The sprinkler discharge continued for an additional 30 min to cool the environment. Once the sprinklers were shut off the smoke cleared from the lab and small fires in the target rack were visible, Figure 6-23. The fire grew in intensity, along with a large amount of black smoke, and the sprinklers were turned back on at 3:14:03 once the target ESS rack was fully involved in the fire. Figure 6-24 shows the complete damage to both main and target ESS racks after the test.

This test result strongly suggests that the batteries in the target rack underwent thermal runaway reactions during the initial fire in the main ESS rack. The cooling provided by the active sprinkler system may have slowed the development of the target rack fire but was not sufficient to prevent fire spread. Thus, unlike the LFP case, the sprinkler protection was not able to suppress or control the fire.

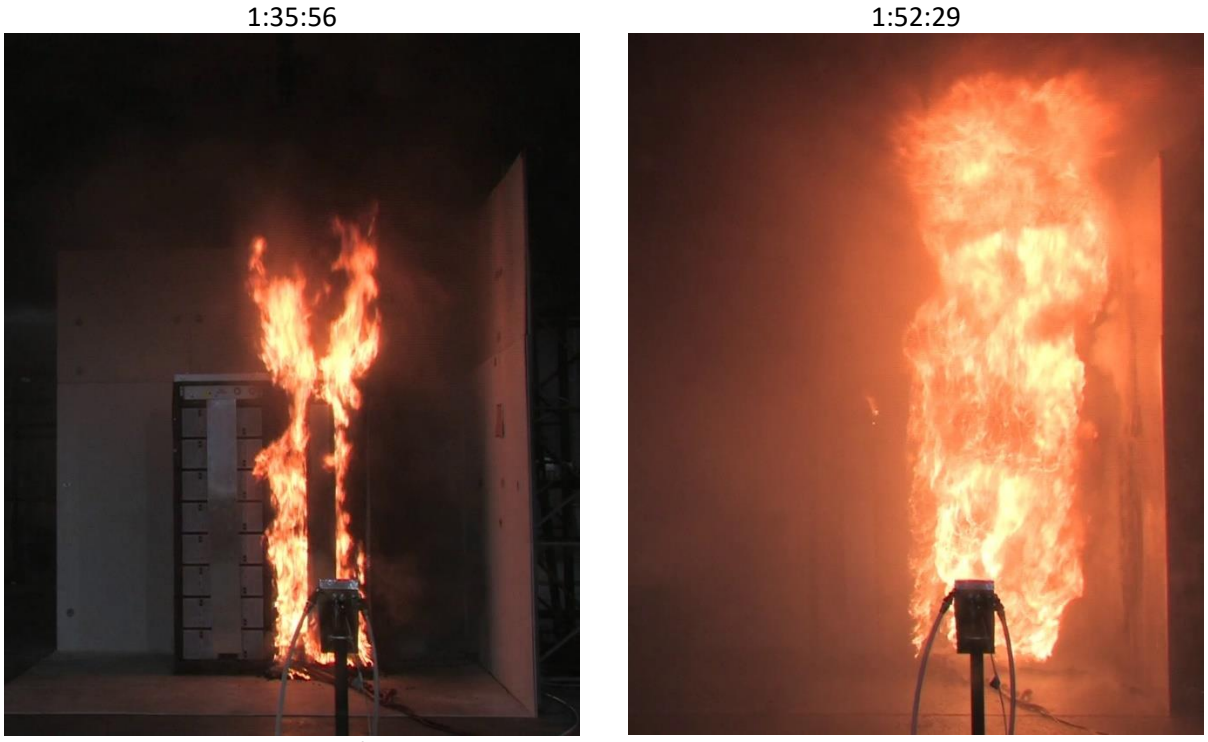

Figure 6-22: Photos of LNO/LMO sprinklered test during fire development on main rack: first sprinkler operation (left) and peak heat release rate (right).

2:35:30 3:14:03

Figure 6-23: Photos of LNO/LMO sprinklered test during fire development on target rack: view of rack once sprinklers were shut off (left) and fire size when sprinklers were turned back on (right).

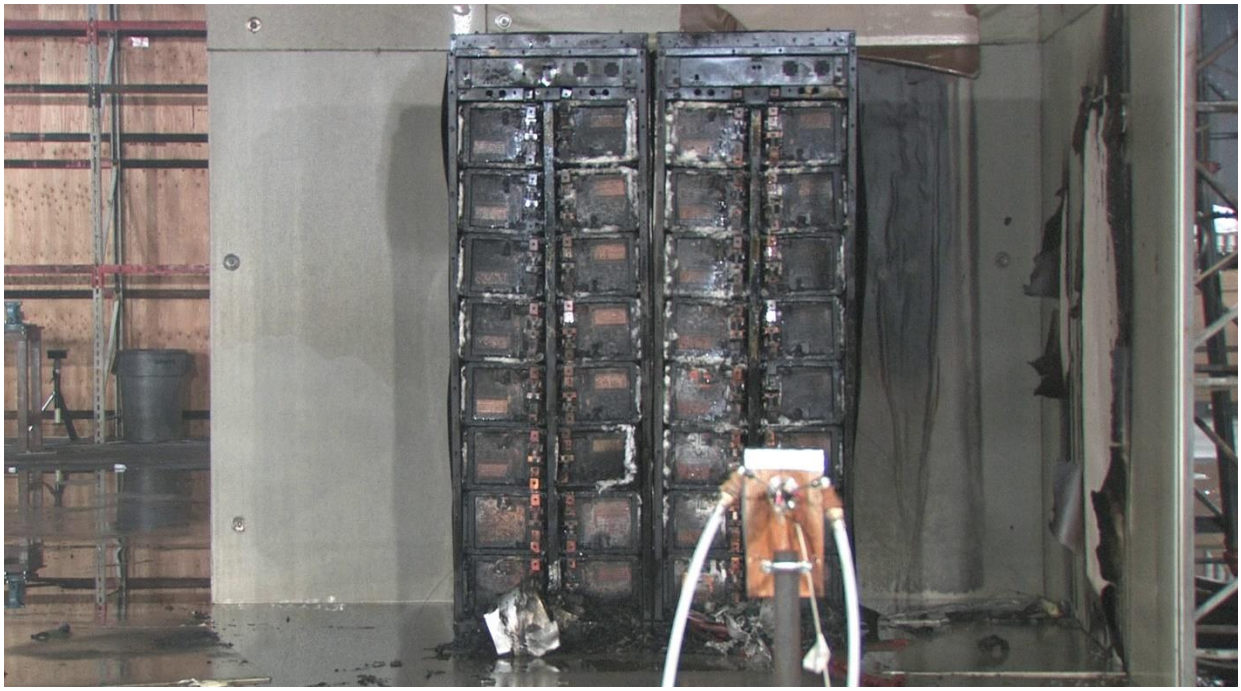

Figure 6-24: Post-test photo of LNO/LMO showing complete burnout of main and target rack.

6.2.3.1 TC Measurements

Figure 6-25 shows the TC measurements from the modules and racks in the LFP tests for both the main and target racks. Similar to the free burn tests, heating of the modules in the main rack was delayed compared to the heating of the rack structure. This was again likely due to the minimal open space and greater thermal inertia of the modules. The rack TCs also recorded higher peak values that in some locations exceeded 900°C (1,650°F), while the modules peaked in the range of 400 to 600°C (750 to 1,110°F). While the fire did not spread to the target rack, the elevated temperature of ESSTC44 (module 44) is consistent with the observed minor contribution to the fire. The elevated temperature of ESSTC29 (Module 29) also indicates some involvement in the fire, though the remainder of the modules did not exceed ~110°C (230°F). The elevated temperatures of 500 to 600°C (930 to 1,110°F) at ESSTC17 / ESSTC19 on the main rack and ESSTC46 / ESSTC48 are on adjacent sides of the rack near the ignition module and suggest sprinkler water was not flowing between the racks.

Figure 6-26 shows corresponding module and rack TC measurements from the LNO/LMO test. The same delayed heating of the modules compared to the rack structure is again evident, as well as peak rack values that in some locations reached 800 – 900°C (1,470 – 1,650°F), while the modules peaked in the range of ~400 – 600°C (750 – 1,100°F). Unlike the LFP test, elevated module temperatures were measured in the target rack while the fire appeared to be contained to the main rack (Module38, 41, 43, 44). While the fire in the target rack occurred after the main rack fire burned out and the sprinklers were shut off, early heating of the target modules is evidence that the target modules were already undergoing thermal runaway reactions.

Unlike the LFP test, the temperatures between the main and target racks (Rack17/19 and Rack46/48) remained low while sprinklers were operating. Since these measurements are on adjacent sides of the racks, water was likely flowing between the racks even though the intersection at the top of the racks was sealed. On the main rack the highest initial temperatures were seen at the face of the main (Rack24/25) and then shifted to the middle (Rack21/22) and back (Rack26) as the fire progressed. A similar progression was seen on the target rack as the fire moved from the face (Rack52/53), to the middle Rack49/50) and back (Rack54/55).

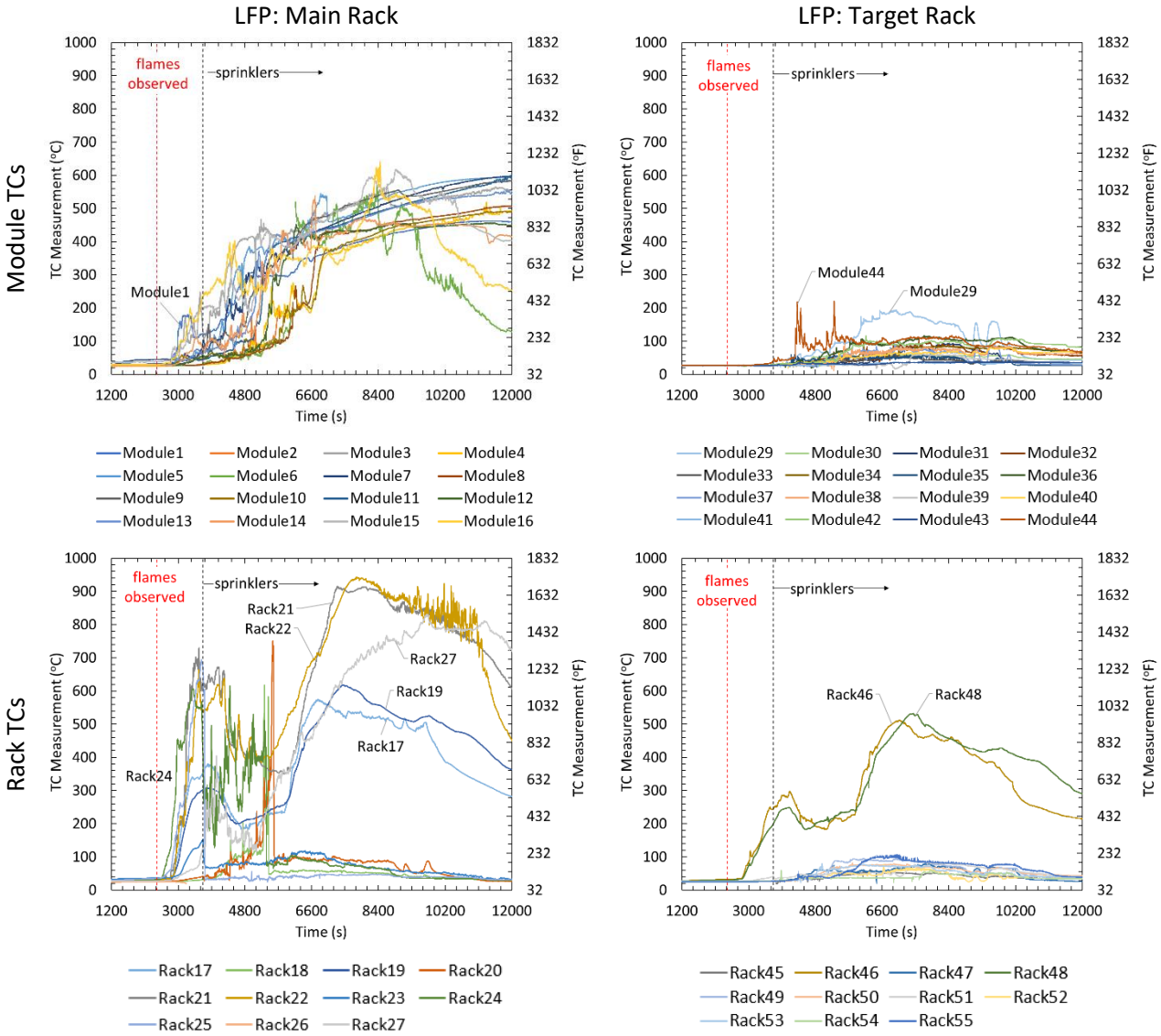

Figure 6-25: TC measurements during LFP test for main (left) and target (right) racks: module temperatures (top), rack temperatures (bottom).

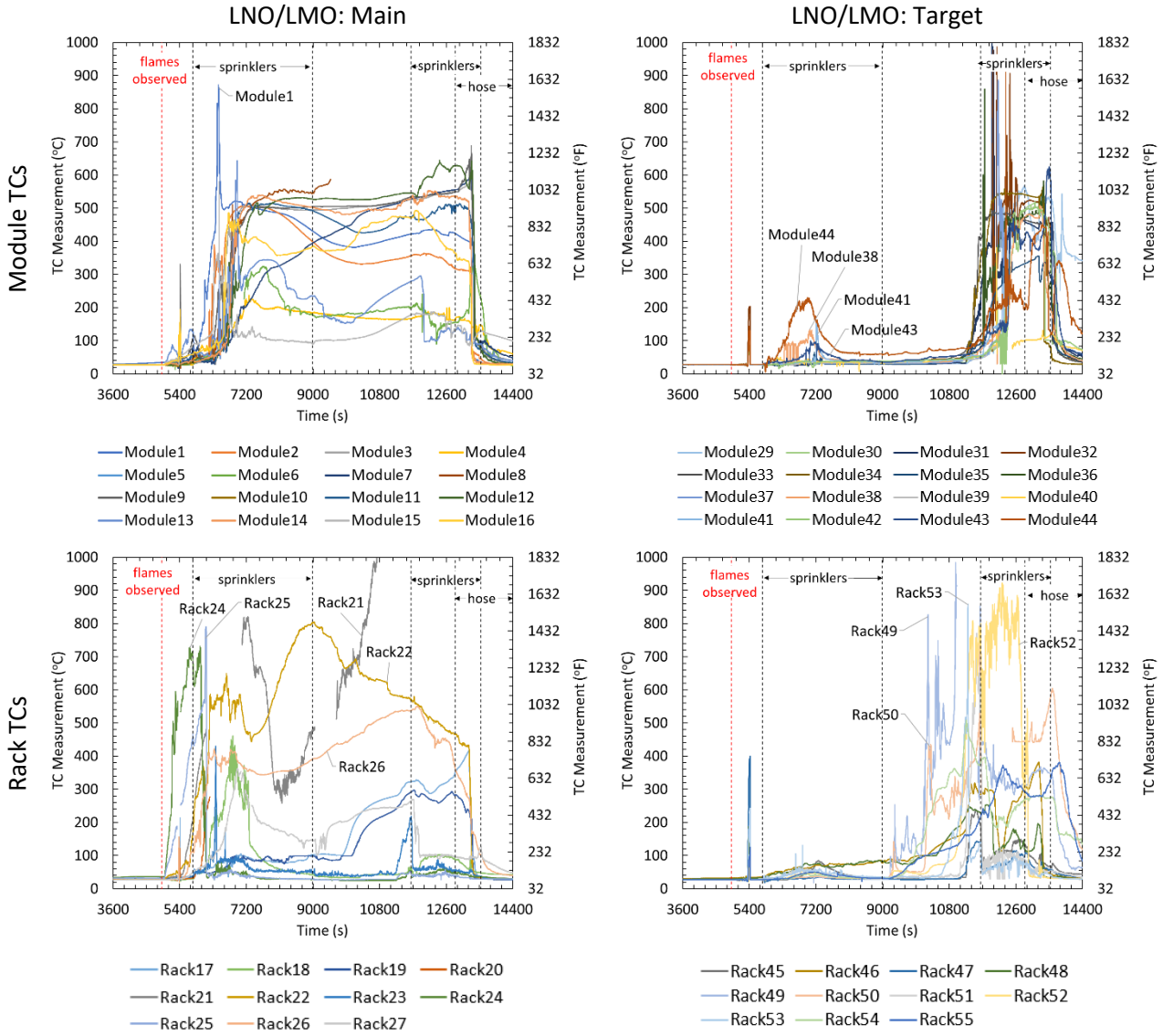

Figure 6-26: TC measurements during LNO/LMO test for main (left) and target (right) racks: module temperatures (top), rack temperatures (bottom).

6.2.3.2 Thermal Exposure to Surroundings

Heat flux measurements were acquired to compare the thermal exposure to the surroundings for both tests. Time-resolved data are shown in Figure 6-27 and corresponding heat flux values at the time of the first sprinkler operation and at the peak intensity are listed in Table 6-2. While similar trends were observed, the magnitudes were significantly higher during the LNO/LMO test. Beyond the comparisons presented here, these data validate the MPS model used to calculate the change in thermal exposure with respect to the distances detailed in Section 7.1.

At first sprinkler operation, the heat flux at 0.9 m (3 ft) away from the racks, i.e., HFG1-4, ranged from 0.5 to 4.6 kW/m^2 (2.6 to 24.3 BTU/ft^2/min) for the LFP test and 0.1 to 1.6 kW/m^2 (0.53 to 8.5 BTU/ft^2/min) for the LNO/LMO test. The sudden drop to negative values after sprinklers operated was due to water flow along the corner walls wetting the gages. The negative values are caused by the

sprinkler water temperature of 29°C (85°F) being lower than the target gage temperature of 43°C (110°F). A supplemental test where a gage was submerged in a bucket of sprinkler water showed the maximum decrease due to wetting was -6 kW/m^2, under the conditions of these tests. RAD1-2 were also wetted during the LFP test, though a cover was added above these gages before the LNO/LMO test to mitigate wetting.

After sprinkler operation, far-field heat flux measurements provided the most reliable means of measuring the fire intensity. RAD3-4 were located 11.6 m (38 ft) away from the face of the racks and were not subject to any wetting from the sprinklers. The low peak values of 0.3 kW/m^2 (1.6 BTU/ft^2/min) for the LFP test and 1.4 to 1.6 kW/m^2 (7.4 to 8.5 BTU/ft^2/min) for the LNO/LMO test were due to the distance from the fire, but the time-resolved data showed consistent trends with the near-field gages.

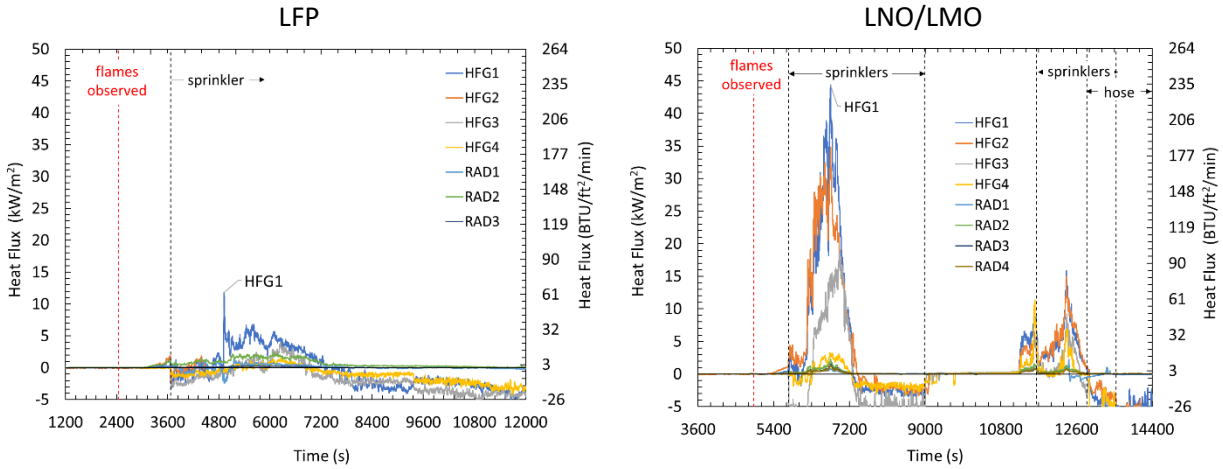

Figure 6-27: Thermal exposure to surrounding objects during LFP (left) LNO/LMO (right) during test.

Table 6-2: Heat flux values at peak intensity and at first sprinkler operation for LFP and LNO/LMO tests.

Gage		LFP		LNO/LMO	
Location	Distance*	@ Sprinkler†	Peak	@ Sprinkler†	Peak
(-)	m (ft)	kW/m^2 (BTU/ft^2/min)		kW/m^2 (BTU/ft^2/min)	
HFG1	0.3 m (3 ft)	1.5 (7.9)	12 (63)	1.3 (6.9)	44 (232)
HFG2		1.9 (10)	3.8 (20)	1.6 (8.5)	35 (180)
HFG3		0.1 (0.5)	4.0 (21)	0.1 (0.5)	19 (100)
HFG4		0 (0)	1.5 (7.9)	0.1 (0.5)	11 (58)
RAD1	3 m (9 ft): LFP	0.3 (1.6)	1.3 (6.9)	0.1 (0.5)	2.3 (12)
RAD2	8.5 m (28 ft): LNO/LMO	1.2 (6.3)	2.3 (12)	0.2 (1.1)	2.3 (12)
RAD3	11.6 m (38 ft)	0.1 (0.5)	0.3 (1.6)	0.1 (0.5)	1.6 (8.5)
RAD4‡		-	-	0.1 (0.5)	1.4 (7.4)

* Measured from closest edge of the test structure.
† Sprinkler operation occurred at 3,667 s during the LFP test and at 5,756 s during the LNO/LMO test.
‡ RAD4 not present during LFP test.

6.2.3.3 Heat Release Rate Estimates

With the addition of sprinkler protection, the LNO/LMO modules still presented a significantly higher fire hazard as observed in all free burn tests. Heat release rate estimates based on the far-field radiation measurements, as described in Section 3.4.4.3, are shown in Figure 6-28. The peak heat release rate during the LNO/LMO test was 6,690 kW (6,340 BTU/s) for the main rack and 4,900 kW (4,600 BTU/s) for the target rack, which were around three times greater than the 1,880 kW (1,780 BTU/s) peak for the LFP modules (in the latter case, the fire did not spread to the target rack). The corresponding total energy released during the LNO/LMO test was 4,360 MJ (4,130 BTU×10^3) for the main rack and 4,510 MJ (4,270 BTU×10^3) for the target rack. The total energy released was also slightly lower for the LFP with a value of 3,440 MJ (3,260 BTU×10^3).

It is interesting to note the temporary reduction in the HRR when sprinkler water was discharged onto the LNO/LMO fire. When the first sprinkler operated due to the growing fire on the main ESS rack, at 5,756 s (1:35:56), there was a 300 s (5:00) plateau in the HRR before the fire began to increase rapidly. A more dramatic event occurred during the target ESS rack fire. In this case, water was manually re-supplied to all four sprinklers (similar to a deluge system because all sprinklers had already operated) at 11,643 s (3:14:03) and the fire size dropped from ~5,000 to ~1,000 kW (4,700 to 950 BTU/s) before increasing rapidly. A similar trend was seen in the LFP test, where a temporary plateau in the HRR occurred following sprinkler operation.

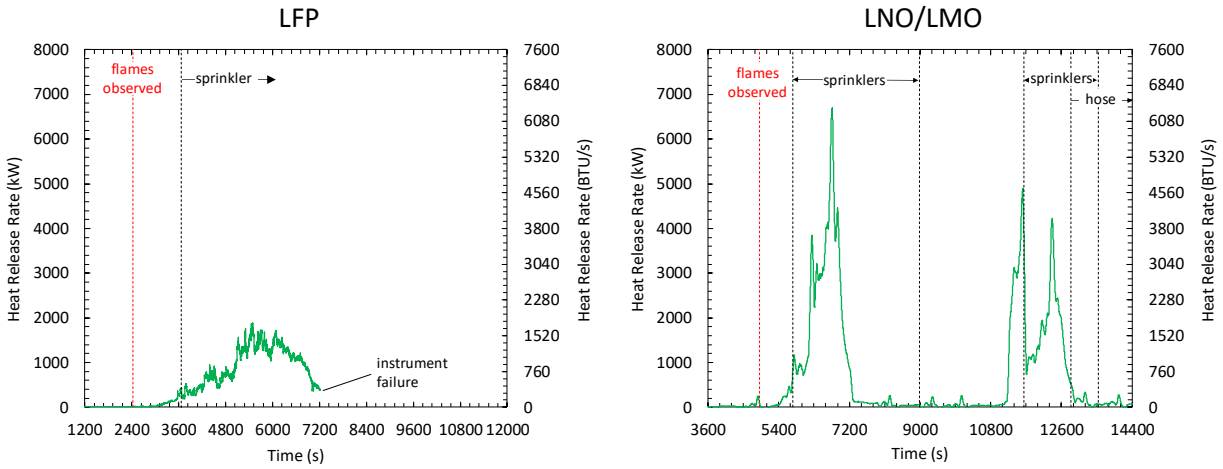

Figure 6-28: HRR for LFP (left) and LNO/LMO (right) based on far-field radiation measurements in the sprinklered test environment.

6.2.3.4 Sprinkler Performance

Figure 6-29 illustrates the sprinkler operation pattern during the LFP and LNO/LMO tests. Sprinklers that operated are shown as solid circles. The four blue circles represent the location of active sprinklers that could discharge water upon operation. The remaining 45 locations represent potentially installed sprinklers, shown as orange circles, to provide a conservative estimate on the maximum potential water demand.

During the LFP test a single sprinkler operated at 3,667 s (1:01:07) after ignition, directly over ignition, and contained the fire to the main rack. The larger fire during the LNO/LMO test resulted in the

operation of all four active sprinklers, with the first occurring at 5,756 s (1:35:56) followed by the remaining three from 6,274 to 6,449 s (1:44:34 to 1:47:29). Thirty-five indicator sprinklers operated from 6,245 to 6,764 s (1:44:05 to 1:52:44), including many operations along the perimeter of the ceiling. These results suggest that in an unconfined environment, i.e., where nearby walls do not contribute to the build-up of the hot ceiling gas layer, the typical 230 m^2 (2,500 ft^2) demand area would have been sufficient for the LFP rack but may have been exceeded for the LNO/LMO rack. Further analysis is necessary to evaluate the demand area for smaller room sizes, where the build-up of the ceiling-gas layer does occur. However, a conservative estimate is to assume all sprinklers would operate when the room area is equivalent to the sprinkler demand area.

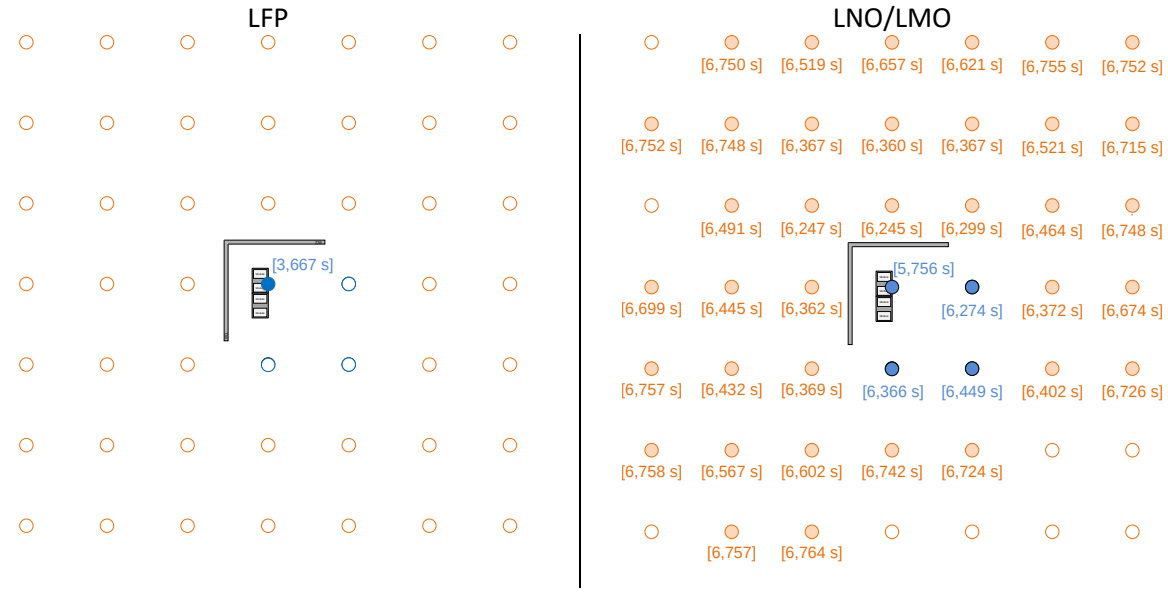

Figure 6-29: Sprinkler operation overview for LFP (left) and LNO/LMO (right) tests. Sprinklers that operated are shown as solid circles. Blue circles represent active sprinklers that could discharge water and orange circles represent indicator sprinklers that could not.

The ceiling TC measurement contours at first sprinkler operation are shown in Figure 6-30. For both tests, the alignment of the centroid with the ignition location indicates the fire plume was centered. This confirms that the test design choice, where the corner walls did not extend up to the ceiling, avoided build-up of the ceiling gas layer that could have expedited the initial sprinkler operations.

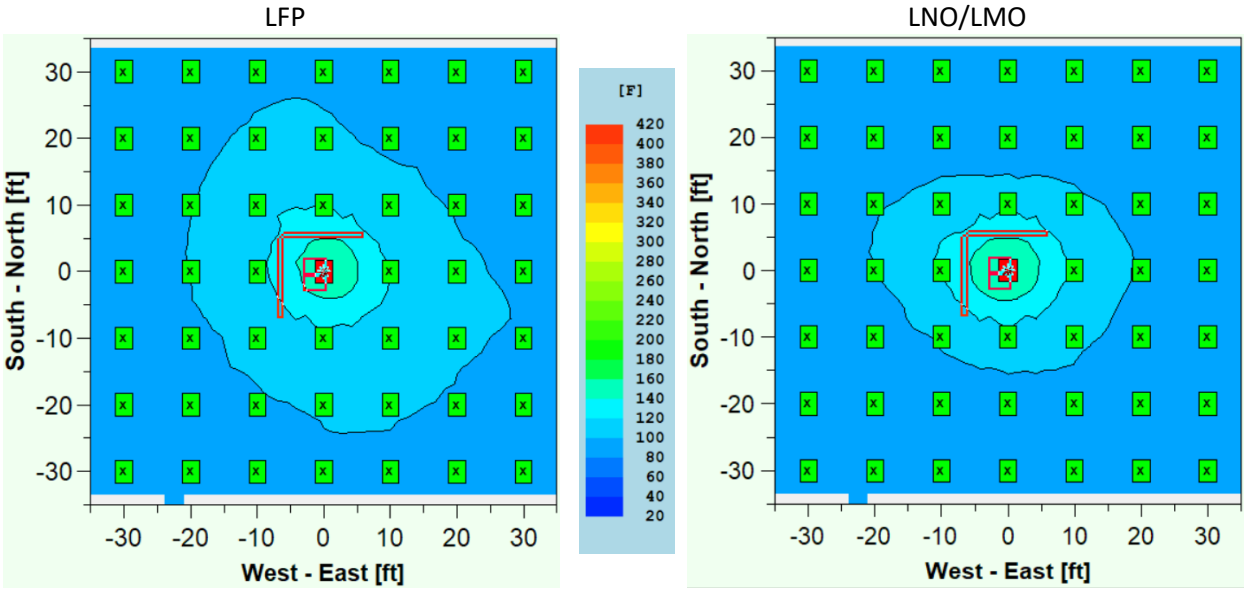

Figure 6-30: Contour plots of ceiling gas temperatures at first sprinkler operation during LFP (left) and LNO/LMO (right) tests. Convert to metric as [m = ft × 0.305] and [°C = (°F – 32)/1.8)].

Figure 6-31 shows the steel TC measurements and adjacent ceiling TC measurement. The maximum average steel TC measurement was 83°C (181°F) during the LFP test and 425°C (797°F) during the LNO/LMO test. These values represent the average of all nine steel TCs and are below the 538°C (1,000°F) threshold where damage to the ceiling could occur. While not shown, one of the individual steel-TCs reached 590°C (1,094°F) during the LNO/LMO test, indicating there is some potential for damage to the ceiling. The maximum for the other eight steel TCs ranged from 284°C to 515°C (543°F to 959°F).

The adjacent ceiling TC measurement, located above ignition, was 272°C (522°F) for the LFP test and 747°C (1,377°F) the LNO/LMO test. These values are consistent with the observation of flames impinging on the ceiling during the LNO/LMO test but not during the LFP test.

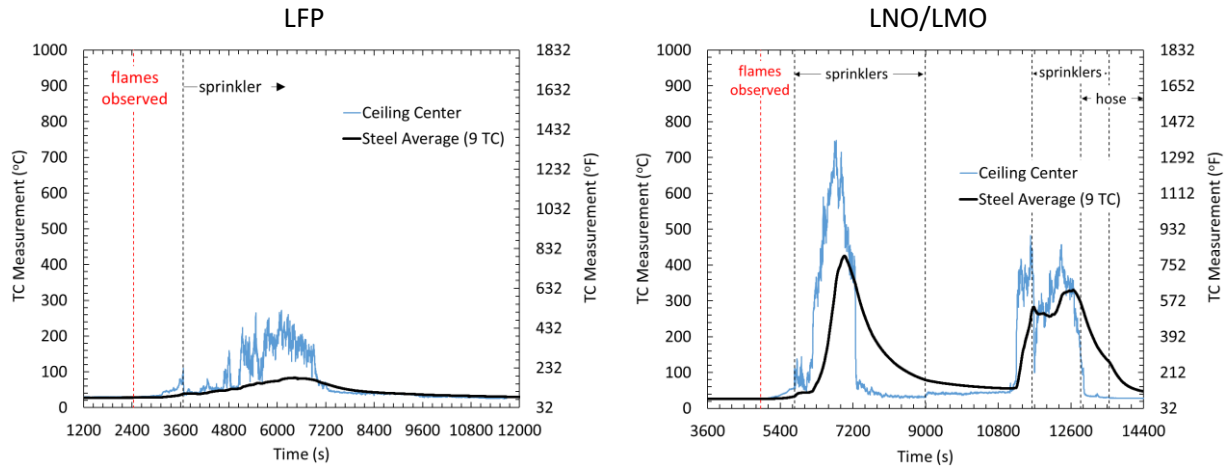

Figure 6-31: Ceiling steel TC measurements and gas temperature at the ceiling center during LFP (left) and LNO/LMO (right) test.

The sprinkler discharge pressures, shown as a 10-s average in Figure 6-32, were controlled within 10% of the target value which meets the acceptance criteria for the lab. The sudden drop in pressure during the LNO/LMO test at ~9,000 s (2:30:00) was due to the sprinkler system being shut off to clear smoke from the lab after the fire in the main rack burned out.

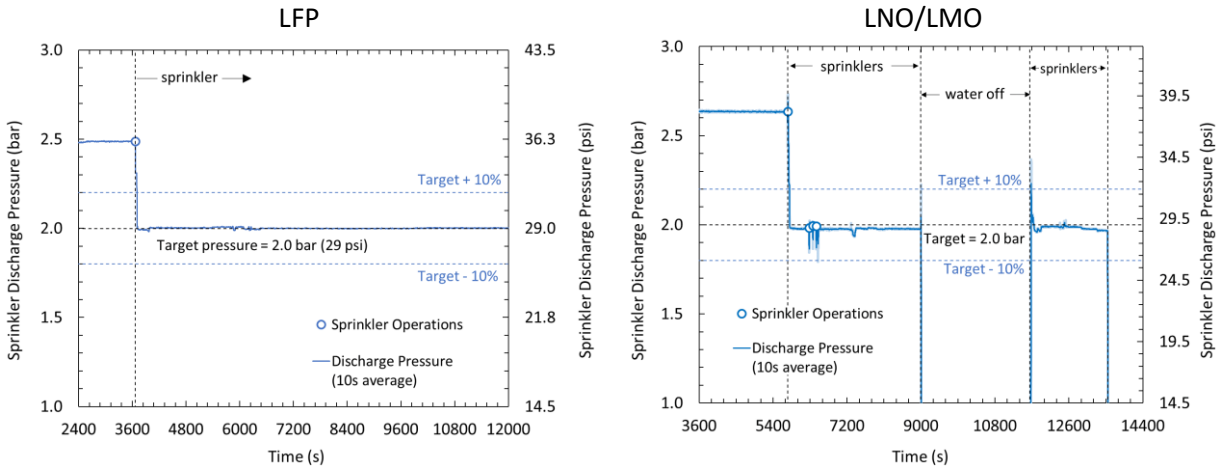

Figure 6-32: Sprinkler discharge pressure during LFP (left) and LNO/LMO (right) tests.

7. Application of Test Results to Sprinkler Protection Guidance

Through large-scale fire testing, sprinkler protection available at many non-storage commercial facilities has been shown to reduce the hazard of an ESS fire. While the design of the racks effectively shields the fire from sprinkler water, under the conditions of the tests, the sprinklers delayed or outright prevented fire spread to adjacent racks. Coupled with adequate space separation from nearby combustibles and the addition of thermal barriers between racks, the hazard can be further decreased. However, lacking a protection system that can suppress the fire in the early stages, prolonged fire duration, high water demand, and damage to the surroundings is likely. This section discusses the differences in the observed hazard between the tested LFP and LNO/LMO based systems leading to the application of the test results to protection and installation guidance.

7.1 Evaluation of Sprinkler Protection

To assess the value of sprinkler protection it is first important to define reasonable expectations for performance. The intention of this testing was to evaluate the performance of a sprinkler system designed to provide a 12 mm/min (0.3 gpm/ft^2) discharge density. No specific pass / fail criteria were set to evaluate the adequacy of the protection. Rather, the overall hazard of an ESS fire in a commercial occupancy was assessed based on: 1) the reduction in the fire intensity based on the peak HRR, 2) the potential for damage to surroundings, and 3) fire containment to the ESS rack of origin. Protection guidance coupling sprinkler system design and ESS installation guidance is then provided to manage the hazard within acceptable levels.

7.1.1 Hazard Reduction

Chemical heat release rate is a convenient means of measuring the hazard of an unprotected fire and the subsequent reduction achieved with sprinkler protection. Figure 7-1 presents a comparison of the chemical HRR from the large-scale free burn and sprinklered fire tests. HRR is calculated from far-field heat flux measurements as described in Section 3.4.4.3, which allows for direct comparison between the tests. Here it can be seen that modest reductions in the fire intensity were gained with the sprinkler protection used in this project. The peak HRR for the LFP rack reduced from 2,240 kW to 1,225 kW (2,120 to 1,160 BTU/s) representing a difference of 45%, and peak values for the LNO/LMO rack reduced from 10,120 kW to 6,690 KW (9,600 to 6,340 BTU/s) for a difference of 34%. The results from both chemistries indicate that sprinkler protection alone is not sufficient to address an ESS fire.

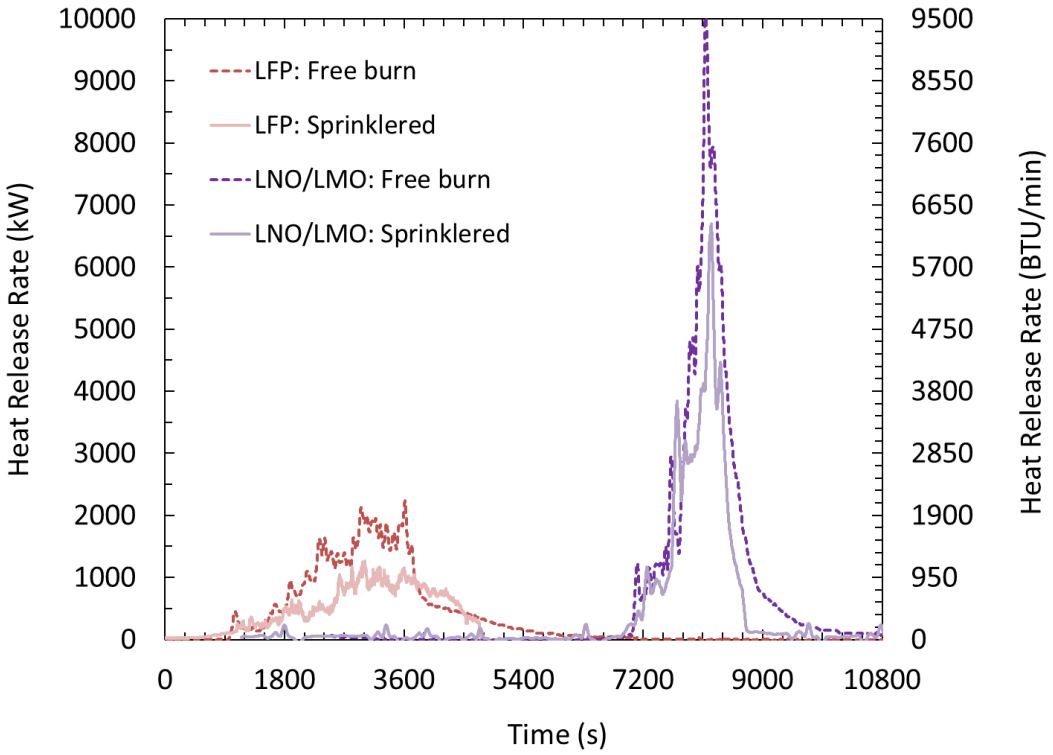

Figure 7-1: Comparison of heat release rate during free burn and sprinklered tests. Times are offset to group LFP and LNO/LMO data.

7.1.2 Space Separation and ESS Installation Considerations

One means of managing the hazard is adequate space separation to prevent fire spread to nearby combustibles, including adjacent ESS racks, or damage to non-combustibles. Two prominent public documents provide guidance on separation distance: FM Global Property Loss Prevention Data Sheet 1-20 (DS 1-20), *Protection Against Exterior Fire Exposure* [42], and National Fire Protection Association Standard 80A (NFPA 80A), *Recommended Practice for Protection of Buildings from Exterior Fire Exposures* [43]. The recommended separation distances in both documents are based on limiting the maximum instantaneous heat flux to exposed combustibles to ≤ 12.5 kW/m^2 (66 BTU/ft^2/min). This value is considered representative of the critical heat flux for piloted ignition of plastic and cellulosic materials. DS 1-20 also provides recommendations for non-combustible objects based on a maximum imposed heat flux of 27 kW/m^2 (140 BTU/ft^2/min), which is considered representative of the damage threshold for metal and glass objects.

Figure 7-2 presents the thermal exposure to the surroundings from the large-scale LFP and LNO/LMO tests as a function of distance. All heat flux estimates represent 60-s average values and were calculated using the MPS model from far-field heat flux measurements and validated with near-field heat flux measurements as described in Section 3.4.4.4. Threshold values for combustibles and non-combustibles are provided as dashed lines. These data show that the LFP system can be safely separated by 0.9 m (3 ft) from non-combustible objects and 1.5 m (5 ft) from combustibles when sprinkler protection is present. Those distances increase to 1.2 m (4 ft) and 1.8 m (6 ft), respectively, when sprinkler protection is not present. The higher hazard of the LNO/LMO system results in increased separation distances of

1.8 m (6 ft) from non-combustibles and 2.7 m (9 ft) from combustibles when sprinkler protection is present. Without sprinkler protection, the recommended separation distances for LNO/LMO further increase to 2.4 m (8 ft) and 4.0 m (13 ft), respectively. Note that this evaluation conservatively omits any potential surface cooling provided by the sprinklers, i.e., water running down the exposed surfaces.

Similar calculations based on the peak 60-s average heat flux measurements during the intermediate-scale tests, detailed in Section 5, result in separation distances for the LFP system of 0.9 m (3 ft) from non-combustible objects and less than 1.2 m (4 ft) from combustibles when sprinkler protection is not present. Comparable separation distances for the LNO/LMO system are 1.2 m (4 ft) from non-combustibles and 1.8 m (6 ft) from combustibles. These results are in general agreement with the large-scale data, where the higher peak HRR from the LNO/LMO system lead to greater separation distance requirements.

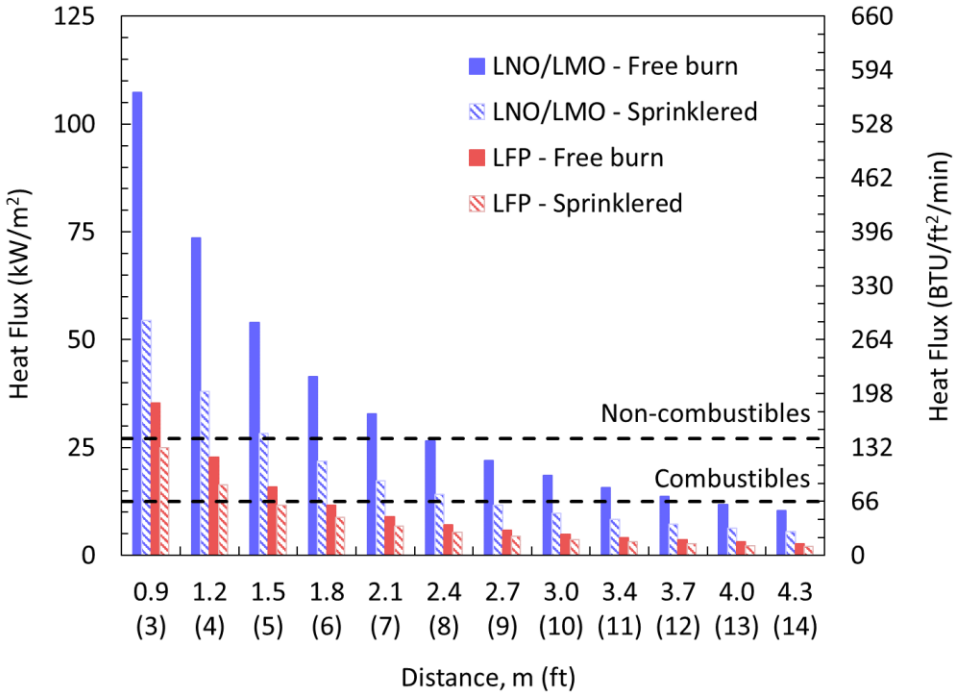

Figure 7-2: Predicted thermal exposure to combustible and non-combustible objects as a function of distance. Results are based on large-scale testing of an 83 kWh LFP system and 125 kWh LNO/LMO system.

For indoor installations it is also important to consider possible damage to the ceiling from flame impingement or the collection of fire plume gases. As shown in Section 6.2.3.4, flames directly impinging on the test ceiling during the LNO/LMO resulted in temperatures that were near or above the threshold value for damage to a 4.6 m (15 ft) high ceiling. Following the methodology detailed in Section 3.4.4.5, raising the ceiling to approximately 7.6 m (25 ft) would prevent damage to an unprotected ceiling in an

unconfined environment[iii]. While outside the scope of this project, further analysis is needed to determine the corresponding ceiling height for smaller rooms where the collection of fire plume gases could result in the need for higher ceilings. However, to limit the potential for damage, ceilings in the range of 3.0 m (10 ft) to 7.6 m (25 ft) heights should have a 1-hour fire rating in accordance with documents such as DS 1-20 or National Fire Protection Association Code 5000, *Building Construction and Safety Code* [44]. Additionally, the impact of thermal barriers, such as fire rated barriers or spray-on foams, could also reduce the damage potential.

The addition of thermal barriers between adjacent ESS racks may also reduce the risk of fire spread. For both the LFP and LNO/LMO tests, sprinkler protection did not prevent ignition of a single module from spreading to involve the entire rack. As shown in Section 6.2, sprinkler protection was sufficient to control the fire to the rack of origin during the LFP test, whereas the fire spread to the adjacent target rack during the LNO/LMO test. Interestingly, lower temperatures were measured at the intersection racks during for the LNO/LMO test, possibly due to wetting from sprinkler water. This suggests that the involvement of the target rack was a result of direct exposure to the fire and that a thermal barrier at the front of the rack would also be needed to block this fire spread path.

There are three primary configurations for battery based ESS located within buildings that are comprised of multiple racks, as shown in Figure 7-3 In general order of expected hazard, these configurations are: a) individual racks in a non-combustible cabinet; b) multiple racks with each rack contained in a separate non-combustible cabinet; and c) multiple racks contained within a shared non-combustible cabinet. This hazard ranking assumes that the presence of non-combustible separators between racks will impede the spread of fire, or battery thermal runaway, from rack to rack. Thus, the design shown in Figure 7-3c represents the reasonable worst-case configuration for any given ESS.

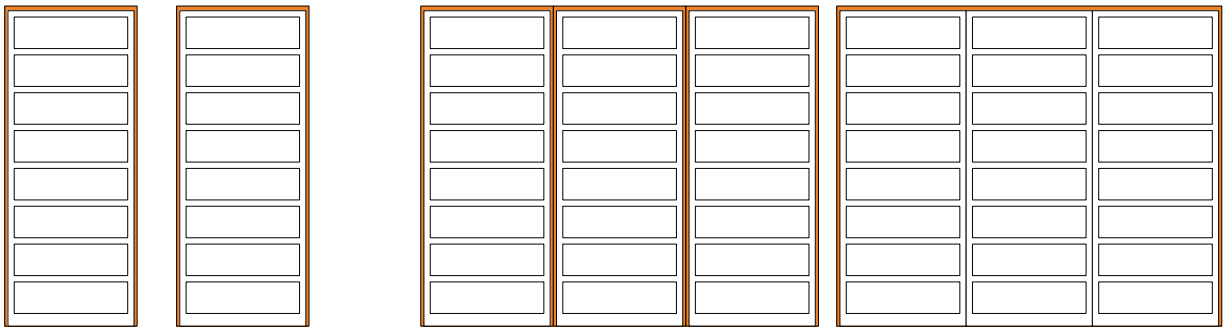

a) Individual racks in separate non-combustible cabinets

b) Multiple racks with each rack contained in a separate non-combustible cabinet (i.e., racks separated by cabinet walls)

c) Multiple racks contained in a shared non-combustible cabinet (i.e., no separation between racks)

Figure 7-3: Elevation view of installation configurations for an ESS comprised of multiple racks.

[iii] Assuming a thermal response of 1,100 $m^{½}s^{½}$ (2,000 $ft^{½}s^{½}$) as representative of metal ceiling construction elements of at least 6 mm (0.25 in.) thickness.

All ESS racks should be considered combustible for the purpose of determining adequate space separation, regardless of the installation configuration. When sprinkler protection is present per Section 6.2.2, the separation distances in Table 7-1 for combustibles can be applied to the tested LFP and LNO/LMO systems as follows:

- Multiple LFP racks installed side-by-side, as shown in Figure 7-3a-b, can be excluded from the separation distance requirements because the fire did not spread beyond the rack of origin in the sprinklered fire test.

- Multiple LNO/LMO racks installed side-by-side, as shown in Figure 7-3a-b, should follow the separation distance requirements to avoid fire spread from one rack to the next. If lesser separation is provided, the sprinklered system design should be adjusted as discussed in Section 7.1.3.

- Multiple rack installations for both the LFP and LNO/LMO systems, as shown in Figure 7-3c, are beyond the scope of this project and should follow the separation distance requirements.

When sprinkler protection is not provided, each individual LFP or LNO/LMO rack should be separated as combustibles per Table 7-2. Refer to Section 6.1.2.4 for additional discussion.

7.1.3 Sprinkler System Considerations

Two critical parameters needed to determine the water supply for a sprinkler system are the number of sprinklers expected to operate and the duration of the fire event. As discussed in Section 2, the target sprinkler protection was a 12 mm/min (0.3 gpm/ft^2) discharge density over a 230 m^2 (2,500 ft^2) demand area, as specified for an EH1 occupancy in NFPA 13 [14] or an HC-3 occupancy in DS 3-26 [16]. The water demand area is typically based on the number of sprinklers needed to provide adequate protection during a large-scale fire test plus a 50% safety factor. Thus, a common evaluation criterion for sprinklers on 3.0 m × 3.0 m (10 ft × 10 ft) spacing is ≤ 16 sprinkler operations.

The above approach to determining sprinkler demand area can be applied to the sprinklered fire tests in Section 6.2.3.4, provided the minimum separation distances in Table 7-1 are met, as follows:

- For the LFP test, a single sprinkler operation controlled the fire to the rack of origin and all other evaluation metrics were met, such as ceiling steel temperatures. As a result, the target protection was deemed adequate.
- All ceiling sprinklers operated during the LNO/LMO test, conservatively representing a demand area > 230 m^2 (2,500 ft^2). In addition, the fire spread from the rack of origin to the adjacent target rack, indicating that all ESS racks installed side-by-side in a row could eventually be involved in the fire. Ignition of the target rack occurred during the decay phase of the initial fire, essentially resulting in two separate fire events. As a result, it is reasonable to base the sprinkler demand area on the total area of the room where the LNO/LMO system is located.

Refer to Section 7.2.1 for guidance on determining the representative hazard of an ESS not tested in this project.

The duration of the water demand must exceed the expected fire duration to ensure that protection is available for the entire fire event. From the intermediate- to large-scale testing the average fire duration[iv] was ~5,400 s (90 min) for the LFP tests and ~2,700 s (45 min) for the LNO/LMO tests[v]. Since the LFP fire did not spread beyond the rack of origin, a water duration of 5,400 s (90 min) is adequate for the duration of the fire event. However, the fire did spread to the target rack in the LNO/LMO test and the water duration needs to account for fire spread to all racks installed side-by-side. In this case, a water duration of 2,700 s (45 min) times the number of adjacent racks is necessary to ensure sprinkler water is available for the entire fire event. For example, the water duration doubles to 5,400 s (1 hr 30 min) for two adjacent LNO/LMO racks.

7.2 Comparison to other ESS Systems

The methodology for this project coupled the performance of sprinkler protection and installation guidance, such as space separation, to manage the hazard of an ESS fire event to an acceptable level. The goal was to provide a framework to define the protection guidance for installations beyond the scope of the systems evaluated here. From this work there are two means of determining protection guidance for an arbitrary ESS:

1) Large-scale free burn tests, as described in Section 6.1, are recommended to determine adequate space separation distances to prevent fire spread to nearby combustibles, or damage to non-combustibles, when sprinkler protection is not provided.

2) Large-scale sprinklered tests, as described in Section 6.2, are recommended to determine adequate space separation distances to prevent fire spread to nearby combustibles or damage to non-combustibles, as well as sprinkler protection design, including discharge density/area and water supply duration.

If the ESS installation consists of multiple adjacent racks, then the fire test design must address the potential for fire spread from one rack to the next. One option is to incorporate multiple racks in the fire test, such as described in Section 6.2.

Given the similarity in the construction of the LFP and LNO/LMO systems tested in this project, the predominant difference in the hazard was the battery chemistry and energy density. LNO/LMO batteries are generally considered to have a higher electrical capacity but reduced thermal stability than LFP batteries [45]. However, the effect of rack design, materials-of-construction, battery specifications and chemistry, and other design features are not well understood. While it is reasonable to assume that the hazard of an LNO/LMO-based ESS could be reduced with proper design, it is also possible that the hazard of an LFP-based system would increase through poor design. Because of these issues, it does not appear possible to extrapolate the results obtained with the tested LFP and LNO/LMO systems to others

[iv] Fire duration was calculated as the time between the first and last exceedance of 100 kW based on chemical HRR because time-resolved convective HRR cannot be accurately measured during a sprinklered fire test.

[v] Refer to Table E-1 for tabulated values.

that are significantly different. Large-scale testing is necessary whenever there is doubt regarding the potential impact that a change in an ESS design feature may have on the system hazard.

7.2.1 Comparison of ESS Hazard

Several attempts were made to characterize the results of the tests conducted in this project using easily obtainable physical properties, such as electrical energy or combustible load. From Table 3-1, the electrical energy of each LFP module was 5.2 kWh and the rating for each LNO/LMO module was 7.8 kWh. These values are multiplied by the number of modules in the test to determine the total system electric capacity, i.e., six modules in the intermediate-scale test or 16 modules in the large-scale test. The combustible load present in each test can be similarly calculated from Table 3-2, as 279 ± 28 MJ (265 ± 26 BTU×10^3) for each LFP module and 509 ± 51 MJ (482 ± 48 BTU×10^3) for each LNO/LMO module.

Figure 7-3 shows that the total energy released across all free burn tests exhibited a similar linear increase with respect to both electrical capacity (left) and combustible load (right). These trends are consistent with the LFP and LNO/LMO modules having a comparable ratio of electrical energy to combustible load, i.e., 6 ± 0.5%, though the trends may not extend to modules with a different ratio. It should be noted that total energy released is not a direct indicator of hazard, since a short duration large fire can release the same energy as a long duration small fire. Figure 7-4 shows that the maximum HRR during the tests, which is the basis for the separation distance recommendations in Section 7.1.2, exhibited a non-linear increase as a function of the same physical properties. This can be partially attributed to more extensive heating occurring within the larger systems leading to faster involvement in the fire. In both plots the maximum HRR of the LNO/LMO is higher than that of the LFP, indicating that the LNO/LMO batteries present a greater fire hazard than the LFP batteries.

It is important to bound the above characterization to the modules tested in this project. LFP and LNO/LMO batteries, which represented ~60% of the total battery market in 2016 [46], typically contain an electrolyte solution consisting of a lithium salt, e.g., $LiPF_6$, in a mixed organic solvent, e.g., ethylene carbonate (EC) or dimethyl carbonate (DMC) [47, 48, 45]. Different modules, even comprised of batteries with the same chemistries, could have a significantly different ratio of electrical energy to combustible load depending on the materials of construction and may not follow the same linear trends observed in Figure 7-3. The energy density per unit volume also needs to be considered since it impacts the physical size of the ESS. For example, the lower energy density of the LFP modules compared to the LNO/LMO modules, 153 kWh/m^3 versus 196 kWh/m^3, means that LFP modules will occupy a larger volume to produce the same electrical output. This can affect the overall design of an ESS, either in terms of the combustible load per rack or the number of racks in the system.

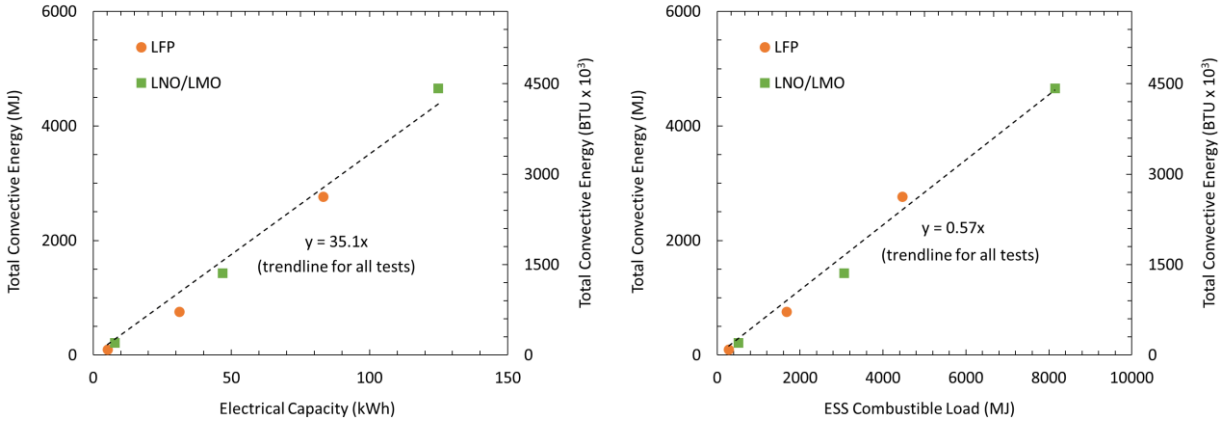

Figure 7-4: Total convective energy as a function of electrical capacity (left) and combustible load (right) for the LFP and LNO/LMO tests.

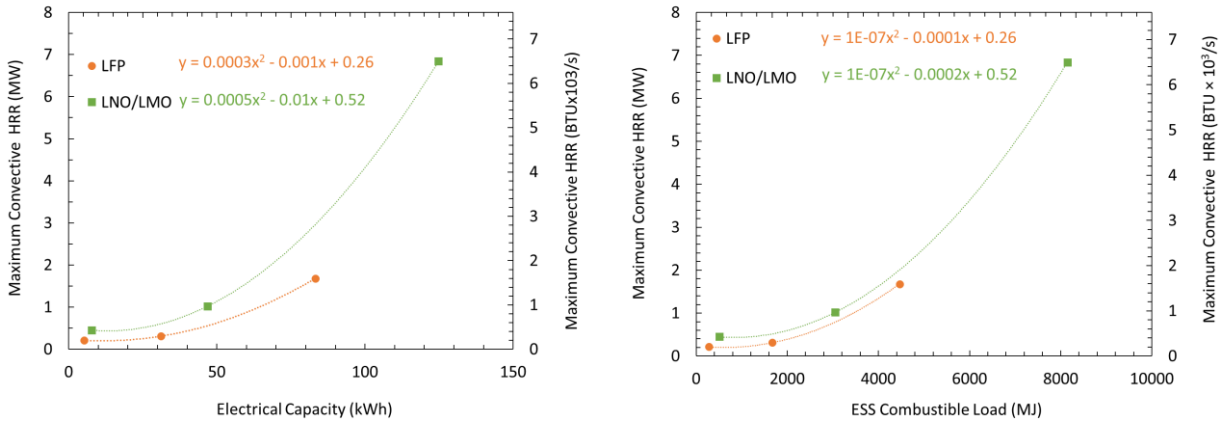

Figure 7-5: Maximum convective HRR energy as a function of electrical capacity and combustible load for the LFP and LNO/LMO tests.

Table 7-1 compiles the corresponding separation distances to prevent fire spread to nearby combustibles or damage to non-combustibles, established in Section 7.1.2, with respect to system electrical capacity. These distances assume sprinkler protection is present per Section 6.2.2. In this case the primary role of sprinkler protection is to prevent or delay the fire spread to adjacent ESS racks, not extinguish the fire. Table 7-2 compiles comparable separation distances when no fire protection is present.

Table 7-1: Minimum separation distance recommendations between ESS and non-combustible and combustible objects, provided sprinkler protection is present per Section 6.2.2.

ESS Capacity Rating		Non-combustibles	Combustibles
LFP	31 kWh	-	-
	83 kWh	0.9 m (3 ft)	1.5 m (5 ft)
LNO/LMO	47 kWh	-	-
	125 kWh	1.8 m (6 ft)	2.7 m (9 ft)
* See Section 7.2.1 for guidance on calculating the total equivalent ESS capacity (kWh) - Sprinklered tests were not conducted with the 31 kWh LFP or 47 kWh LNO/LMO systems.			

Table 7-2: Minimum separation distance recommendations between ESS and non-combustible and combustible objects, when no fire protection is present.

ESS Capacity Rating		Non-combustibles	Combustibles
LFP	31 kWh	< 0.9 m (< 3 ft)	1.2 m (4 ft)
	83 kWh	1.2 m (4 ft)	1.8 m (6 ft)
LNO/LMO	47 kWh	1.2 m (4 ft)	1.8 m (6 ft)
	125 kWh	2.4 m (8 ft)	4.0 m (13 ft)
* See Section 7.2.1 for guidance on calculating the total equivalent ESS capacity (kWh)			

While it is recognized that the fire hazard posed by an ESS system is in part a function of the electrical capacity and battery chemistry, additional sprinklered fire testing is recommended to confidently reduce the sprinkler demand area, water duration, or separation distances. Since the hazard of the LFP and LNO/LMO systems exhibited a non-linear increase with respect to electrical capacity (or combustible load), testing should always be conducted at the full rack scale as designed for use in an ESS, such as described in Section 6.2. In addition, there must be no obstructions between the sprinkler system and the ESS to ensure adequate protection. Refer to DS 2-0 [15] or NFPA 13 [14] for sprinkler obstruction guidance. Large-scale fire testing is also required to determine protection and installation guidance for other Li-ion based ESS systems.

7.2.2 Impact of ESS Design Features

There are many components of an ESS beyond the battery specifications that affect the overall hazard of the system. The design of the rack enclosure can significantly impact the fire development and effectiveness of sprinkler protection. For instance, the ESS tested in this project had solid side and back walls that provided some passive protection against fire spread between adjacent racks. Even for the sprinklered LNO/LMO test where the fire did spread to an adjacent rack, there was a significant delay between the involvement of the modules within the rack where ignition occurred and the modules in the adjacent rack. The presence of solid back walls reduced the thermal exposure to objects located behind the tested equipment. In multi-row installations, which often consist of rows of racks mounted back-to-back across a small service gap, the presence of solid back walls would reduce the likelihood of fire jump between rows. Conversely, the open front of the tested ESS racks likely contributed to the fire spread observed in the LNO/LMO test. A solid, or perforated, non-combustible face may have limited

the thermal exposure to the surroundings. However, without proper ventilation, a rack design consisting of all solid walls could also expedite heating of the batteries contained within or result in an explosion hazard. A solid front wall may also reduce cooling provided by the sprinkler system or impede firefighting access for hose stream application.

Further work is needed to establish the relationship between fire hazard and the many aspects of a battery or module design, such as chemistry, capacity, or format. Does a module comprised of 20 Ah batteries pose the same hazard as a module comprised of 5 Ah batteries? What if there are fewer 20 Ah modules in the ESS to store the same amount of energy, or the batteries are cylindrical or prismatic? Non-combustible or fire-retardant materials-of-construction should be used whenever possible to minimize the overall hazard of the ESS.

8. Conclusions

Small- to large-scale free burn fire tests were conducted on Li-ion battery-based energy storage systems (ESS) comprised of either iron phosphate (LFP) or lithium nickel oxide / lithium manganese oxide (LNO/LMO) batteries. Coupled with large-scale sprinklered fire tests, the performance of sprinkler protection common to commercial facilities where ESS are being installed was evaluated. The impact of installation practice, specifically space separation from combustible and non-combustible objects, was assessed to ensure that the hazard of an ESS fire event can be managed to an acceptable level. This approach provided a framework to define the protection guidance for installations beyond the scope of the systems evaluated here.

At all test scales, which ranged from a single battery module to full ESS racks containing 16 modules each, the ESS system comprised of LFP batteries exhibited a lower overall hazard. This was most notably observed in the sprinklered tests where, for the LFP system, a single sprinkler operation was sufficient to control the fire to the rack of origin, with no significant involvement of the modules in an adjacent rack. Under the same conditions, the fire spread to an adjacent rack in the test involving a system comprised of LNO/LMO batteries, and the sprinklers operated over a demand area greater than 230 m^2 (2,500 ft^2). Irrespective of test scale or battery chemistry, ignition of a single module was sufficient to involve all other modules within the same ESS rack for both types of batteries.

Based on the experimental results contained in this report, the following conclusions regarding the performance of sprinkler protection can be made, provided the minimum separation distances in Table 7-1 are met. The target sprinkler protection was a 12 mm/min (0.3 gpm/ft^2) discharge density over a 230 m^2 (2,500 ft^2) demand area, as specified for an EH1 occupancy in NFPA 13 [14] or an HC-3 occupancy in DS 3-26 [16]. The protection system was comprised of pendent sprinklers having a K-factor of 81 L/min/$bar^{1/2}$ (5.6 gpm/$psi^{1/2}$), with a nominal 74°C (165°F) temperature rating and RTI of 27.6 $m^{½}s^{½}$ (50 $ft^{½}s^{½}$), installed on 3.0 m × 3.0 m (10 ft × 10 ft) spacing, operating at a nominal 2.0 bar (29 psi) discharge pressure. The applicable sprinkler system demand area for water supply calculations is typically 230 m^2 (2,500 ft^2) for both DS 3-26 and NFPA 13, which is used as the basis for the conclusions below.

- The ESS comprised of LFP batteries, under a 4.6 m (15 ft) ceiling, was adequately protected by the target sprinkler protection. The water supply should be based on a minimum 230 m^2 (2,500 ft^2) demand area with a duration of at least 90 minutes. These conclusions are based on a single sprinkler operation controlling the fire to the rack of origin with all other evaluation metrics being met, such as ceiling steel temperatures, and the observed fire duration.

- The ESS comprised of LNO/LMO batteries, under a 4.6 m (15 ft) ceiling, can be adequately protected by the target sprinkler protection. However, excessive ceiling sprinklers operated during the test, conservatively representing a demand area > 230 m^2 (2,500 ft^2). Localized ceiling damage was also predicted to occur at ceiling heights less than 7.6 m (25 ft) due to direct flame impingement. In addition, the fire spread from the rack of origin to the adjacent target rack, indicating that all ESS racks installed side-by-side in a row could eventually be involved in the

fire. Ignition of the target rack occurred during the decay phase of the initial fire, essentially resulting in two separate fire events. As a result, the sprinkler demand area should be based on the total area of the room where the LNO/LMO system is located. The water duration to ensure sprinkler water is available for the entire fire event should be at least 90 minutes for a single ESS rack, or 2,700 s (45 min) times the number of adjacent racks.

- Large-scale free burn tests, as described in Section 6.1, are recommended to determine adequate space separation distances to prevent fire spread to nearby combustibles or damage to non-combustibles, when sprinkler protection is not provided. Large-scale free burn testing is also necessary whenever there is doubt regarding the potential impact a change in an ESS design feature may have on the system hazard.

- Large-scale sprinklered tests, as described in Section 6.2, are recommended to determine adequate space separation distances to prevent fire spread to nearby combustibles or damage to non-combustibles, as well as sprinkler protection design, including discharge density/area and water supply duration.

Given the similarity in the construction of the LFP and LNO/LMO systems tested in this project, the predominant difference in the hazard was the battery chemistry and energy density. However, the effect of rack design, materials-of-construction, battery specifications and chemistry, and other design features are not well understood. While it is reasonable to assume that the hazard of an LNO/LMO-based ESS could be reduced with proper design, it is also possible that the hazard of an LFP-based system would increase through poor design. Because of these issues, it does not appear possible to extrapolate the results obtained with the tested LFP and LNO/LMO systems to other ESSs.

Large-scale testing is necessary whenever there is doubt regarding the potential impact that a change in an ESS design feature may have on the system hazard. If the ESS installation consists of multiple adjacent racks, then the fire test design must address the potential for fire spread from one rack to the next. One option is to incorporate multiple racks in the fire test, such as described in Section 6.2.

9. Recommendations

Protection recommendations for Lithium-ion (Li-ion) battery-based ESS located in commercial occupancies have been developed through fire testing. In consultation with the FM Global Chief Engineering Group, which is responsible for the FM Global Property Loss Prevention Data Sheets, protection and installation recommendations have been established based on current knowledge and may be amended if additional research specific to the hazard of Li-ion based ESS is conducted. The best protection recommendations based on current knowledge are summarized below:

- For the tested LFP system:
    - Without fire protection, the minimum space separation from any part of the ESS is 1.2 m (4 ft) from non-combustible objects and 1.8 m (6 ft) from combustible objects.
    - With sprinkler protection, the minimum space separation from any part of the ESS is 0.9 m (3 ft) from non-combustible objects and 1.5 m (5 ft) from combustible objects. The sprinkler system water supply should be designed for a minimum 230 m^2 (2,500 ft^2) demand area and a duration of at least 90 minutes.
    - These separation distances are based on the LFP system with an 83.6-kWh electrical capacity; refer to Table 7-1 for guidance on lower electrical capacity systems.
- For the tested LNO/LMO system:
    - Without fire protection, the minimum space separation from any part of the ESS is 2.4 m (8 ft) from non-combustible objects and 4.0 m (13 ft) from combustible objects.
    - With sprinkler protection, the minimum space separation from any part of the ESS is 1.8 m (6 ft) from non-combustible objects and 2.7 m (9 ft) from combustible objects. The sprinkler system water supply should be designed for the total room area where the ESS is located, and the water supply should be calculated as 45 minutes times the number of adjacent racks (i.e., the number of racks installed such that the horizontal spacing is less than the recommended space separation for combustible objects).
    - These distances are based on the LNO/LMO system with a 125-kWh electrical capacity; refer to Table 7-1 for guidance on lower electrical capacity systems.

These recommendations can be applied under the following conditions:

- Where sprinkler protection is required, the sprinkler system provides a minimum discharge density of 12 mm/min (0.3 gpm/ft^2) using sprinklers having a K-factor of 81 L/min/$bar^{1/2}$ (5.6 gpm/$psi^{1/2}$) or greater, with a nominal 74°C (165°F) temperature rating and RTI of 27.6 $m^{½}s^{½}$ (50 $ft^{½}s^{½}$).
- All ceiling sprinklers are installed in accordance with FM Global Property Loss Prevention Data Sheet 2-0, *Installation Guidelines for Automatic Sprinklers*, January 2014 [15] or National Fire Protection Association Standard 13, *Standard for the Installation of Sprinkler Systems* [14].

- For ceiling heights in the range of 3.0 m (10 ft) to 7.6 m (25 ft) the ceiling construction should have a minimum 1-hour fire rating.
- Examples of combustible objects include carton packaging, trash, exposed wood product, and anything else that can contribute to the severity of a fire. Examples of non-combustible objects include construction materials having at least 1-hour fire rating, such as framing members or glazing (windows), ceramics, or other items in accordance with FM Global Property Loss Prevention Data Sheet 1-20, *Protection Against Exterior Fire Exposure* [42]. Similar requirements are also found in National Fire Protection Association Code 5000, *Building Construction and Safety Code*[vi].
- For ESS comprised of multiple racks, each individual LFP or LNO/LMO rack should be separated as combustibles per Table 7-2 when sprinkler protection is not provided. Refer to Section 7.1.2 for additional guidance when sprinkler protection is provided.

ESS representing a hazard outside the listed conditions, including design features and energy capacity, may require a more robust protection scheme to account for several unknowns that can negatively affect protection effectiveness. Additional large-scale sprinklered fire tests are necessary to establish a protection scheme that can adequately protect the building and surroundings, as summarized below:

- Large-scale free burn tests, as described in Section 6.1, are recommended to determine adequate space separation distances to prevent fire spread to nearby combustibles or damage to non-combustibles, when sprinkler protection is not provided.
- Large-scale sprinklered tests, as described in Section 6.2, are recommended to determine adequate space separation distances to prevent fire spread to nearby combustibles or damage to non-combustibles, as well as sprinkler protection design, including discharge density/area and water supply duration.
- If the ESS installation consists of multiple adjacent racks, then the fire test design must address the potential for fire spread from one rack to the next.

In practice, a fire watch should be present until all potentially damaged ESS equipment containing Li-ion batteries is removed from the area following a fire event. Fires involving Li-ion batteries are known to reignite any time from minutes to days after the initial event. Adequate cooling of the batteries is necessary to avoid re-ignition. Finally, this project has not addressed explosions hazards or any mitigating that may occur during an ESS fire or an independent event, or firefighting tactics.

[vi] National Fire Protection Association Code 5000, Building Construction and Safety Code, 2018.

Nomenclature

c_p	specific heat (kJ/kg·K)
ESS	energy storage system
HFG	heat flux gauge
HRR	heat release rate (kW)
ΔH	net heat of complete combustion (MJ/kg)
$\dot{G}$	gas generation rate (kg/s)
Li-ion	lithium ion
LFP	lithium iron phosphate
LMO	lithium manganese oxide
LNO	lithium nickel oxide
$\dot{m}_{gas}$	mass flow (kg/s)
MBB	module balancing board
PT	plate thermometer
QR	quick-response sprinkler
RAD	radiometer
r	radial distance (m)
RTI	response time index
SOC	state of charge
SR	standard-response sprinkler
$\dot{q}''$	heat flux (kW/m^2)
$\dot{Q}$	heat release rate (kW)
TC	thermocouple
t	time (s)
T	temperature (K)
v	velocity (m/s)
z_o	virtual origin of fire (m)

Greek Symbols

ε	surface emissivity (-)
ρ	density (kg/m^3)
χ_r	radiant fraction (-)

Subscripts

CO	carbon monoxide
CO_2	carbon dioxide
conv	convective
chem	chemical
inc	incident
rad	radiation

References

1. US Department of Energy. (accessed, December 5, 2018) US DOE Global Energy Storage Database. [Online]. https://www.energystorageexchange.org

2. C. Arbizzani, G. Gabrielli, and M. Mastragostino, "Thermal stability and flammability of electrolytes for lithium-ion batteries," *Journal of Power Sources*, vol. 196, no. 10, pp. 4801-4805, 2011. DOI: 10.1016/j.jpowsour.2011.01.068

3. T. Bandhauer, S. Garimella, and T. Fuller, "A Critical Review of Thermal Issues in Lithium-Ion Batteries," *Journal of The Electrochemical Society*, vol. 158, no. 3, pp. R1-R25, 2001. DOI: 10.1149/1.3515880

4. C. Campion, W. Li, and B. Lucht, "Thermal Decomposition of LiPF6-Based Electrolytes for Lithium-Ion Batteries," *Journal of The Electrochemical Society*, vol. 152, no. 12, pp. A2327-A2334, 2005. DOI: 10.1149/1.2083267

5. D. Doughty, E. Roth, C. Crafts, G. Nagasubramanian, G. Henriksen, and K. Amine, "Effects of additives on thermal stability of Li ion cells," *Journal of Power Sources*, vol. 146, no. 1-2, pp. 116-120, 2005. DOI: 10.1016/j.jpowsour.2005.03.170

6. C.-Y. Jhu, Y.-W. Wang, C.-Y. Wen, C.-C. Chiang, and C.-M. Shu, "Self-reactive rating of thermal runaway hazards on 18650 lithium-ion batteries," *Journal of Thermal Analysis and Calorimetry*, vol. 106, no. 1, pp. 159-163, October 2011. DOI: 10.1007/s10973-011-1452-6

7. E.P. Roth, "Abuse Response of 18650 Li-Ion Cells with Different Cathodes Using EC:EMC/LiPF6 and EC:PC:DMC/LiPF6 Electrolytes," *Journal of The Electrochemical Society*, vol. 11, no. 19, pp. 19-41, 2008. DOI: 10.1149/1.2897969

8. S.M. Summer, "Flammability Assessment of Lithium-Ion and Lithium-Ion Polymer Battery Cells Designed for Aircraft Power Usage," U.S. Department of Transportation Federal Aviation Administration, Springfield, VA, DTO/FAA/AR-09/55, 2010.

9. J. Lamb, C. J. Orendorff, L. A. Steele, and S. W. Spangler, "Failure propagation in multi-cell lithium ion batteries," *Journal of Power Sources*, vol. 283, pp. 517-523, June 2015. DOI: 10.1016/j.jpowsour.2014.10.081

10. H. Webster. (May, 2012, accessed 12-13-2018) Full Scale Battery Fire Test Plan Update. presentation. [Online]. https://www.fire.tc.faa.gov/pdf/systems/May12Meeting/Webster-0512-FullScaleBatteryTestPlanUpdate.pdf

11. A. Blum and R. T. Long, "Hazard Assessment of Lithium Ion Battery Storage Systems," Final Report prepared for Fire Protection Research Foundation February, 2016.

12. DNV-GL, "Considerations for ESS Fire Safety," Consolidated Edison New York, NY, Final Report OAPUS301WIKO(PP151895), Rev. #, 2017.

13. B. Ditch, "Development of Protection Recommendations for Li-ion Battery Bulk Storage: Sprinklered Fire Test," FM Global, Technical Report 3053291, 2016.

14. National Fire Protection Association Standard 13, Standard for the Installation of Sprinkler Systems, 2010.

15. FM Global, Property Loss Prevention Data Sheets 2-0, Installation Guidelines for Automatic Sprinklers, Interim Revision January 2018.

16. FM Global Property Loss Prevention Data Sheets 3-26, Fire Protection Water Demand for Nonstorage Sprinklered Properties, 2019 [Approved for Release].

17. National Fire Protection Association Standard 855, Standard for the Installation of Stationary Energy Storage Systems, Proposed Standard, anticipate issuance in 2019.

18. FM Global Property Loss Prevention Data Sheets 5-33, Electrical Energy Storage, January, 2017.

19. D.P. Abraham, E.P. Roth, R. Kostecki, and D.H. Doughty, "Diagnostic Examination of Thermally Abused High-Power Lithium-ion Cells," *Journal of Power Sources*, vol. 161, pp. 648-657, 2006. DOI: 10.1039/c1ee02218k

20. S. J. Harris, A. Timmons, and W. J. Pitz, "A Combustion Chemistry Analysis of Carbonate Solvents in Li-Ion Batteries," *Journal of Power Sources*, vol. 193, pp. 855-858, 2009.

21. M.M. Khan, A. Tewarson, and M. Chaos, "Combustion Characteristics of Materials and Generation of Fire Products," in *SFPE Handbook of Fire Protection Engineering*, P. DiNenno, Ed. Quincy, Massachusetts, New York: Springer, 2016, ch. Section 3, Chapter 4, pp. 1143-1232.

22. International Standards Organization (ISO/IEC) 17025:2005, General Requirements for the Competence of Testing and Calibration Laboratories, 2005.

23. J. Nakos, "Uncertainty Analysis of Steady State Incident Heat Flux Measurements in Hydrocarbon Fuel Fires," ," Sandia National Laboratories , SAND2005-7144, December, 2005.

24. G. Marlair and A. Tewarson, "Effects of the Generic Nature of Polymers in Their Fire Behavior," in *Proceedings of the 7th International Symposium on Fire Safety Science, Worcester (USA)*, 2002, pp. 629-642. DOI: 10.3801/IAFSS.FSS.7-629

25. H. Biteau, "Thermal and Chemical Behaviour of an Energetic Material and a Heat Release Rate Issue," University of Edinburgh, PhD Thesis 2010.

26. H. Biteau, T. Steinhaus, C. Schemel, A. Simeoni, G. Marlair, N. Bal, and J.L. Torero, "Calculation Methods for the Heat Release Rate of Materials of Unknown Composition," *Fire Safety Science*, vol. 9, pp. 1165-1176, 2009. DOI: 10.3801/IAFSS.FSS.9-1165

27. B. Ditch and J. de Vries, "Flammability Characterization of Lithium-ion Batteries in Bulk Storage," FM Global, Technical Report J.I. 0003045375, March 2013.

28. P. Ribière, S. Grugeon, M. Morcrette, S. Boyanoy, S. Laruelle, and G. Marlair, "Investigation on the Fire-Induced Hazards of Li-ion Battery Cells by Fire Calorimetry," *Energy and Environmental Sciences*, vol. 5, pp. 5271-5280, 2012. DOI: 10.1039/clee02218k

29. ASTM E 2058-09, Standard Test Method for Measurement of Synthetic Polymer Material Flammability Using a Fire Propagation Apparatus (FPA), 2009.

30. W. Zhang, C. Xiao, Q. Chen, C. Ding, J. Lui, M. Chen, and J. Wang, "Combustion Calorimetry of Carbonate Electrolytes used in Lithium Ion Batteries," *Journal of Fire Sciences*, vol. 33, no. 1, pp. 22-36, September 2014. DOI: 10.1177/0734904114550789

31. L. Zhou, D. Zeng, D. Li, and M. Chaos, "Total Radiative Heat Loss and Radiation Distribution of Liquid Pool Fire Flames," *Fire Safety Journal*, vol. 89, pp. 16-21, 2017.

32. G. Hankinson and B.J. Lowesmith, "A Consideration of Methods of Determining the Radiative Characteristics of Jet Fires," *Combustion and Flame*, vol. 159, no. 3, pp. 1165-1177, 2012. DOI: 10.1016/j.combustflame.2011.09.004

33. A. T. Modak, "Thermal Radiation from Pool Fires," *Combustion and Flame*, vol. 29, no. 0, pp. 177-192, 1977. DOI: 10.1016/0010-2180(77)90106-7

34. H-C Kung, H-Z You, and R. D. Spaulding, "Ceiling Flows of Growing Rack Storage Fires," in *Twenty-first Symposium (International) on Combustion*, 1986, pp. 121-128.

35. B. Ditch, "The Impact of Thermal Runaway on Sprinkler Protection Recommendations for Warehouse Storage of Cartoned Lithium-Ion Batteries," *Fire Technology*, no. 2, 2018. DOI: 10.1007/s10694-017-0687-6

36. G. Heskestad, "Investigation of a New Sprinkler Sensitivity Approval Test: The Plunge Test," FMRC, Technical Report Serial No. 22485, RC 76-T-50, 1976.

37. G. Heskestad and H.F. Smith, "Plunge Test for Determination of Sprinkler Sensitivity," FMRC, Technical Report J.I. 3A1E2.RR, 1980.

38. H.Z. You and H.C. Kung, "Strong buoyant plumes of growing rack storage fires," in *Twentieth Symposium (International) on Combustion, The Combustion Institute*, 1984, pp. 1547-1554.

39. G. Heskestad, "Pressure Profiles Generated by Fire Plumes Impacting on Horizontal Ceilings," FMRC, Technical Report 0F0E1.RU, 1980.

40. S. Abada, G. Marlair, A. Lecocq, M. Petit, V. Sauvant-Moynot, and F. Huet, "Safety focused modeling of lithium-ion batteries: A review," *Journal of Power Sources*, vol. 306, pp. 178-192, February 2016. https://doi.org/10.1016/j.jpowsour.2015.11.100

41. E.P. Roth, C. Crafts, D.H. Doughty, and J. McBreen, "Advanced Technology Development Program for Lithium-Ion Batteries: Thermal Abuse Performance of 18650 Li-Ion Cells," Sandia National Laboratories, SAND2004-0584, Unlimited Release 2004.

42. FM Global Property Loss Prevention Data Sheets 1-20, Protection Against Exterior Fire Exposure, Interim Revision, October 2016.

43. National Fire Protection Association Standard 80A, Recommended Practice for Protection of Buildings from Exterior Fire Exposures, 2017.

44. National Fire Protection Association Code 5000, Building Construction and Safety Code, 2018.

45. Q Wang, M BinBin, S Stoliarov, and S Jinhua, "A Review of Lithium Ion Battery Failure Mechanisms and FIre Prevention Strategies," *Progress in Energy and Combustion Science*, vol. 73, pp. 95-131, 2019. https://doi.org/10.1016/j.pecs.2019.03.002

46. M. Li, C. Zhongwei, and K. Amine, "30 Years of Lithium-Ion Batteries," *Advanced Materials*, vol. 30, no. 33, June 2018. DOI: 10.1002/adma.201800561

47. B. Scrosati and J. Garche, "Lithium Batteries: Status, Prospects and Future," *Journal of Power Sources*, vol. 195, no. 9, pp. 2419-2430, May 2010. DOI: · 10.1016/j.jpowsour.2009.11.048

48. R. Younesi, G. Veith, P. Johansson, K. Edstrom, and T. Vegge, "Lithium Salts for Advanced Lithium Batteries: Li–metal, Li–O2, and Li–S ," *Energy & Environmental Science*, vol. 8, pp. 1905-1922, 2015. DOI: 10.1039/C5EE01215E

Appendix A. MPS Model

A.1 Introduction

FM Global conducted several large-scale fire tests of Lithium-ion batteries with different electrolytes in the Large Burn Lab of the FM Global Research Campus. The fire was generated by burning a Li-ion battery-based energy storage cabinet. The maximum fire size of burning a single cabinet of Li-ion battery modules reached nearly 9 MW. The radiative heat flux of these fires to a nearby surface such as one as close as 0.9 m (3 ft) to the Li-ion battery cabinet is of interest. The large fire size and close distance of the target location require considering the view angle of the fire. For this purpose, this study utilizes a multi-point source model similar to the approach used by Zhou et al. [31]. The free burn case using lithium nickel oxide / lithium manganese oxide (LNO/LMO) Li-ion battery is analyzed and reported herein.

A.2 Test Configuration

The test configuration related to the placement of heat-flux gages is shown in the left panel of Figure A-1. The fire is generated from a Li-ion battery cabinet. In addition to the battery cabinet, two simulated half-width cabinets covered with a metal surface are placed adjacent to the battery cabinet. Five heat-flux gages are placed around the cabinet, labeled HFG 4 to 8. Table A-1 shows the relative distances and heights from the cabinet and ground surface. The coordinate system (refer to the left panel of Figure A-1) has the x-axis perpendicular to the cabinet front surface, the y-axis overlapping with the lower front edge of the cabinet, and the z-axis overlapping with the vertical centerline of the cabinet front surface.

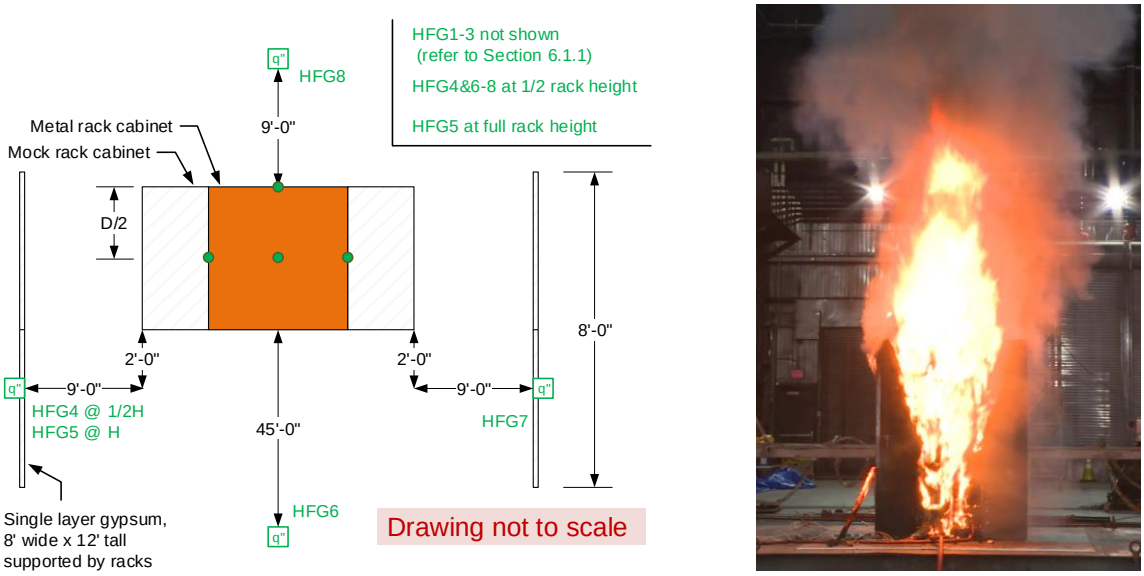

Figure A-1: Left panel: a plan view of test configuration, (not to scale); right panel: fire image of Li-ion battery fire test.

Table A-1: Heat flux gage location parameters for LNO/LMO Li-ion battery fire test

Gage	$x_0\ (ft)$	$y_0\ (ft)$	$z_0\ (ft)$	Plane
HFG4	2	-(9+2.5)*	4.25	x-z
HFG5	2	-(9+2.5)*	8.5	x-z
HFG6	45	0	4.25	y-z
HFG7	2	9+2.5*	4.25	x-z

*Indicating the distance is 9 ft in addition to a half cabinet width of 2.5 ft.

A.3 Multi-point Source Model

The Multi-point Source (MPS) model was originally developed by Hankinson and Lowesmith [32] for jet fire and extended to optically-thin, buoyant turbulent fires by Zhou et al. [31]. In this study, the similar model was applied to calculate the radiative heat flux of significantly larger, potentially optically-intermediate fires, i.e. compared to those examined previously. Theoretically, for optically-intermediate fires, the approach of Modak [33] considers radiation absorption and may better simulate such fires. However, the complex test configuration of the current fire complicates the determination of effective pathlength. Instead, a simple vertical radiative profile with a single adjustable parameter and optically-thin radiative characteristics are assumed in the current approach. Such an approach is expected to capture the main feature related to near-field radiative heat flux.

Figure A-2 shows the geometry setup of the MPS model. The heat flux of interest is at the location (x_0, y_0, z_0) in a coordinate system with the flame base as the origin. The heat flux from a point source of height z_p to a heat flux gage surface is:

$$\dot{q}_p^{"} = \frac{\dot{Q}_{r,z}}{4\pi r^2}\cos(\xi) \qquad \text{A-1}$$

where $\dot{Q}_{r,z}$ is the local emissive power (kW) of a point source at the height z (m); r is the distance between the gage and the point source, and ξ is the angle between the surface normal of the heat flux gage and the line connecting the point source *p* and the gage. Assuming the fire emissive power has a linear distribution with a peak location at z_m (m), its peak value is:

$$h_m = 2\frac{\dot{Q}_r}{L_f} \qquad \text{A-2}$$

where L_f is the instantaneous fire height (m), $\dot{Q}_r$ is the total radiative power of the fire:

$$\dot{Q}_r = \dot{Q}\chi_r \qquad \text{A-3}$$

where $\dot{Q}$ is the chemical heat release rate (kW), and χ_r is the radiant fraction. The radiant fraction is calculated from:

$$\chi_r = 1 - \frac{\int_{t_0}^{t_e} \dot{Q}_c}{\int_{t_0}^{t_e} \dot{Q}} \qquad \text{A-4}$$

where $\dot{Q}_c$ is the convective heat release rate, t_0 and t_e provide the time bounds of heat release rate considered in the calculation. The local emissive power has the form of:

$$\dot{Q}_{r,z} = \frac{z_p}{z_m} h_m, \qquad z \le z_m$$
$$\dot{Q}_{r,z} = \frac{L_f - z_p}{L_f - z_m} h_m, \qquad z > z_m \qquad \text{A-5}$$

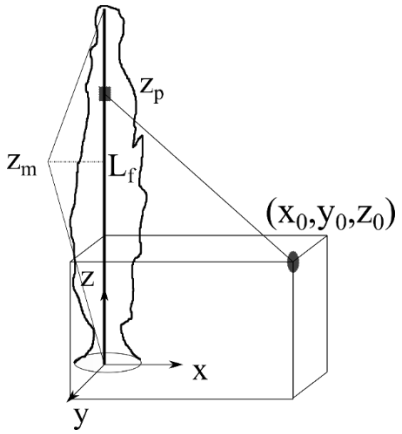

Figure A-2: Setup for the weighted multipoint radiation source model.

The total heat flux of the flame to a gage surface is:

$$\dot{q}_r'' = \int_0^{L_f} \dot{q}_p'' dz_p \qquad \text{A-6}$$

Note that the variables $\dot{Q}$, $\dot{Q}_c$, L_f are based on the experimental measurements, x_0, y_0, and z_0 are the gage locations as listed in Table A-1. The only tuning parameter is the height of the maximum radiative power z_m.

When the fire size is relatively small, such as in the 6-module fire tests, the radiant heat flux emitted from heated module surfaces needs to be considered, which is contrary to the larger fire, such as a full rack fire, where the solid wall surface emission may be blocked by the flame. Figure A-3 shows the geometry configuration for such a consideration. The grey surface represents the module surface with a width of w and height of h. The surface of a heat flux gage is located at (x_0, y_0, z_0).

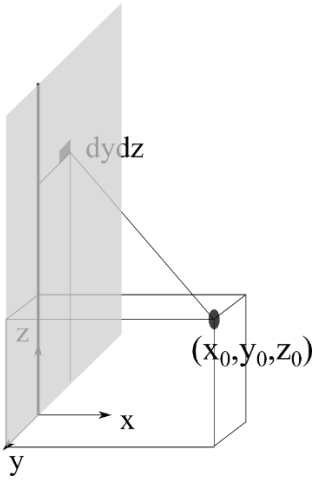

Figure A-3: Geometry setup for the surface radiation model

The radiant power of a surface with a temperature T_s, and emissivity of ε_s is:

$$\dot{Q}_r = \varepsilon_s \sigma T_s^4 dydz \quad \text{A-7}$$

where σ is the Stefan–Boltzmann constant (5.67e-11 kW/m^2K), ε_s is the surface emissivity, T_s is the surface temperature, and dy is the control surface width, dz is the control surface height. Similar to Eq. A-1, the heat flux to a gage surface is:

$$\dot{q}_p^{"} = \frac{\dot{Q}_r}{\pi r^2}\cos(\xi_1)\cos(\xi_2) \quad \text{A-8}$$

where $\dot{Q}_r$ is the local emissive power (kW) of a point source at the module surface; r is the distance between the gage and the point source, and ξ_1 and ξ_2 are the view angles between the surface normal of the module and heat flux gage surface and the line connecting the point source *p* and the gage. The total heat flux of a radiating surface with a width of W and height of H as shown in Figure A-2, to a gage surface is:

$$\dot{q}_{rs}^{"} = \int_0^H \int_{-\frac{W}{2}}^{\frac{W}{2}} \dot{q}_p^{"} dydz \quad \text{A-9}$$

The surface heat flux emitted from hot modules is assumed to be linearly correlated with the fire heat release rate:

$$\dot{q}_{rs}^{"} = \dot{q}_{rs,\max}^{"} \cdot \dot{Q} / \dot{Q}_{\max} \quad \text{A-10}$$

where $\dot{q}''_{rs,max}$ is the radiant power evaluated at the nominal maximum surface temperature at 900˚C (1652˚F), and surface emissivity of 0.9. $\dot{Q}$ is the chemical heat release rate and $\dot{Q}_{max}$ is the maximum

chemical heat release rate of the fire. The total heat flux received by the heat flux gage is the sum of $\dot{q}_r''$ (see Eq. A-6) and $\dot{q}_{rs}''$ (see Eq. A-10).

A.4 Experimental Data Analysis

This section presents a near-field heat flux analysis example using the free burn test with a full rack of LNO/LMO batteries. The chemical heat release rate and the radiant fraction were analyzed based on the 20-MW FPC data. Flame height was measured from the test video. The heat flux gage considered herein are HFG 4-7 as shown in Figure A-1. z_m was adjusted to match the measured heat fluxes of these gages. The "best-matched" z_m was applied to calculate the heat flux at the near-field locations. For the LNO/LMO battery fire, the "best-matched" z_m value is $0.4L_f$, or the maximum flame radiation elevation is 40% of flame height. This value seems to be reasonable considering the fire is like a wall-burning fire, which should have a higher maximum radiation location than those of pool fires. The typical maximum radiation elevation for a pool fire is approximately 20~30% of flame height [7].

For the LNO/LMO fire, t_0 and t_e are selected to be 4220 and 6500 s respectively, this stage represents the most vigorous burning of the batteries. The chemical HRR and convective HRR are shown in Figure A-4(a). The total chemical heat release and convective heat release are shown in Figure A-4(b). From them, the radiant fraction is calculated based on Eq. A-4. The radiant fraction represents the fraction of the cumulative radiative heat of the cumulative chemical energy release. Figure A-4 (c) shows that the radiant fraction has a decreasing trend with time and ultimately relatively stabilizes at 0.3. A possible reason may be that the potential cooling effect of relatively cold rack and battery module incurs a large convective heat loss in the early stage of the fire. With the progress of fire growth and heating of the rack and battery module, such a cooling effect reduces, and the convective heat release rate measured in the exhaust duct system increases. That may contribute to a higher convective heat release and correspondingly a lower radiant fraction in the late stage of fire. Therefore, a radiant fraction value of 0.3 represents a realistic value and also yields reasonable consistency between the modeled and measured heat fluxes, see Figure A-4.

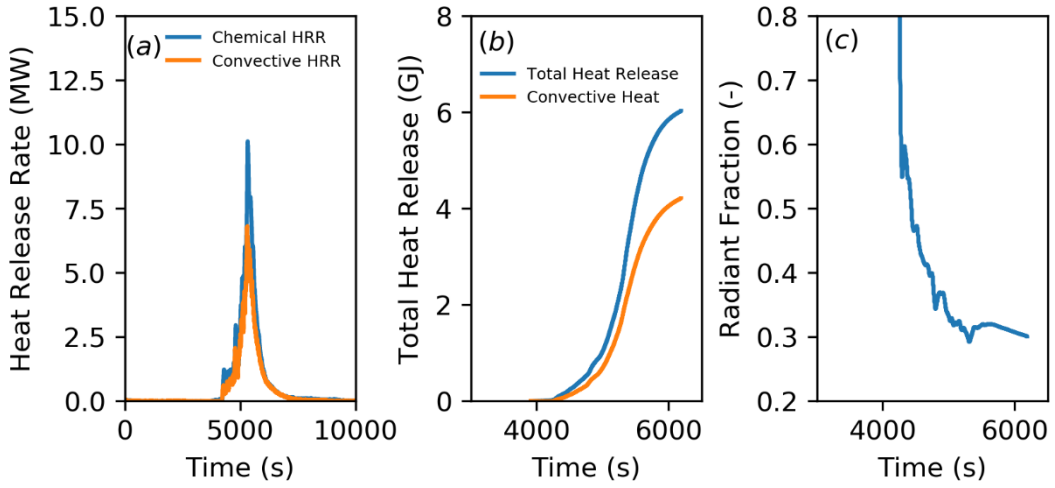

Figure A-4: LNO/LMO free-burn fire test (a) Chemical and convective heat release rates; (b) total chemical heat release and convective heat release; (c) radiant fraction.

Figure A-5 shows the flame heights of LNO/LMO fire test. The time is shifted to the range considered in this study. The flame height quickly increased corresponding to the fire size increase at approximately 4220 s after the ignition, see Figure A-4. In the range of 5390 - 5890 sec, the flame exceeded the field of view of the camera, and the flame height is artificially cut off. For those conditions, the maximum measured flame height is applied in the calculation.

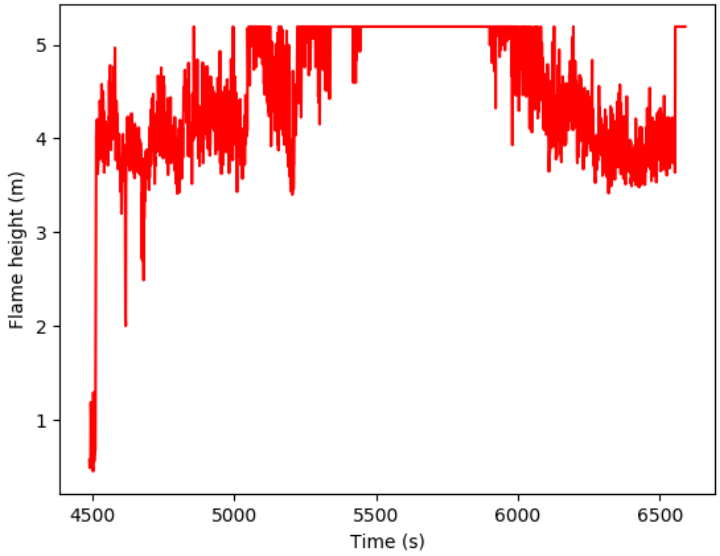

Figure A-5: Flame heights of LNO/LMO fire test.

Figure A-6 shows the comparison of modeled and measured heat fluxes of HFG 4 - 7. The maximum location of radiant power is 0.4 of the flame height. The modeled and measured heat fluxes show reasonable consistencies.

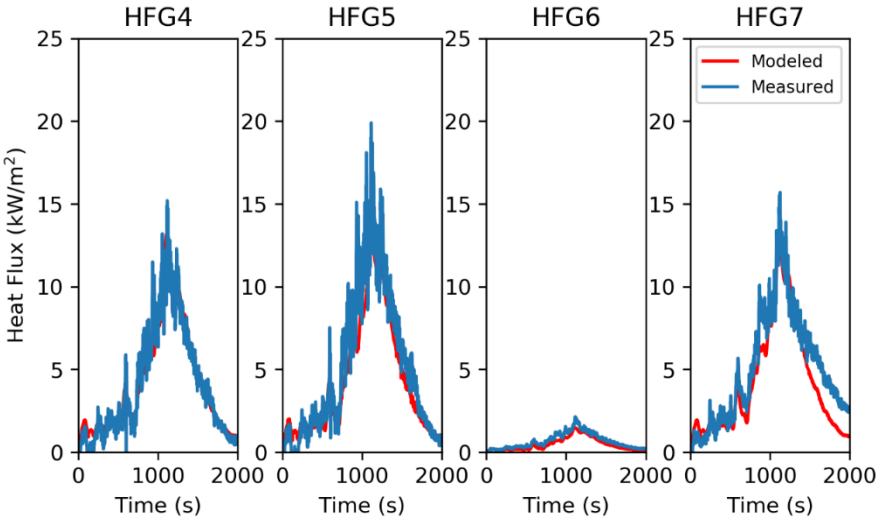

Figure A-6: Comparison of modeled and measured heat fluxes of HFG 4, 5, 6, and 7, time is relative to the selected time window.

Figure A-7 shows the modeled heat fluxes at virtual gage locations like HFG 6, but 0.6, 0.9, 1.2, 1.5 and 1.8 m (2, 3, 4, 5, and 6 ft) away from the cabinet surface. As expected, the heat flux reduces with increased spacing between the gage and the cabinet surface. At the 0.9 m (3 ft) distance, the maximum heat flux reaches close to 100 kW/m^2.

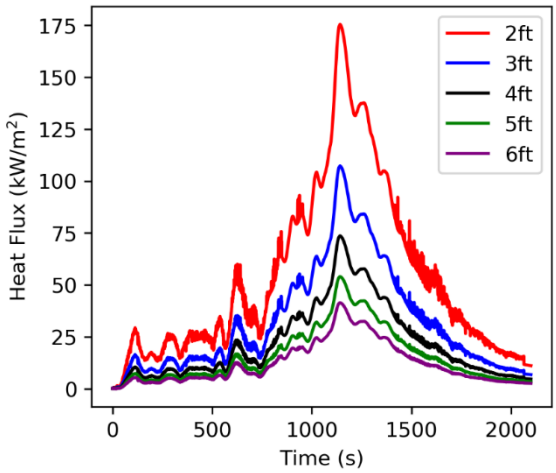

Figure A-7: Modeled near-field, 60-sec running averaged heat fluxes.

A.5 Summary

A multi-point source model was applied to determine the near-field radiative heat flux of Li-ion fire test. The model utilizes the measured heat release rate, radiant fraction, and flame height, and an assumed vertical radiative power distribution with the fraction of the maximum radiative power height of the flame height as the tuning parameter. The free burn test of a full-rack LNO/LMO battery is analyzed and reported as an example. Four of the heat flux measurements are used to tune the parameter, and reasonable comparison shows the model can predict the near-field radiative heat flux.

Appendix B. Small-scale Test Supplemental Information

Table B-1 presents the internal module temperatures acquired for the BMS at the time of communication failure. These values represent the average temperature (± 1 standard deviation) of the front and back of the ignition module near the time of ignition. For the LFP module, communication failure occurred after flames were observed, while communication stopped before ignition during the LNO/LMO tests (with the exception of the small-scale free burn).

Table B-1: Internal module temperatures acquired for BMS at the time of communication failure[+].

Test Scale	LFP		LNO/LMO	
	°C (°F)	°C (°F)	°C (°F)	°C (°F)
Small-scale [Free burn]	78 (172)	21 (70)	50 (122)	22 (72)
Intermediate-scale [Free burn]	55 (131)	22 (72)	41 (106)	34 (93)
Large-Scale [Free burn]	74 (165)	21 (70)	59 (138)	40 (104)
Large-scale [Sprinklered]	55 (131)	26 (79)	48 (118)	27 (81)
Average ± 1 standard deviation	66 ± 12 (150 ± 22)	23 ± 2 (73 ± 4)	50 ± 7 (121 ± 13)	31 ± 8 (87 ± 14)

[+] Communication failure during the small - large scale tests for LFP at 2,790 s, 3,194 s, 2,813 s, and 2,740 s; for LNO/LMO at 3,010 1,632 s, 3,098 s, and 3,260 s.

Appendix C. Intermediate-scale Test Supplemental Information

C.1 Ignition Module BMS Data

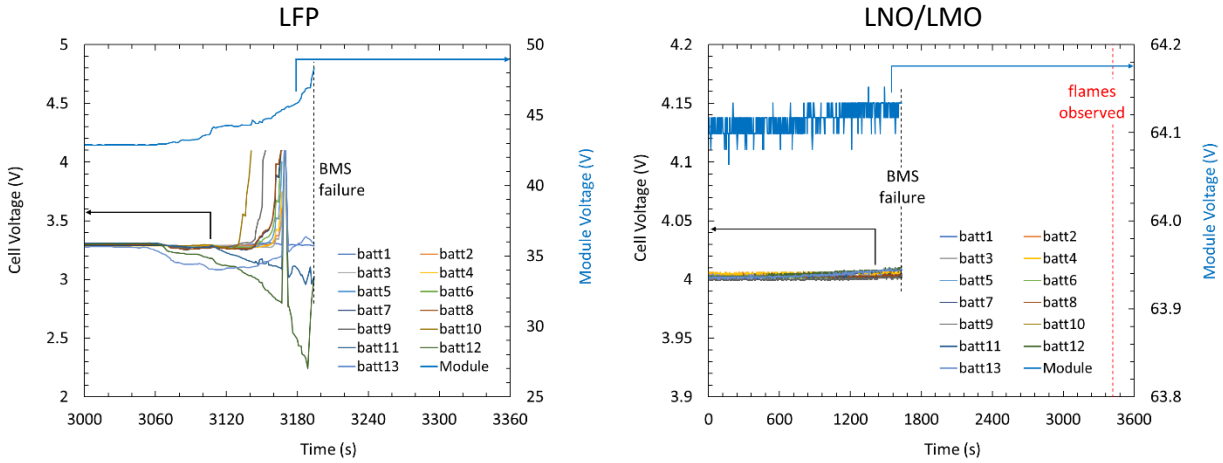

Figure C-1: Voltage measurements from module BMS for LFP (left) and LNO/LMO (right) tests.

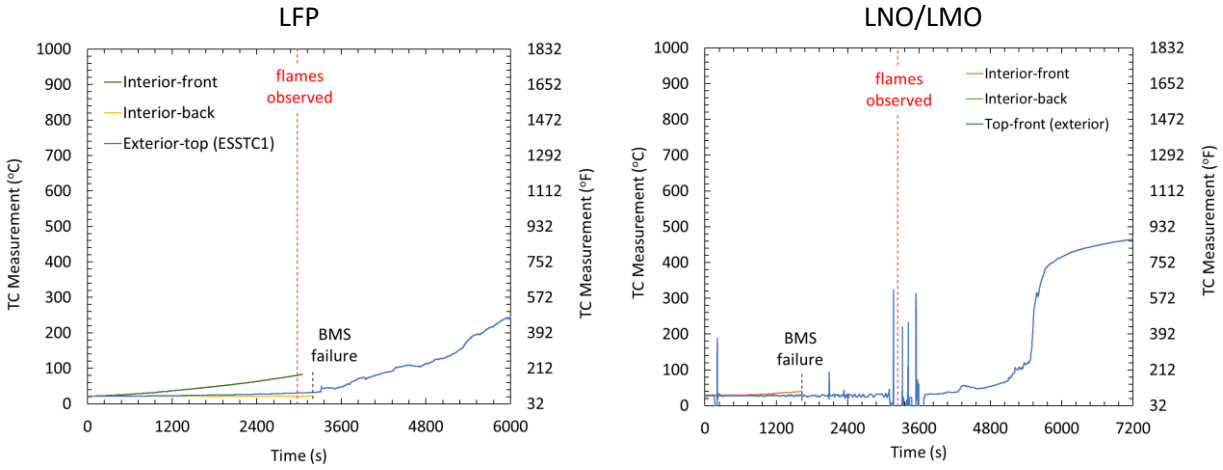

Figure C-2: TC measurements from module BMS for LFP (left) and LNO/LMO (right).

Table C-1: TC measurements at time of observed battery venting; LFP module at 2,974 s and LNO/LMO module @ 3,420 s.

Location	LFP Module		LNO/LMO* Module	
	Front (°C)	Back (°C)	Front (°C)	Back (°C)
External-top	30		34	
Internal	81	22	41†	34†
† Measurement acquired at time of BMS failure (1,632 s)				

C.2 Mock Module TC Data

Figure C-3 presents the TC measurements from the mock modules in the LFP and LNO/LMO tests. Refer to Section 5.1 for a description of the measurement locations. In both tests, peak temperatures were consistent combustion temperature. The tendency for the fire in the LFP test to spread vertically up the modules in the ignition stack before involving the adjacent modules can be seen in the delayed heating of TC8 compared to TC7. Conversely the initial horizontal fire spread from the ignition module to the adjacent module before spreading vertically resulted in a close grouping of the temperature data during the LNO/LMO test.

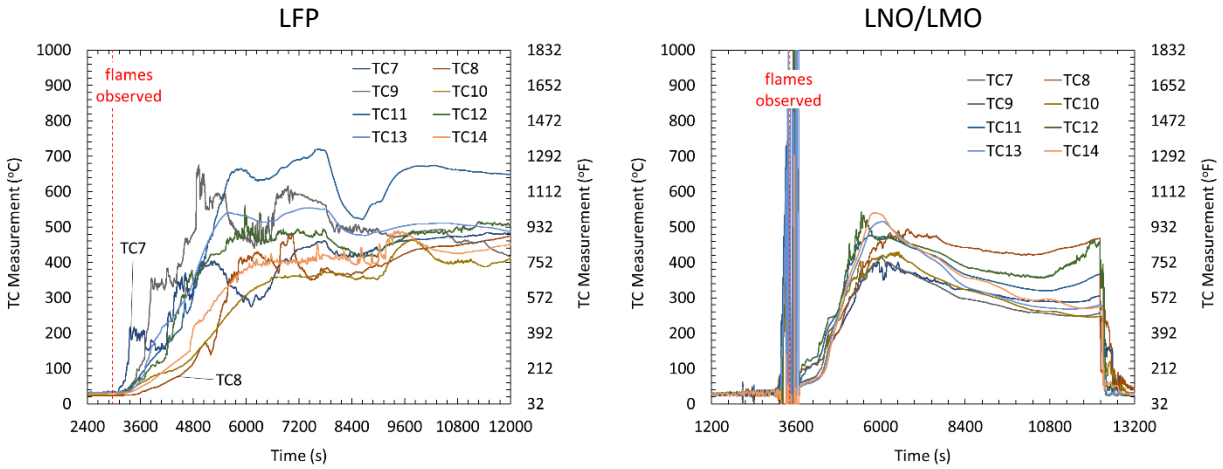

Figure C-3: TC measurements from the mock modules in the LFP (left) and LNO/LMO (right) tests.

Appendix D. Large-scale Test Supplemental Information

D.1 Free burn - Module BMS Data

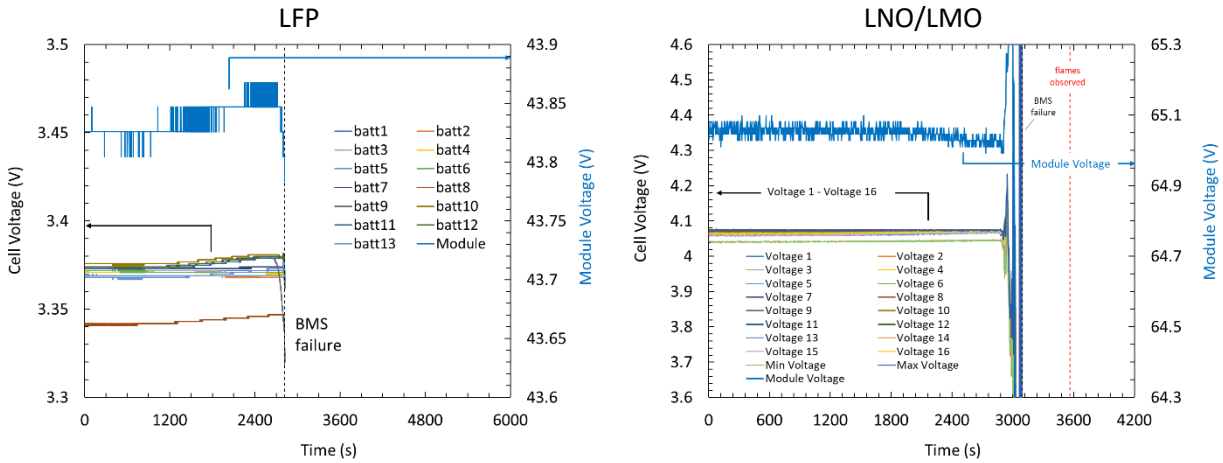

Figure D-1: Voltage measurements from module BMS for LFP (left) and LNO/LMO (right) tests.

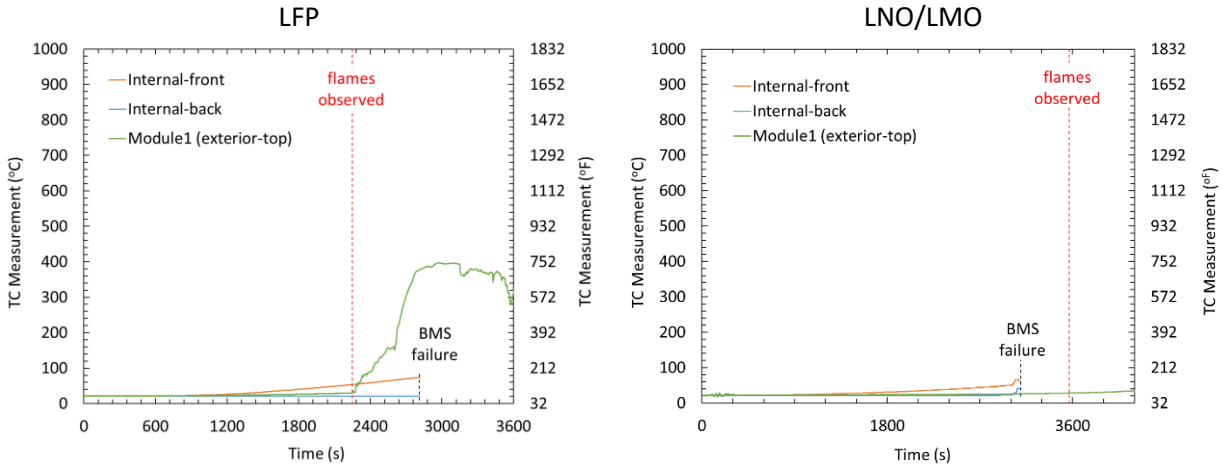

Figure D-2: TC measurements from module BMS for LFP (left) and LNO/LMO (right)

Table D-1: TC measurements at time of observed battery venting; LFP module at 2,250 s and LNO/LMO module @ 3,565 s.

Location	LFP Module		LNO/LMO* Module	
	Front (°C)	Back (°C)	Front (°C)	Back (°C)
External-top	35		28	
Internal	54	21	59†	40†
† Measurement acquired at time of BMS failure (3,093 s)				

D.2 Sprinklered - Module BMS data

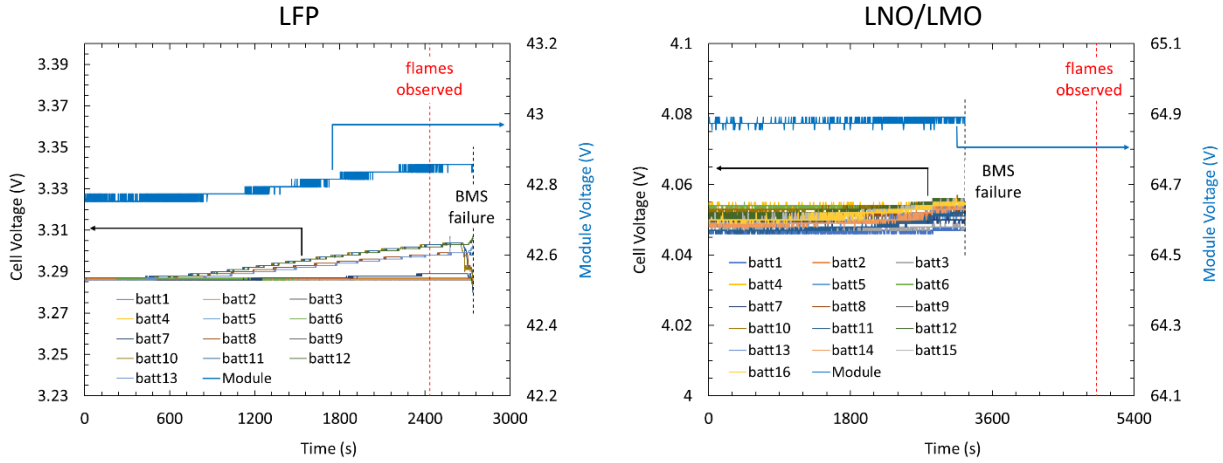

Figure D-3: Voltage measurements from module BMS for LFP (left) and LNO/LMO (right) tests.

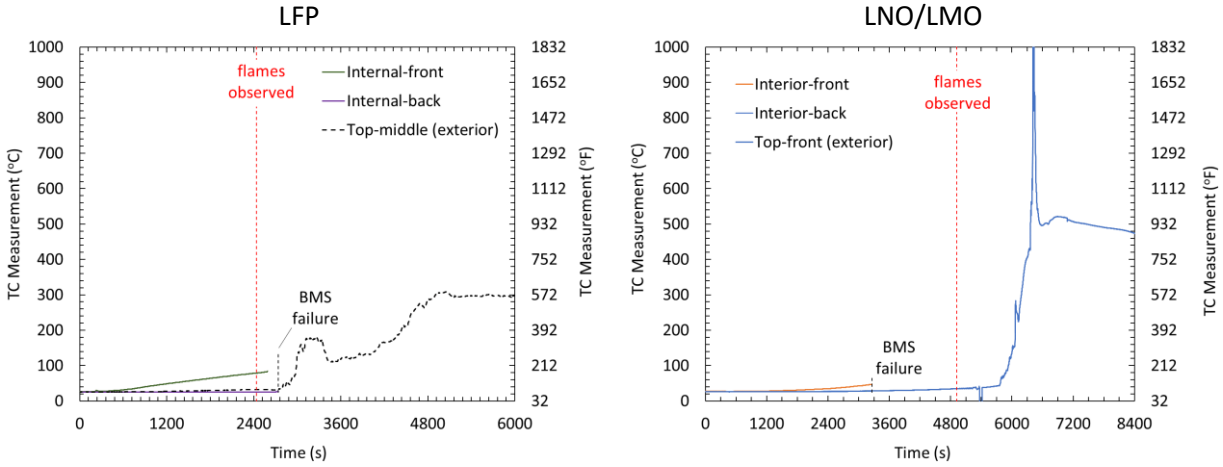

Figure D-4: TC measurements from module BMS for LFP (left) and LNO/LMO (right)

Table D-2: TC measurements at time of observed battery venting; LFP module at 2,435 s and LNO/LMO module @ 4,920 s.

Location	LFP Module		LNO/LMO* Module	
	Front (°C)	Back (°C)	Front (°C)	Back (°C)
External-top	32		35	
Internal	79	26	48†	27†
† Measurement acquired at time of BMS failure (3,260 s)				

Appendix E. Discussion Section Supplemental Information

Table E-1 shows the nominal fire duration from ignition until burn-out. The sprinkler operation time was predicted following the approach discussed in Section 3.4.4.5 for a quick-response sprinkler installed beneath a 4.6 m (15 ft) ceiling. Burn-out was calculated as the time at which the HRR last exceeded 100 kW based on chemical HRR, because time-resolved convective HRR cannot be accurately measured during a sprinklered fire test. The resulting fire duration can be used to determine the necessary water duration requirements for sprinkler protection.

Table E-1: Fire duration from predicted sprinkler operation (actual operation in the sprinklered tests) to burn-out.

LFP					
Test Scale	Ignition	Sprinkler	Burn-out (HRR < 100 kW)	Sprinkler Response Time (ignition-to-sprinkler)	Nominal Fire Duration (sprinkler-to-burn out)
Small	2,790 s	4,350 s	4,925 s	1,560 s	600 s
Intermediate	2,974 s	5,571 s	11,600 s	2,597 s	6,000 s
Large	2,250 s	2,349 s	7,100 s	99 s	4,750 s
Sprinklered	2,435 s	3,667 s	9,189 s	1,232 s	5,500 s

LNO/LMO					
Test Scale	Ignition	Sprinkler	Burn-out (HRR < 100 kW)	Sprinkler Response Time (ignition-to-sprinkler)	Nominal Fire Duration (sprinkler-to-burn-out)
Small	2,820 s	4,195 s	5,905 s	1,375 s	1,700 s
Intermediate	3,420 s	4,276 s	7,581 s	856 s	3,300 s
Large	3,565 s	4,232 s	7,270 s	667 s	3,000 s
Sprinklered*	4,920 s	5,756 s	7,500 s	836 s	1,750 / 2100 s
* The main rack fire duration was 1,750 s; target rack fire duration was 2,100 s